Constrained $\mathcal{H}_2$ Design via Convex Optimization with Applications

by

Beau V. Lintereur

B.S., Aeronautics and Astronautics
Purdue University, 1996

SUBMITTED TO THE DEPARTMENT OF
AERONAUTICS AND ASTRONAUTICS
IN PARTIAL FULFILLMENT OF THE REQUIREMENTS
FOR THE DEGREE OF

Master of Science
at the
Massachusetts Institute of Technology

June, 1998

Signature of Author ____
Department of Aeronautics and Astronautics
May 8, 1998

Approved by ____
Dr. Brent D. Appleby
Charles Stark Draper Laboratory
Thesis Supervisor

Certified by ____
Professor Eric Feron
Assistant Professor of Aeronautics and Astronautics
Thesis Advisor

Accepted by ____
Professor Jaime Peraire
Chairman, Department Graduate Committee

Constrained $\mathcal{H}_2$ Design via Convex Optimization with Applications

by

Beau V. Lintereur

Submitted to the Department of Aeronautics and
Astronautics on May 8, 1998 in partial fulfillment of the
requirements for the degree of Master of Science

Abstract

A convex optimization controller design method is presented which minimizes the closed-loop $\mathcal{H}_2$ norm, subject to constraints on the magnitude of closed-loop transfer functions and transient responses due to specified inputs. This method uses direct parameter optimization of the closed-loop Youla or Q-parameter where the variables are the coefficients of a stable orthogonal basis. The basis is constructed using the recently rediscovered Generalized Orthonormal Basis Functions (GOBF) that have found application in system identification. It is proposed that many typical control specifications including robustness to modeling error and gain and phase margins can be posed with two simple constraints in the frequency and time domain. With some approximation, this formulation allows the controller design problem to be cast as a quadratic program.

Two example applications demonstrate the practical utility of this method for real systems. First this method is applied to the roll axis of the EOS-AM1 spacecraft attitude control system, with a set of performance and robustness specifications. The constrained $\mathcal{H}_2$ controller simultaneously meets the specifications where previous model-based control studies failed. Then a constrained $\mathcal{H}_2$ controller is designed for an active vibration isolation system for a spaceborne optical technology demonstration test stand. Mixed specifications are successfully incorporated into the design and the results are verified with experimental frequency data.

Thesis Supervisor: Dr. Brent D. Appleby
Title: Senior Member of the Technical Staff

Thesis Advisor: Professor Eric Feron
Title: Assistant Professor of Aeronautics and Astronautics

Acknowledgments

Without a doubt, Lawrence McGovern deserves my greatest expression of gratitude and acknowledgment for the success of this work. From the earliest conceptual stages of this research to the final drafts of this thesis, Larry selflessly contributed his talents and time, and assumed a role equivalent to an academic advisor. Most remarkable is that Larry is a student himself with his own research interests and obligations. Although Larry is only a year my senior, he exhibits a combination of theoretical maturity and practical engineering know-how that is truly exceptional. His collaboration was paramount in developing and trouble-shooting the work presented in this thesis. As a bonus, Larry also turned me on to Jazz music which I will no doubt derive a lifetime of enjoyment.

I would like to thank Dr. Brent Appleby and Timothy Henderson at the Charles Stark Draper Laboratory. I always felt that Brent believed in this work and supported my interests. His ideas and contributions where timely and appropriate. It was Brent's idea to use the EOS-AM1 precision pointing attitude control problem as an design example. Tim Henderson encouraged the inclusion of the constrained $\mathcal{H}_2$ methodologies into the SCTB tools and provided the technical information required for the AVIS system identification and design example.

I thank Professor Feron at MIT for giving me the freedom to explore my research interests at Draper. His endless enthusiasm toward control and his research philosophies were always uplifting.

I want to thank the SCTB software development team which included Timothy Henderson, Michael Piedmont, Lawrence McGovern, and Jiann-Woei Jang for responding to my suggestions. Their work made my research more enjoyable and relevant.

I would like to thank my MIT/Draper friends Chris, Gordon, Rudy, Tony, George, Lisa, Larry and Steve (to name a few) for making every day in Cambridge seem like a Seinfeld episode.

Finally, I would like to thank my parents and my brothers Louis, Sam, Barry, Max, and Ross for their continued love, understanding and support. I owe a special thanks to my brother Louis who provided countless encouragement and advice through my engineering studies. His example has been inspirational.

This thesis was prepared at The Charles Stark Draper Laboratory, Inc., under Draper IR&D funding. Publication of this thesis does not constitute approval by Draper or the sponsoring agency of the findings or conclusions contained herein. It is published for the exchange and stimulation of ideas. Permission is hereby granted by the Author to the Massachusetts Institute of Technology to reproduce any or all of this thesis.

Contents

List of Figures

Chapter 1

Introduction

The linear controller design problem can be stated as follows: given a linear time invariant (LTI) model of a plant, find a controller that simultaneously meets a set of design specifications (and perhaps optimize a design metric) or determine that one does not exist. Historically, classical control methods have played a dominant role in practical control applications while model-based methods have been the focus of vigorous theoretical research. However, as many engineers have discovered, achieving a particular set of performance and robustness specifications with these methods can often be indirect. In recent years, the advancement in computer technology and efficient convex optimization algorithms has led to the reformulation of many control problems into general convex optimization problems [3, 4, 5, 60]. Some of the earliest related work is observed in the sequence of publications starting in 1964 by Fegley et. al. [6, 18, 19, 20, 44] where some control problems are shown to have linear and quadratic programming formulations. The result is that the most typical controller design constraints and objective can be cast as a convex optimization problem (frequently as a simple quadratic program) which can be solved efficiently. This ideology provides a nice foundation for developing general purpose Computer-Aided Design (CAD) software. The aim of this thesis is to develop a new CAD tool that extends the work of Boyd et. al. [3, 4], and Polak [60] which demonstrates through example the practical benefits of designing linear controllers with convex optimization algorithms.

1.1 Linear controller design overview

A brief overview and historical account of some analytic and optimization based linear controller design approaches are now discussed to add perspective to the current research. This overview also incorporates preliminary background material regarding mathematical programs, convexity, and optimization.

1.1.1 Classical methods

Traditional classical methods of solving the linear control design problem adopt the strategy of designing the loop gain, the plant and compensator serial combination PK, and inferring the closed-loop performance. Often times the compensator is assumed to have some fixed structure, such as a Proportional Integral Derivative (PID) or lead-lag structure, with corresponding gains that can be tuned through established rules, engineering intuition, or previous experience. Root-locus techniques, Nyquist diagrams, Bode plots, and Nichols charts are used to design the loop gain, analyze stability margins, and infer the closed-loop performance. This framework is especially suited for single-input/single-output (SISO) systems. Application of the classical methods to multiple-input/multiple-output (MIMO) systems is limited by the interplay or cross-coupling between the input/output channels.

A typical simplified control loop diagram used for classical synthesis is shown in Figure 1.1 where r, d, n, y, u, and e are various inputs and outputs that could represent the reference, disturbance, noise, measurement, control, or error signals respectively. Although there are multiple input/output locations in the typical classical closed-loop diagram, each SISO closed-loop, for example from d to e, is treated separately. The designer must simultaneously consider the effects on all of the closed-loop transfer functions of interest when adjusting the compensator gains. Meeting multiple design objectives often becomes indirect and difficult because of the global influence of each gain. Furthermore, formulating the gain selection into an optimization problem results in a non-convex search space, as discussed in Section 1.1.3 under controller optimization methods, and has inherent practical limitations.

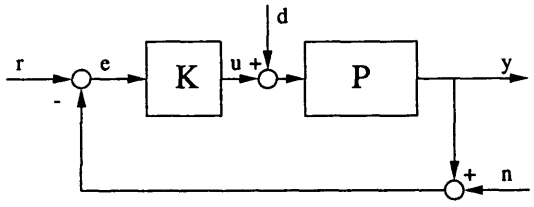

Figure 1.1: Typical classical control loop.

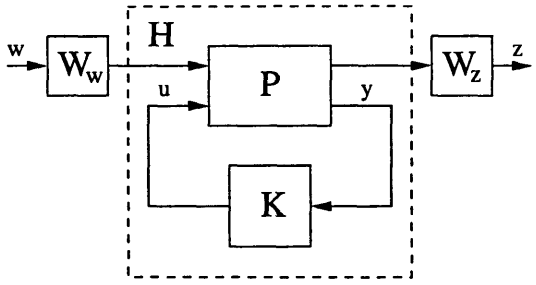

Figure 1.2: Traditional model-based method closed loop.

1.1.2 Traditional model-based methods

Traditional model-based approaches such as the Linear Quadratic Gaussian (LQG, or $\mathcal{H}_2$) or $\mathcal{H}_\infty$ focus on finding analytic solutions to certain classes of problems. These methods generalize the notion of the plant and closed loop as shown in Figure 1.2 so that closed loop H is a linear fractional transformation (LFT) of the plant P with the compensator K. This leaves the map H between the signals w and z open for minimization in terms of some metric or norm. Usually frequency weights or shaping filters are appended to these signals, for example W_w and W_z in Figure 1.2, as a means of penalizing particular frequency bands or shaping the closed-loop response.

The optimal weighted $\mathcal{H}_2$ controller is found by

$$K = \arg\min_K \|W_z H W_w\|_2,$$

where $\|\cdot\|_2$ is the system 2-norm. Similarly, the optimal $\mathcal{H}_\infty$ weighted controller is found by

$$K = \arg\min_K \|W_z H W_w\|_\infty,$$

where $\|\cdot\|_\infty$ is the system ∞-norm. These problems are easily solved through two closed-form Riccati equations or by iterating over modified single parameter Riccati equations. The design variables are now the frequency weights or shaping filters W_z and W_w, and must be adjusted until the desirable closed-loop performance is achieved. One important advantage of this design framework is that MIMO systems are easily handled. However picking the correct set of weights or filters to simultaneously achieve a mixed set of design specifications is still a difficult task.

1.1.3 Parameter optimization methods

The difficulties and limitations of traditional model-based and classical methods and the development of cheap and fast computers have motivated research in direct parameter optimization design methods. The idea is to cast the linear controller design problem as a mathematical program of the form

$$\min \Phi(\omega)$$
$$\text{subject to } \omega \in \Omega$$

where Φ is the objective function, ω is the decision variables and Ω is the feasible set. One important preliminary notion when considering parameter optimization methods or mathematical programs, is the nature of the feasible set and objective function. Most important is the notion of convexity.

A set Ω is said to be convex if

$$\lambda x + (1-\lambda)y \in \Omega, \ \forall x, y \in \Omega, \text{ and } 0 \leq \lambda \leq 1.$$

This definition says that if the two points x and y are in the convex set, then any point on a line segment connecting x and y is also in the set as illustrated in Figure 1.3. A function $f : \Omega \rightarrow \mathrm{R}$ is said to be convex on a convex set Ω if

$$f(\lambda x + (1-\lambda)y) \leq \lambda f(x) + (1-\lambda) f(y), \ \forall x, y \in \Omega, \text{ and } 0 \leq \lambda \leq 1.$$

This definition says that a line connecting two points $f(x)$ and $f(y)$ on a convex function lies above the function between the two points x and y as illustrated in Figure 1.4.

A mathematical program is called convex if Φ is a convex function and Ω is a convex set. One nice property of a convex program is that the local optimal solution is also the global optimal solution. Two important special cases of convex mathematical programs are the linear and convex quadratic programs. In these special cases, the constraints that define the feasible set, also referred to as the constraint set, are linear scalar inequalities of the decision variables, while the objective function is either a linear or quadratic (positive definite) function of the decision variables respectively.

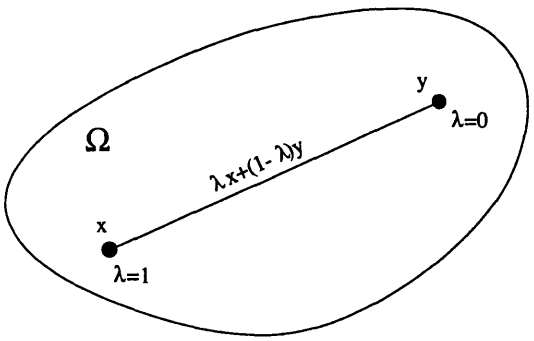

Figure 1.3: Convex set Ω.

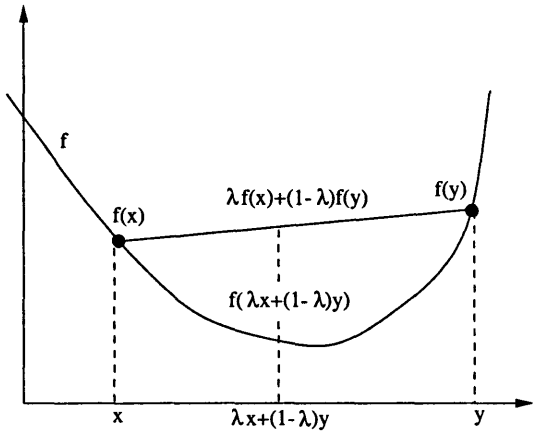

Figure 1.4: Convex function f.

Celebrated optimization algorithms used to solve the linear program are the Simplex Method [27] and the more recently developed interior point methods (for a survey of interior point methods see [22]). Reliable optimization algorithms to solve the quadratic program are readily available and described in [24]. More recent developments in convex mathematical problems write the constraint set in terms of Linear Matrix Inequalities (LMI) [5] in which interior-point optimization methods have been developed to solve [51].

Non-convex optimization problems describe a class of problems where the objective function and feasible set can be non-convex and even disconnected. In this case the nature of the objective function, feasible set, and the existence of local minimum can make these optimization problems NP-hard (A problem is NP-hard if solving it in polynomial time would make it possible to solve all other problems in the class of nondeterministic polynomial time problems in polynomial time).

The purpose of this section is to examine some of the proposed parameter optimization methods, and analyze their objective function and feasible set in terms of convexity and numerical tractability. The parameter optimization methods are categorized into three classes determined by the design variable that is parameterized. The three most common choices are the compensator K, the closed loop H, or the Youla-Parameter Q. Similar survey discussions can be found in the work of Boyd et. al. [3, 4] and Polak [59].

Controller optimization methods

Possibly the most direct parameter optimization approach is to parameterize the compensator itself. This gives the designer maximum control over the compensator order and structure. In the work of Polak and Stimler [62], Davison and Ferguson [12], Ly et. al. [42] and Jacques and Ridgely [36], optimization-based design methods are derived where the compensator is parameterized directly. For example, one possible parameterization for a discrete compensator could represent a partial fraction expansion

$$K(z) \approx \sum_{k=1}^{N} \frac{b_{0k} + b_{1k} z^{-1}}{1 + a_{1k} z^{-1} + a_{2k} z^{-2}},$$

where the decision variables would be the coefficients $b_{01}, b_{02}, \ldots, a_{2N}$. Similarly, the compensator state-space could be parameterized in minimum-realization modal form as suggested in [42].

Now consider constraining a particular closed-loop transfer functions assuming a plant of the form,

$$\begin{bmatrix} P_{11} & P_{12} \\ P_{21} & P_{22} \end{bmatrix}$$

with inputs w and u and outputs z and y as shown in Figure 1.2. The compensator appears in the closed loop in a linear fractional way

$$H = P_{11} + P_{12} K (I - P_{22} K)^{-1} P_{21},$$

or in shorthand $H = \mathcal{F}_\ell(P, K)$. Hence a mathematical program constraining the set closed-loops would be,

$$\text{(P1)} \qquad \min_{K \in \mathcal{K}_K} \Phi(K)$$

$$\mathcal{K}_K = \{K \mid P_{11} + P_{12} K (I - P_{22} K)^{-1} P_{21} \in \mathcal{K}_H\}$$

where $\mathcal{K}_H$ is the closed-loop constraint set, $\mathcal{K}_K$ is set of compensators that produce closed loops inside the constraint set, and K is the compensator, parameterized in a finite dimensional space. Because of the linear fractional dependence of the closed loop on the compensator, convex constraints on the closed loop in general do not result in convex constraints on the compensator [4]. Figure 1.5 gives a graphical

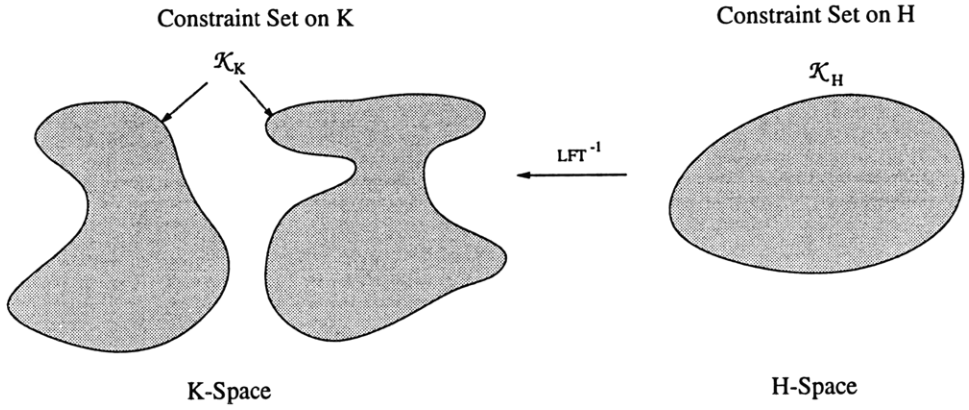

Figure 1.5: Nonconvex, disconnected constraint set in controller optimization.

interpretation of a possible constraint set on the compensator resulting from convex constraints on the closed loop. It is not hard to imagine why constrained optimization problems of this form quickly become numerically intractable. Never the less, some CAD software exists to solve the linear controller design problem with controller optimization formulations (it may be more relevant to solve the control problem this way for some systems). One example is the SANDY code of Ly [42]. There are many examples where these methods have been applied to controller design problems and compared to other parameter optimization methods. See for example [2, 37, 41, 47, 67, 69, 70].

Closed-loop optimization methods

Another class of linear controller design problems treat the closed loop H as the design variable. Now a convex constraint set $\mathcal{K}_H$ of the closed loop avoids the complicated LFT map because the constraints and the design variable H are in the same space. Switching the design variable to the closed loop does not come free and requires additional interpolation conditions to ensure that closed loops in the constraint set are also achievable by some stabilizing compensator. The interpolation conditions appear as additional linear scalar equality constraint in a mathematical problem [9]. In general, the interpolation conditions may result in an infinite number of equality constraints. Figure 1.6 illustrates the convex intersection of the constraint set and set of

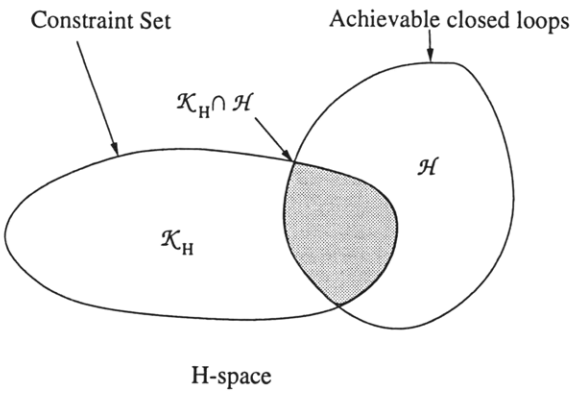

Figure 1.6: Intersection of convex constraint set and set of achievable closed loops in closed-loop optimization.

achievable closed loops. The mathematical program associated with this formulation is

$$\text{(P2)} \qquad \min_{H \in \mathcal{K}_H \cap \mathcal{H}} \Phi(H),$$

where $\mathcal{K}_H$ is the closed-loop constraint set and $\mathcal{H}$ is the set of achievable closed loops. $\mathcal{K}_H \cap \mathcal{H}$ is an infinite dimensional space which is usually parameterized in a finite number of dimensions.

Closed-loop optimization methods are proposed by Dahleh [9, 10] to solve the l_1 control problem, Elia to solve multi-objective control problems [16] and by McGovern [45] to solve the constrained l_1 and $\mathcal{H}_2$ problems. McGovern applied his method successfully to a real hardware system in [46]. The advantage of this method is that the constraints and the design variables are in the same space so the designer has maximum insight into picking a good finite dimensional approximation for H. One disadvantage of this method is that once a desirable closed loop is found, finding the compensator that achieves it relies on an inverse map through the Youla-Parameterization (described in the Q-parameter optimization methods section) , which could be numerically ill-conditioned. Furthermore, the addition of interpolation constraints adds complexity to the optimization problem, especially for multiblock problems [14].

Q-parameter optimization methods

The Q-parameter optimization method exploits the Youla or Q-parameterization of the close loop, eliminating the need for interpolation conditions. The Q-parameterization is an affine parameterization of the set of closed loops achievable with stabilizing compensators,

$$H = \{T_1 + T_2 Q T_3 \mid Q \text{ stable}\},$$

where T_1, T_2, and T_3 are stable systems that are derived from the plant and Q is any stable realizable system. This parameterization was first recognized by Youla et. al. [71, 72] in 1976 and further developed in the 80's; see for example Desoer et. al. [13], Pernebo [57, 58], Nett et. al. [52], Doyle [15], Francis [21], and Vidyasagar [66]. With this formulation, a convex closed-loop constraint set is mapped to convex constraints on Q as illustrated in Figure 1.7. An important result of this parameterization is that every stabilizing compensator is related to Q through a bilinear map. Unfortunately general constraints on the compensator will result in non-convex constraints on Q. The mathematical program associated with this formulation is

$$\text{(P3)} \quad \min_{Q \in \mathcal{K}_Q} \tilde{\Phi}(Q)$$

$$\begin{aligned} \mathcal{K}_Q &= \{Q \mid T_1 + T_2 Q T_3 \in \mathcal{K}_H\} \\ \tilde{\Phi}(Q) &= \Phi(T_1 + T_2 Q T_3), \end{aligned}$$

where $\mathcal{K}_H$ is the closed-loop constraint set, $\mathcal{K}_Q$ is the set of Qs that produce closed-loops inside the constraint set, Φ is the same objective function as in P2, and Q is the infinite dimensional design variable to be approximated with a finite dimensional parameterization.

Q-parameter optimization methods of design are proposed by Gustafson and Desoer [25, 26], Hu and Loewen [30], Boyd et. al.[3, 4] and Polak and Salcudean [60]. In the work of Gustafson and Desoer and Hu and Loewen, convexity is sacrificed by assuming a general parameterization of Q where the design variables describe the location of the poles and zeros of Q. The CAD tool DELIGHT.MIMO [61] was developed

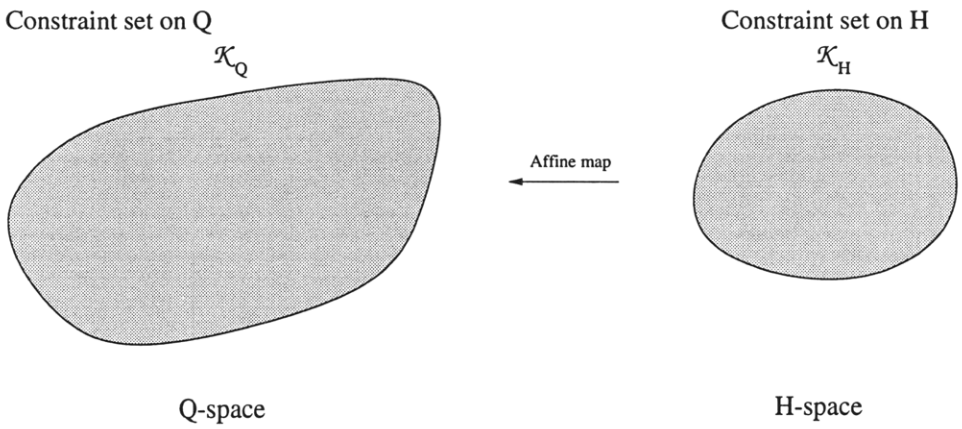

Figure 1.7: Convex constraint set in Q-parameter optimization.

based on the non-convex formulation of Gustafson and Desoer while Hu and Loewen demonstrate their method using the MATLAB's **Optimization Toolbox**. By sacrificing convexity, the designer has maximum control over the order and structure of Q and the resulting compensator. However in general, non-convex mathematical programs can quickly become intractable.

The approach proposed by Boyd et. al. and Polak uses a fixed denominator series expansion model to parameterize Q which preserves the convexity between the Q-space and the parameter space defined by the decision variables. For example, assuming a SISO Q, a finite dimensional approximation of Q would have the form

$$Q(z) \approx \sum_{n=0}^{N-1} F_n(z)\phi_n,$$

where $F_n(z)$ are some fixed denominator stable maps also known as basis functions, N is the total number of basis functions and the ϕs are the decision variables. For sufficiently large N this provides a good approximation for the space of Q but also results in high order compensators. Of course the choice of basis plays a significant role in approximating $Q(z)$ with small N. Typically $Q(z)$ is approximated with a Finite Impulse Response (FIR) basis. The CAD tool QDES [4] was developed based on this methodology and controllers designed with QDES have been demonstrated on a real hardware system [56]. Often times the resulting compensators are reduced using model reduction methods [48] before implementation.

1.2 Scope and Contribution

The goal of this thesis is to examine the impact of Q-parameterization optimization methods on practical control problems. The aim is to bridge the gap between theory and practice by developing a methodology that is accessible to the practicing design engineer. The method proposed in this work attempts to boost productivity by simplifying the problem formulation and user interface while employing proven and efficient optimization algorithms. Exploring more advanced formulations, for example using LMI's, which require more sophisticated optimization algorithms such as semi-definite programming is outside the scope of this work.

The main contribution of this thesis is a reduction in the control system design cycle time. The design cycle time is reduced by combining an easy to use problem specification interface with an efficient problem solution methodology. A more natural expression of many design specifications is proposed using two types of constraints in the frequency and time domain that are easily placed with the aid of a Graphical User Interface tool. The efficiency of the problem solution is increased by approximating the optimization problem with an easily solved quadratic program with a minimum number of basis functions (that are found through an *ad hoc* method developed in this work). A significant factor in realizing this contribution was incorporating the newly rediscovered Generalized Orthonormal Basis Functions (GOBF) into the Q approximation. The GOBF have mostly been studied for system identification applications, however this work proposes that the GOBF are useful in the design problem as well. An *ad hoc* method for selecting the GOBF poles is proposed which is shown to produce lower order compensators while further improving the speed of finding an acceptable solution. This work demonstrates that Q-parameterization optimization methods are applicable to a variety of real controller design problems such as precision pointing attitude control of a flexible spacecraft or vibration isolation of a flexible space structure.

1.3 Organization

This thesis is organized into eight chapters as shown in Figure 1.8. The second through fourth chapters presents the developmental material for the constrained $\mathcal{H}_2$ design methodology. In Chapter 2, the Youla parameterization of the closed loop is presented and the $\mathcal{H}_2$ objective function and closed-loop specifications in the frequency and time domains are formulated. Chapter 3 discusses how to build a good model for design and constrain it to achieve robustness to modeling uncertainty, compensator roll-off, loop gain roll-off, and gain and phase margins. Finally, Chapter 4 presents the Generalized Orthonormal Basis Functions (GOBF) that are used to approximate Q. Chapter 5 gives a brief overview of the Graphical User Interface (GUI) panels developed under subcontract for the Structural Control Toolbox (SCTB) [32] to illustrate how this methodology can be used in a general purpose linear controller design tool. Chapters 6 and 7 present real control applications where the constrained $\mathcal{H}_2$ method was used effectively. The GUI panels described in Chapter 5 were used to design the controllers in these chapters. Finally the conclusions and recommendations for future work are presented in Chapter 8.

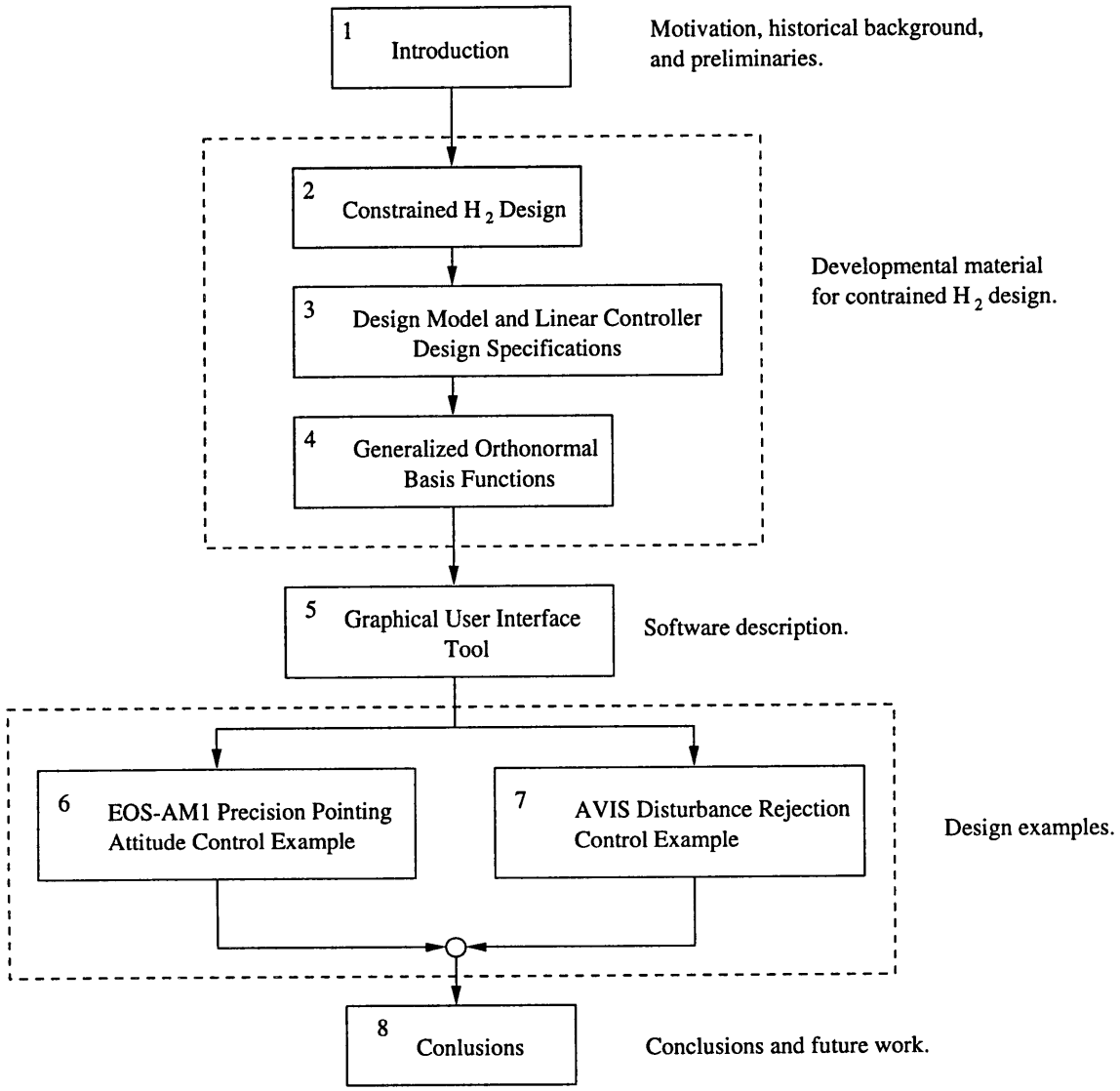

Figure 1.8: Organization of thesis.

Chapter 2

Constrained $\mathcal{H}_2$ Design

There are many variations to the constrained optimization problem that combine a particular objective function with a variety of meaningful constraint sets. In [4], the $\mathcal{H}_2$, $\mathcal{H}_\infty$, and l_1 objectives are considered with constraints such as asymptotic tracking, decoupling, and regulation; overshoot, undershoot, and settling-time limits; bounds on closed-loop signal peaks; bounds on transfer function peak magnitudes; classical single-loop gain/phase margin (M-circle) constraints; and other miscellaneous bounds. Further variations on the constrained optimization design theme include methods that systematically incorporate a nominal controller into the formulation, which is necessary if the plant is unstable. The following discussion explores the marriage of the $\mathcal{H}_2$ (or LQG) design methodology and objective with two simple types of constraints in the frequency and time domain.

A constrained optimization method based on a nominal $\mathcal{H}_2$ design is appealing for several reasons:

- The $\mathcal{H}_2$ objective function is easily constructed as a quadratic function of the free parameters.
- A state space model for the Youla parameterization can be directly obtained from the controller and filter gains of a LQG design.
- An $\mathcal{H}_2$ design guarantees nominal stability of the plant given that the $\mathcal{H}_2$ design assumptions are met.

- Much research has been invested in designing $\mathcal{H}_2$ or LQG controllers.

The question often arises whether $\mathcal{H}_2$ optimization is the best approach to use if some nominally stabilizing controller already exists that exhibits marginal performance. The concern is that the constrained $\mathcal{H}_2$ formulation would start from scratch rather than exploit the good qualities of the nominal controller. The constrained augmentation method is developed in this chapter to deal with this issue.

To some extent, the objective function is less important than meeting a set of design constraints. A typical list of design specifications are usually constraints on the closed-loop and the compensator. Rarely are the specifications concerned with minimizing a closed-loop objective. Most design specifications are based on two simple types of constraints:

1. Time Domain. Constraints on the transient response $z(t)$ to a specified command or disturbance to remain within an envelope, i.e.,

$$z_{min}(t) \leq z(t) \leq z_{max}(t) \text{ for a given } w(t)$$

2. Frequency Domain. Constraints on the closed-loop gain at a particular frequency, i.e.,

$$|H(\omega)| \leq \gamma(\omega)$$

For example, frequency-domain constraints can be used directly or through small gains arguments for loop shaping, gain and phase margin constraints, and robustness to modeling uncertainty.

This chapter develops a powerful convex optimization controller design method to minimize the closed-loop $\mathcal{H}_2$ norm, subject to frequency and time domain constraints on the closed-loop system. Explicit equations are derived for the objective function and constraints. In addition, formulations for the controller augmentation design, quadratic frequency domain constraints, peak-to-peak constraints and Δ phase constraints are included at the end of this chapter.

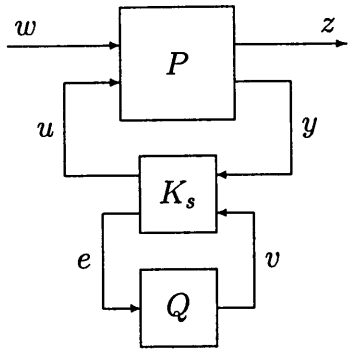

Figure 2.1: Youla Parameterization.

2.1 Youla Parameterization

The Youla parameterization of a closed-loop system is shown in Figure 2.1, where the closed-loop system $H(z) = \mathcal{F}_\ell(P, K)$ is a $n_z \times n_w$ system and $K = \mathcal{F}_\ell(K_s, Q)$ is a $n_u \times n_y$ compensator. Furthermore, K_s is a stabilizing controller with an observer-based state-space realization and Q is realizable and stable [43].

Typically, K_s is derived from an observer based formulation where the output e is the measurement residual, and the input v is added to the actuator command signal. A well known result of observer theory is that the closed-loop transfer function from v to e is zero. Because of this fact, an affine representation of all achievable H is:

$$H = \{T_1 + T_2 Q T_3 \mid Q \text{ stable}\}.$$

where T_1, T_2 and T_3 are stable systems with sizes $n_z \times n_w$, $n_z \times n_u$, and $n_y \times n_w$ [72]. This powerful parameterization represents all stabilizing controllers as $K = \mathcal{F}_\ell(K_s, Q)$ for some stable Q.

2.1.1 State-Space Model of the Youla Parameterization

State-space representations for K_s and T are found in [3, 11, 43] and their derivations are reviewed here for completeness. Consider the plant:

P	$x[k]$	$w[k]$	$u[k]$
$x[k+1]$	A	B_1	B_2
$z[k]$	C_1	D_{11}	D_{21}
$y[k]$	C_2	D_{21}	D_{22}

Figure 2.2 shows the structure of every linear, realizable, stabilizing compensator K for plant P. The blocks connected by the solid line show the familiar model-based controller structure of K_s where F and H are the controller and filter gains respectively. When solving the discrete $\mathcal{H}_2$ control problem, these gains are computed from the solution[1] of two algebraic Riccati equations [73]. In Figure 2.2, the Youla parameter $Q(z)$ is a proper and stable system with realization (A_q, B_q, C_q, D_q).

A derivation of K_s is obtained directly from Figure 2.2 by adding the input v to the actuator command signal before the observer tap and tapping the output measurement residual to obtain e,

$$\begin{aligned} u[k] &= F\hat{x}[k] + v[k], \\ e[k] &= y[k] - C_2\hat{x}[k] - D_{22}u[k]. \end{aligned}$$

In addition, a modification to the state estimate equation is needed to include the contribution of the signal v,

$$\hat{x}[k+1] = (A + B_2F + HC_2 + HD_{22}F)\hat{x}[k] - Hy[k] + (B_2 + HD_{22})v[k].$$

Combining these three equations, the state-space representation for K_s immediately follows,

K_s	$\hat{x}[k]$	$y[k]$	$v[k]$
$\hat{x}[k+1]$	$A + B_2F + HC_2 + HD_{22}F$	$-H$	$B_2 + HD_{22}$
$u[k]$	F	0	I
$e[k]$	$-(C_2 + D_{22}F)$	I	$-D_{22}$

[1] With the following assumptions: i) (A, B_2, C_2) must be stabilizable and detectable ii) D_{11} must be zero iii) D_{12} and D_{12}^T must have full column rank

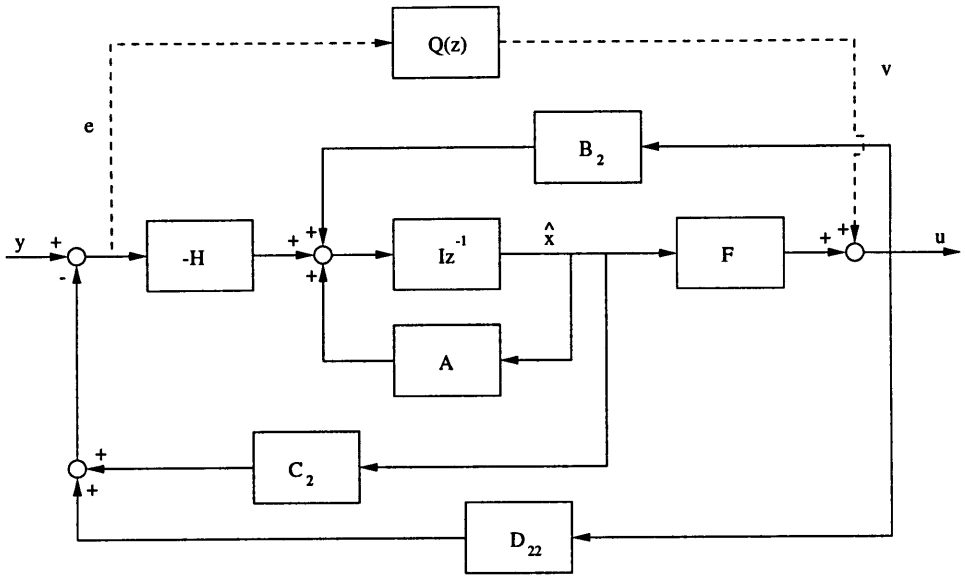

Figure 2.2: All stabilizing compensators.

A realization for T is obtained by algebraically eliminating u and y in a lower linear fractional transformation of P and K_s,

T	$x[k]$	$\tilde{x}[k]$	$w[k]$	$v[k]$
$x[k+1]$	$A+B_2F$	$-B_2F$	B_1	B_2
$\tilde{x}[k+1]$	0	$A+HC_2$	B_1+HD_{21}	0
$z[k]$	$C_1+D_{12}F$	$-D_{12}F$	D_{11}	D_{12}
$e[k]$	0	C_2	D_{21}	0

where $\tilde{x} = x - \hat{x}$. Notice that the state estimate error $\tilde{x}$ is uncontrollable from v while the state x is unobservable from the measurement residual e, hence the transfer function from v to e is zero. Figure 2.3 shows the interconnection between T and Q where the transfer function matrix T is a two by two matrix of the form,

$$T = \begin{bmatrix} T_1 & T_2 \\ T_3 & T_4 \end{bmatrix}.$$

The closed loop from w to z is simply $H(z) = \mathcal{F}_\ell(T, Q)$,

$$H(z) = T_1 + T_2Q(I - T_4Q)^{-1}T_3.$$

Because the map from v to e (T_4) is zero, $H(z)$ is affine in Q,

$$H(z) = T_1 + T_2QT_3$$

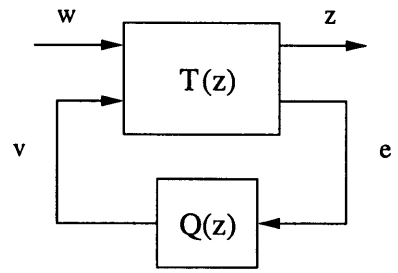

Figure 2.3: T and Q interconnection.

with,

$$T_1 = \left(\begin{bmatrix} A+B_2F & -B_2F \\ 0 & A+HC_2 \end{bmatrix}, \begin{bmatrix} B_1 \\ B_1+HD_{21} \end{bmatrix}, \begin{bmatrix} C_1+D_{12}F & -D_{12}F \end{bmatrix}, D_{11} \right)$$

$$T_2 = (A+B_2F, \quad B_2, \quad C_1+D_{12}F, \quad D_{12})$$

$$T_3 = (A+HC_2, \quad B_1+HD_{21}, \quad C_2, \quad D_{21})$$

2.1.2 Parameterization of $Q(z)$

An infinite-dimensional affine representation of $Q(z)$ is given by:

$$Q(z) = \sum_{p=1}^{n_u} \sum_{q=1}^{n_y} \sum_{n=0}^{\infty} E_{pq} F_n(z) \phi_{pqn}$$

where the E_{pq}'s are $n_u \times n_y$ matrices with the (p,q) entry 1 and all other entries zero, $\{F_n(z)\}$ is a complete sequence of basis transfer functions, and the ϕ_{pqn}'s are the free coefficients. A set of basis functions $\{F_n(z)\}$ is complete if it spans the space of all stable realizable transfer functions, and is orthonormal if $\sum_{k=0}^{\infty} f_i[k] f_j[k] = \delta_{ij}$, where $f_n[k]$ is the impulse response of $F_n(z)$ and δ_{ij} is the Kronecker delta function.

The above infinite-dimensional representation of $Q(z)$ is approximated by the following finite-dimensional representation for optimization:

$$Q(z) \approx \sum_{p=1}^{n_u} \sum_{q=1}^{n_y} \sum_{n=0}^{N-1} E_{pq} F_n(z) \phi_{pqn}$$

where N is the total number of basis functions. The basis functions have less impact on the approximation as n increases, hence good approximations can be achieved with sufficiently large N.

The FIR, Laguerre, and Kautz basis functions are examples of commonly used orthonormal basis functions, and have all been generalized by the following basis function model [54]:

$$F_n(z) = \left(\frac{\sqrt{1-|\xi_n|^2}}{z-\xi_n}\right)\prod_{k=0}^{n-1}\left(\frac{1-\xi_k^* z}{z-\xi_k}\right).$$

This construction allows for arbitrary placement of poles within the unit circle, rather than restricting pole placement to a single location as is the case with the FIR, Laguerre, and Kautz models. In [34], these functions are referred to as the Generalized Orthonormal Basis Functions (GOBF). The GOBF are discussed in Chapter 4 and explicit state-space realizations are provided.

2.2 $\mathcal{H}_2$ Performance Objective

One of the most commonly used objective function in model-based control is the system $\mathcal{H}_2$ norm. The $\mathcal{H}_2$ norm of a MIMO system is defined as

$$\|H(z)\|_2 \equiv \left(\mathrm{Tr}\frac{1}{2\pi}\int_{-\pi}^{\pi} H(e^{i\omega})H(e^{i\omega})^* d\omega\right)^{1/2}.$$

This system norm can be interpreted as the root mean squared value of the system output given a white Gaussian input. By Parseval's theorem, the $\mathcal{H}_2$ norm squared is approximately

$$\|H(z)\|_2^2 \approx \sum_{i=1}^{n_z}\sum_{j=1}^{n_w}\sum_{k=0}^{L} h_{ij}[k]^2,$$

where $h[k]$ is the closed-loop impulse response and L is a finite but large number of time steps. The $\mathcal{H}_2$ norm of the closed loop is constructed from the Youla parameterization in terms of the closed loop impulse response:

$$h_{ij}[k] = t_{1,ij}[k] + \left(\sum_{p=1}^{n_u}\sum_{q=1}^{n_y} t_{2,ip} * \sum_{n=0}^{N-1} f_n \phi_{pqn} * t_{3,qj}\right)[k]$$

where f_n is the basis function impulse response for Q, $t_{1,ij}$, $t_{2,ij}$, and $t_{3,ij}$ are the impulse responses of the (i,j) entries of T_1, T_2, and T_3 respectively, and N is a finite

number of basis functions. The $\mathcal{H}_2$ suboptimal objective can now be written as a quadratic function of ϕ_{pq} (a vectorization of ϕ_{pqn}):

$$\text{minimize} \quad \sum_{p=1}^{n_u}\sum_{q=1}^{n_y} \phi_{pq}^T M_{pq}\phi_{pq} + g_{pq}^T\phi_{pq}$$

where

$$\begin{aligned} M_{pq} &= \sum_{i=1}^{n_z}\sum_{j=1}^{n_w} m_{ipqj}^T m_{ipqj} \\ g_{pq} &= 2\sum_{i=1}^{n_z}\sum_{j=1}^{n_w} t_{1,ij}^T m_{ipqj} \\ m_{ipqj} &= t_{2,ip} * t_{3,qj} * [\ f_0 \quad f_1 \quad \cdots \quad f_{N-1}\ ] \end{aligned}$$

2.3 Closed-loop Specifications

2.3.1 Time-Domain Constraints

Specifications on the transient response of a system due to a specified input can be posed as a set of linear scalar constraints on Q. Consider a MIMO closed-loop transfer function $H(z)$ in which a SISO transfer function $H_{ij}(z)$ is to be constrained. The output z_{ij} due to a specific disturbance w_j is found by the convolution $z_{ij}[k] = (h_{ij} * w_j)[k]$, where $h_{ij}[k]$ is the impulse response of $H_{ij}(z)$. A constraint on the transient response $g_{\mathrm{l},ij}[k] \le z_{ij}[k] \le g_{\mathrm{u},ij}[k]$ can be written as

$$\begin{aligned} \sum_{p=1}^{n_u}\sum_{q=1}^{n_y}(w_j * m_{ipqj})[k]\phi_{pq} &\ge (g_{\mathrm{l},ij} - w_j * t_{1,ij})[k] \\ \sum_{p=1}^{n_u}\sum_{q=1}^{n_y}(w_j * m_{ipqj})[k]\phi_{pq} &\le (g_{\mathrm{u},ij} - w_j * t_{1,ij})[k] \end{aligned}$$

where $g_{\mathrm{l}}[k]$ and $g_{\mathrm{u}}[k]$ are the lower and upper bounds of $z[k]$. This set of constraints is simply the linear inequality $A_{\mathrm{time}}\phi \le b_{\mathrm{time}}$, where ϕ is a vectorization of the ϕ_{pq} vectors.

2.3.2 Frequency-Domain Constraints

Consider the magnitude bound on the frequency response of a SISO transfer function in the MIMO system $H(z)$:

$$|H_{ij}(\omega)| \leq \gamma_{ij}(\omega)$$

with

$$H_{ij}(z) = T_{1,ij} + \sum_{p=1}^{n_u} \sum_{q=1}^{n_y} \sum_{n=0}^{N-1} T_{2,ip} F_n \phi_{pqn} T_{3,qj}.$$

This constraint is equivalent to

$$\Re[H_{ij}(\omega)] \cos\theta + \Im[H_{ij}(\omega)] \sin\theta \leq \gamma_{ij} \quad \forall \theta \in [0, 2\pi).$$

In [9], a magnitude constraint in this form is approximated by a finite number of linear constraints on the real and imaginary parts of $H_{ij}(\omega)$ by only considering a discrete number of angles $\theta_{n,N}$ evenly spaced between 0 and 2π,

$$\Re[H_{ij}(\omega)] \cos\theta_{n,N} + \Im[H_{ij}(\omega)] \sin\theta_{n,N} \leq \gamma_{ij} \cos\frac{\pi}{N} \quad \text{where} \quad \theta_{n,N} = \frac{2n\pi}{N}, n = 1, \cdots, N.$$

The approximate constraint is easily visualized on a Nyquist plot of the constrained transfer function $H_{ij}(z)$. Figure 2.4 shows the exact constraint on the magnitude of $H_{ij}(z)$. The approximation shown in Figure 2.5 corresponds to picking 8 discrete linearly spaced angles between 0 and 2π. Hence, in this example, 8 linear constraints are used to approximate a single frequency-domain constraint at a particular frequency.

This approximation has the property that the intersection of the linear constraints are contained within the exact constraint set. Define the compact set

$$\Omega \equiv \{H_{ij}(\omega) \mid |H_{ij}(\omega)| \leq \gamma_{ij}(\omega)\},$$

and the halfspace

$$\Omega_{\theta_{n,N}} \equiv \{H_{ij}(\omega) \mid \Re[H_{ij}(\omega)] \cos\theta_{n,N} + \Im[H_{ij}(\omega)] \sin\theta_{n,N} \leq \gamma_{ij} \cos\frac{\pi}{N}\}.$$

Then the intersection of the halfspace is contained inside Ω

$$\bigcap_{n=1}^{N} \Omega_{\theta_{n,N}} \subset \Omega$$

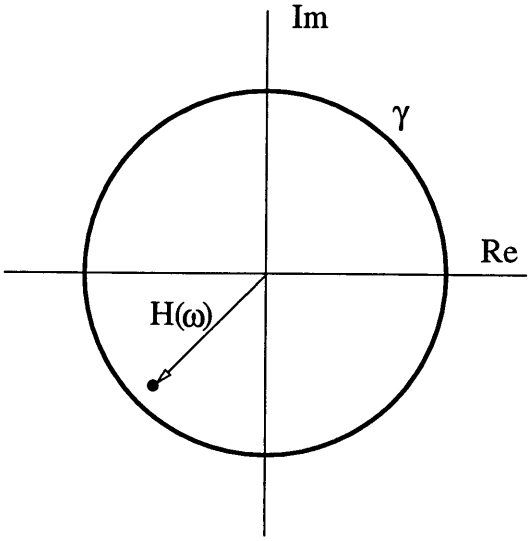

Figure 2.4: Exact magnitude constraint on $H(\omega)$.

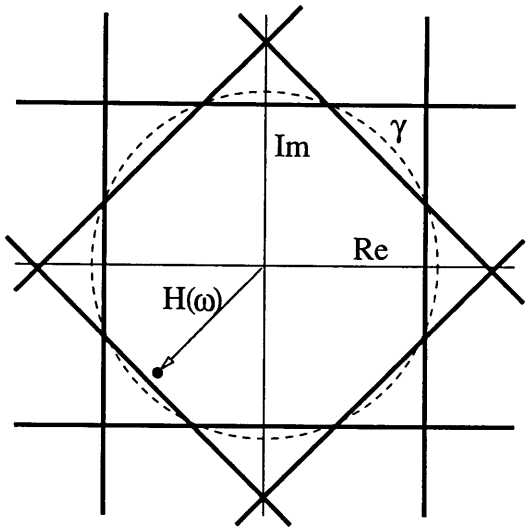

Figure 2.5: Approximate magnitude constraint on $H(\omega)$ with 8 linear constraints.

as seen in Figure 2.5 for $N = 8$. It is easy to show that in the limit as $N \to \infty$

$$\lim_{N\to\infty} \bigcap_{n=1}^{N} \Omega_{\theta_{n,N}} \to \Omega.$$

The approximate magnitude constraint translates to a finite number of linear scalar constraints on ϕ:

$$\sum_{p=1}^{n_u}\sum_{q=1}^{n_y}(\Re[S_{ipqj}(\omega)]\cos\theta_{n,N} + \Im[S_{ipqj}(\omega)]\sin\theta_{n,N})\phi_{pq} \leq L_{ij}(\omega)$$

where

$$S_{ipqj}(\omega) = T_{2,ip}(\omega)[\ F_0(\omega)\ \ \cdots\ \ F_{N-1}(\omega)\ ]T_{3,qj}(\omega)$$

and

$$L_{ij}(\omega) = \gamma_{ij}(\omega)\cos\frac{\pi}{N} - \Re[T_{1,ij}(\omega)]\cos\theta_{n,N} - \Im[T_{1,ij}(\omega)]\sin\theta_{n,N}.$$

This is simply the linear inequality $A_{\text{freq}}\phi \leq b_{\text{freq}}$, where ϕ is a vectorization of the ϕ_{pq} vectors.

2.4 Additional Topics

This section discusses alternate approaches to the constrained optimization problem. These topics represent ongoing ideas for further research, and will not be used in the examples.

2.4.1 Constrained Augmentation Design

In some cases an augmentation to an existing controller is preferred over a complete redesign. An example of this is a controller that operates in two modes where one is a low performance classical control mode and the other is a high performance augmented classical mode. For this case, the augmentation would simply provide the necessary correction to the nominal controller to meet the design specifications. A constrained augmentation approach is developed in this section so that augmentations to existing nominally stabilizing compensators can be designed with the convex optimization framework.

The constrained augmentation design method is similar to the constrained $\mathcal{H}_2$ design method in that they both begin with a baseline stabilizing controller that is augmented with a stable Q parameter to satisfy some constraints set. The constrained augmentation approach departs from the traditional assumption that the baseline controller is observer based and exploits the Youla parameterization such that any stabilizing controller can be used. It is proposed that the objective function for the constrained augmentation method is constructed in a way that penalizes modifications to the baseline controller so that the desirable qualities of the baseline controller are preserved.

Modification to the Youla Parameterization

Frequently in control system development, a nominal controller has been designed which stabilizes the plant and achieves a modest level of performance or robustness. By exploiting the Youla parameterization, the nominal controller can be used as a starting point for an augmented control design. If the nominal controller is observer

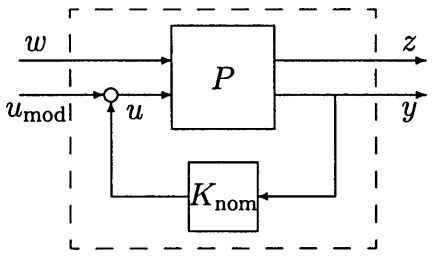

Figure 2.6: Nominal closed-loop system.

based (e.g., developed using LQG or $\mathcal{H}_\infty$ Riccati formulations), then the Youla parameterization is simple as described in Section 2.1. On the other hand, if the nominal controller is not observer based, a Youla Parameterization can still be constructed as follows. Given the open loop plant:

$$\begin{bmatrix} z \\ y \end{bmatrix} = \begin{bmatrix} P_{11} & P_{12} \\ P_{21} & P_{22} \end{bmatrix} \begin{bmatrix} w \\ u \end{bmatrix},$$

add a modified control input to the actuator signal, and close the loop with the nominal controller, as shown in Figure 2.6. Then this "nominal" closed-loop can be written as

$$\begin{bmatrix} z \\ y \end{bmatrix} = \begin{bmatrix} T_{11} & T_{12} \\ T_{21} & T_{22} \end{bmatrix} \begin{bmatrix} w \\ u_{\text{mod}} \end{bmatrix}$$

where

$$T_{11} = P_{11} + P_{12}K_{\text{nom}}(I - P_{22})^{-1}P_{21}$$

$$T_{12} = P_{12} + P_{12}K_{\text{nom}}(I - P_{22}K_{\text{nom}})^{-1}P_{22}$$

$$T_{21} = (I - P_{22}K_{\text{nom}})^{-1}P_{21}$$

$$T_{22} = (I - P_{22}K_{\text{nom}})^{-1}P_{22}.$$

Because this new system is stable, an observer-based Youla parameterization can be constructed where the observer and state feedback gains are zero matrices (the feedback gains are no longer needed to stabilize the system). Defining this "stabilizing" controller with zero gain to be $K_{\text{s,mod}}$, the augmented controller is then

$K = K_{\text{nom}} + \mathcal{F}_\ell(K_{\text{s,mod}}, Q)$. In this case, it can be shown that the Youla Parameterization reduces to:

$$H(z) = T_{11} + T_{12}QT_{21}$$

Q Minimization Performance Objective

It is not clear which objective function is best for constrained augmentation design. It is assumed that the designer has a good nominal controller and desires to modify it slightly while preserving its good qualities. In this case, it makes sense to penalize modifications to the nominal controller. Minimizing the unweighted $\mathcal{H}_2$ norm of Q is one naive but simple way of implementing this strategy. That way, in the limit as $\|Q(z)\|_2^2$ goes to zero, the augmented controller converges to the original nominal controller. If the selected set of basis functions are orthonormal, the $\mathcal{H}_2$ norm of $Q(z)$ is found by

$$\|Q(z)\|_2^2 = \sum_{i=1}^{n_u}\sum_{j=1}^{n_y}\sum_{k=0}^{N-1}\phi_{ijk}^2.$$

The $\mathcal{H}_2$ suboptimal Q objective can now be written:

$$\text{minimize} \quad \phi^T\phi$$

where ϕ is a vectorization of ϕ_{ijk}.

Design Specifications

The frequency and time-domain constraints are unchanged by the constrained augmentation design method.

2.4.2 Quadratic Frequency Domain Constraints

Some designers may prefer to write frequency-domain constraints exactly instead of using the approximation presented in Section 2.3.2. This section shows that a frequency-domain constraint can be written exactly as one quadratic constraint. The advantages of representation over the linear approximation are obvious: (1) it is

exact, (2) each frequency constraint can be represented by a single quadratic constraint. However, it is unclear whether one quadratic constraint will perform better than N approximate linear constraints in the optimization algorithm. MINOS uses a projected augmented Lagrangian algorithm [24] to solve problems with nonlinear constraints. MINOS becomes more efficient solving nonlinear constrained problems if the gradient[2] of the constraint equations are provided, otherwise they are computed numerically at additional computational cost. For this reason, both the quadratic constraints and the gradients are provided in this section.

The frequency-domain constraint, $|H_{ij}(\omega)| \leq \gamma_{ij}(\omega)$ is most naturally written as a single quadratic constraint. Define the scalar values α and β,

$$\begin{aligned} \alpha &\equiv \mathrm{Re}\,[H_{ij}(\omega)] \\ \beta &\equiv \mathrm{Im}\,[H_{ij}(\omega)]\,. \end{aligned}$$

Then the exact frequency-domain constraint shown in Figure 2.4 is,

$$\alpha^2 + \beta^2 \leq \gamma^2.$$

This constraint translates to a quadratic constraint on ϕ by the following procedure.

$$\begin{aligned} \alpha &= \mathrm{Re}\,[T_{1,ij}(\omega)] + \mathrm{Re}\left[\sum_{p=1}^{n_u}\sum_{q=1}^{n_y}\sum_{n=0}^{N-1} T_{2,ip}(\omega)F_n(\omega)T_{3,qj}(\omega)\right]\phi_{pqn} \\ \beta &= \mathrm{Im}\,[T_{1,ij}(\omega)] + \mathrm{Im}\left[\sum_{p=1}^{n_u}\sum_{q=1}^{n_y}\sum_{n=0}^{N-1} T_{2,ip}(\omega)F_n(\omega)T_{3,qj}(\omega)\right]\phi_{pqn} \end{aligned}$$

or in vector notation,

$$\begin{aligned} \alpha &= b_\alpha + A_\alpha^T\phi \\ \beta &= b_\beta + A_\beta^T\phi \end{aligned}$$

where $\phi \equiv [\,\phi_{1,1,0} \quad \phi_{1,1,1} \quad \cdots \quad \phi_{n_u,n_y,N-1}\,]^T$ and

$$\begin{aligned} b_\alpha &\equiv \mathrm{Re}\,[T_{1,ij}(\omega)] \\ A_\alpha &\equiv \mathrm{Re}\,[\cdots \quad T_{2,ip}(\omega)F_n(\omega)T_{3,qj}(\omega) \quad \cdots]^T \\ b_\beta &\equiv \mathrm{Im}\,[T_{1,ij}(\omega)] \\ A_\beta &\equiv \mathrm{Im}\,[\cdots \quad T_{2,ip}(\omega)F_n(\omega)T_{3,qj}(\omega) \quad \cdots]^T \end{aligned}$$

[2]The gradients are used to construct the Jacobian matrix.

Now the quadratic constraint on ϕ can be written,

$$\phi^T(A_\alpha A_\alpha^T + A_\beta A_\beta^T)\phi + 2\phi^T(A_\alpha b_\alpha + A_\beta b_\beta) + b_\alpha^2 + b_\beta^2 \leq \gamma^2$$

and the gradient $\frac{d}{d\phi}(\alpha^2 + \beta^2)$ is easily computed by,

$$\frac{d}{d\phi}(\alpha^2 + \beta^2) = 2A_\alpha^T\alpha + 2A_\beta^T\beta.$$

Experience using quadratic constraints in the constrained $\mathcal{H}_2$ problem is limited. In the few examples that quadratic constraints were tried, MINOS was less robust in terms of finding an initial feasible solution than when solving the problem with the linear approximation constraints.

2.4.3 Peak-to-Peak Constraints

Peak-to-peak constraints on transient responses due to specified inputs are a compact way to write some time-domain specifications. A more attractive application of these constraints is the potential for optimizing the peak-to-peak value. For example, a specification that wishes to minimize the excursion of a state from the origin, as in a disturbance rejection or tracking error problem, would be easily posed as a peak-to-peak constraint, where the constraint value is actually included in the objective function for minimization.

A peak-to-peak constraint on the transient response to a fixed input as shown in Figure 2.7 is easily formulated with the addition of two variables γ_u and γ_l. The response z_{ij} and the variables are constrained in the following way:

$$\begin{aligned} z_{ij} &< \gamma_u \\ z_{ij} &> \gamma_l \\ \gamma_u - \gamma_l &< \gamma_{pk}, \end{aligned}$$

where $z_{ij}[k] = (h_{ij} * w_j)[k]$ and γ_{pk} is the peak-to-peak constraint value which can be fixed or a variable. To implement this in the optimization problem, the first two inequalities are treated like time-domain constraints with the exception that γ_u and

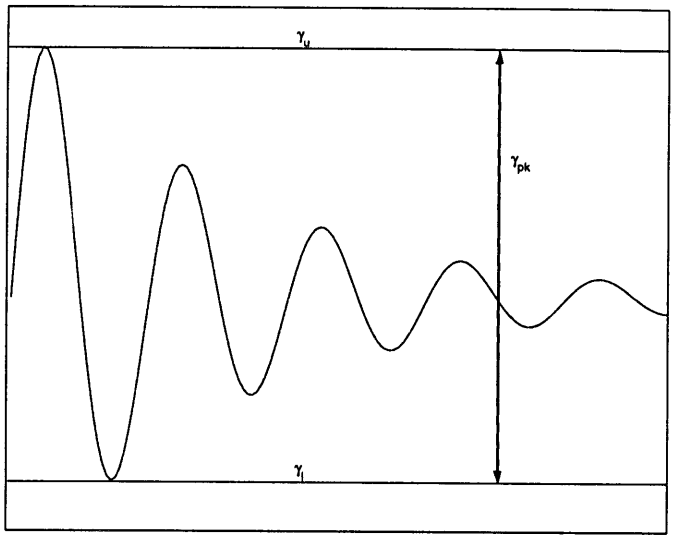

Figure 2.7: Peak to peak constraint.

γ_l are decision variables like ϕ instead of constants but are not represented in the objective function. The last inequality is in the correct form for the optimization problem. It is up to the designer to determine whether γ_{pk} is best defined as a fixed value or a variable that is included in the objective function.

2.4.4 Δ Phase Constraints

A constraint on the phase change between two frequencies is one way to increase damping in a closed-loop mode. The phase change of a lightly damped mode is much more dramatic in the neighborhood of the resonance frequency than in a damped mode. This is illustrated in Figure 2.8 where two modes with a natural frequency of 0.796 Hz but with different damping ratios are plotted. The lightly damped mode has a damping ratio of 0.02 and experiences nearly 180° of phase lag between 0.5 and 2 Hz, while the damped mode with damping ratio 0.6038 only experiences roughly 98° of phase lag. Hence, constraining the phase lag between two frequencies can be used as a mechanism for constraining the damping. These constraints were motivated as a method to eliminate the spiking effect described later in Section 7.4 and shown in Figure 7.11, where mismatched lightly damped poles and zeros cause large gain and phase changes in the closed-loop.

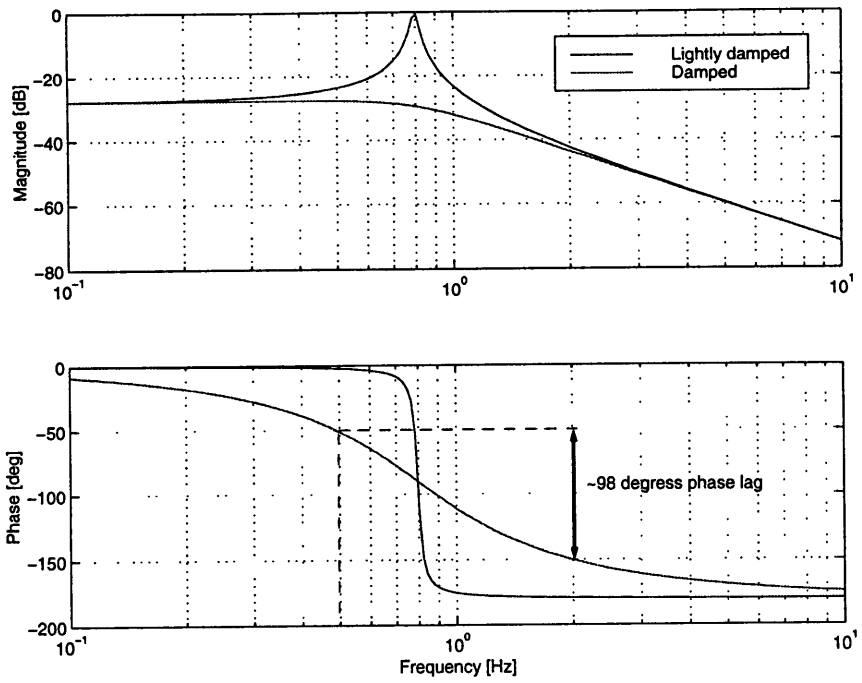

Figure 2.8: Phase change in lightly damped mode compared to damped mode.

The phase change between two frequency points can be written as a quadratic constraint by exploiting the fact that [8],

$$\arg\left(\frac{z_1}{z_2}\right) = \arg z_1 - \arg z_2,$$

where $z \in C$ and $\arg z = \tan^{-1}(\mathrm{Im}\{z\}/\mathrm{Re}\{z\})$. The change in phase of a closed-loop transfer function $H_{ij}(z)$ between two frequency points is equivalently written,

$$\Delta\theta = \theta_1 - \theta_2 = \angle\frac{H_{ij}(\omega_1)}{H_{ij}(\omega_2)},$$

where $\theta = \angle H_{ij}(\omega)$, $H_{ij}(\omega) = \alpha + i\beta$, and α and β assume the same definitions as in Section 2.4.2. After some algebra an inequality constraint can be written,

$$\Delta\theta = \tan^{-1}\frac{\alpha_1\beta_2 - \alpha_2\beta_1}{\alpha_1\alpha_2 + \beta_1\beta_2} \leq \gamma,$$

where γ is the constraint on the change of phase. Finally, the constraint is written,

$$(\alpha_1\beta_2 - \alpha_2\beta_1) - (\alpha_1\alpha_2 + \beta_1\beta_2)\tan\gamma \leq 0,$$

where α and β are affine in ϕ, hence the constraint is quadratic in ϕ.

Chapter 3

Design Model and Linear Controller Design Specifications

This chapter discusses the construction of the design model and formulates some typical linear controller design specifications that are easily incorporated into the constrained optimization approach. The specifications in this chapter are formulated in terms of magnitude bounds on closed-loop transfer functions over a frequency band (see Section 2.3.2). The main theme of this chapter is to demonstrate how to combine ideas from robust control with constraints in the frequency domain to construct useful design specifications.

3.1 The Design Model

A design model, shown in Figure 3.1, is a model that includes the plant with its control input u and measurement y, and any additional input and output channels [1] denoted by w and z respectively that are useful in the design problem. The input/output channels w and z are the signals available to the designer for constraining, optimizing, or both. The closed-loop H is constructed through a lower linear fraction transformation (LFT) of the design model with the compensator as shown in Figure 3.2.

The system H should contain every closed-loop transfer function that the designer

[1] Often referred to as exogenous inputs and regulated outputs.

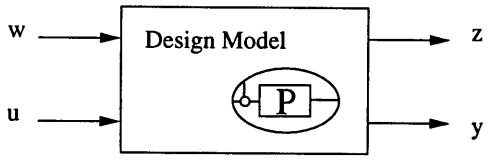

Figure 3.1: Design model.

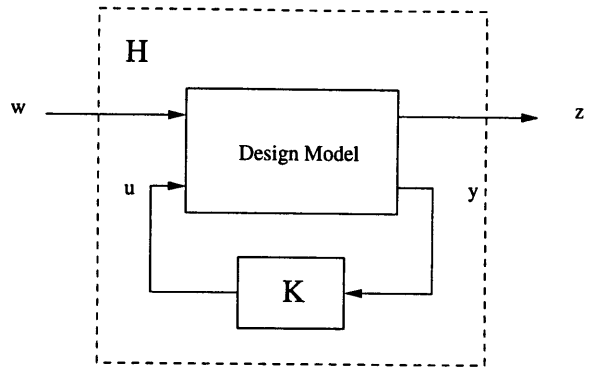

Figure 3.2: Lower linear fractional transformation.

wishes to constrain or optimize. The idea is to add the appropriate inputs and outputs to the design model so that the closed-loop transfer functions of interest appear in H. These inputs and outputs can be interpreted as being physical signals injected or tapped from the system, fictitious signals injected or tapped from the system, or uncertainty applied to the signal path or about the plant or compensator.

Often times, the same closed-loop transfer function can be derived by adding inputs and outputs with different interpretations. As an example, consider the closed-loop disturbance rejection problem shown in Figure 3.3 where d is the disturbance, n is the sensor noise, e is the regulator error and u is the control. This figure illustrates the internal structure of the design model where the signal paths are motivated by the physical interpretation of each input or output. The LFT of this design model with K leads to the following closed-loop transfer function H from w to z,

$$H = \begin{bmatrix} \frac{PK}{1-PK} & \frac{K}{1-PK} \\ \frac{P}{1-PK} & \frac{PK}{1-PK} \end{bmatrix}$$

where $w = [d \quad n]^T$ and $z = [u \quad e]^T$, and d, n, u, and e are scalar signals.

An equivalent design model can be obtained by applying multiplicative uncertainties at the plant input and output as shown in Figure 3.4. The closed-loop transfer function resulting from a LFT of this model with K is also described by H above with $w = [w_1 \quad w_2]^T$ and $z = [z_1 \quad z_2]^T$. The closed loop contains the same SISO transfer functions as in the physically motivated design model.

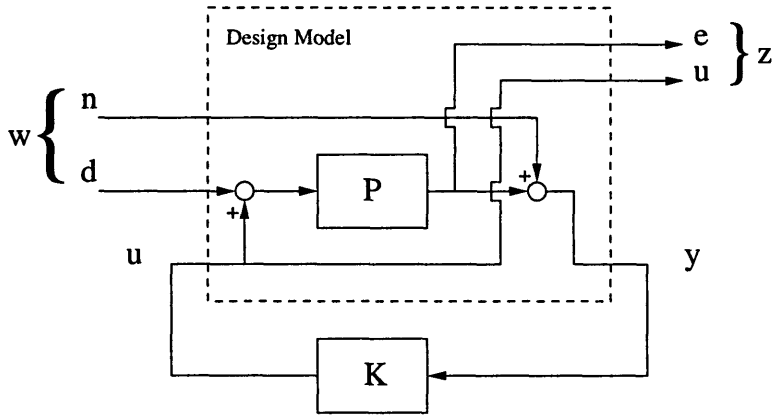

Figure 3.3: Disturbance rejection block diagram.

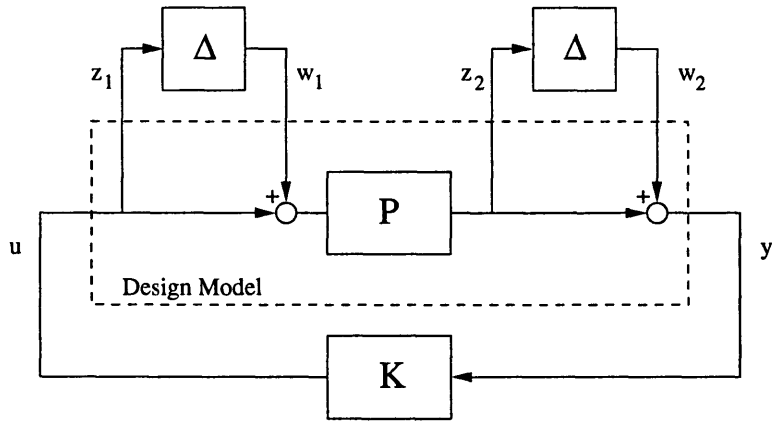

Figure 3.4: Equivalent disturbance rejection block diagram.

Some design specifications follow directly from the input/output pairs of the physically motivated design model while others are better understood by studying an associated uncertainty. For example, to attenuate sinusoidal disturbances at a certain frequency, the transfer function from d to e or $P/(1-PK)$ would be constrained in the frequency domain. Likewise, to avoid actuator saturation in the presence of a specified disturbance, time-domain constraints would be placed on the transient response of the transfer function from d to u or $PK/(1-PK)$. These specifications are derived directly from the physical system. Alternatively, specifications such as robustness to modeling uncertainty, compensator and loop gain roll-off and gain/phase margin constraints are more easily derived from the system modeled with uncertainty. The remainder of this chapter is dedicated to showing how to incorporate the appropriate inputs and outputs into the design model so that these specifications can be enforced.

3.2 Robustness to Modeling Uncertainty

Robustness to modeling uncertainty can be incorporated into the design problem by representing the plant modeling errors as an additive uncertainty as shown in Figure 3.5. The additive uncertainty has the following form

$$P_\Delta = P + \Delta.$$

By the small gain theorem, stability is guaranteed if $|K/(1-PK)| < 1/|\Delta|$ where $K/(1-PK)$ is the transfer function seen by the additive uncertainty. If Δ is of the form $re^{i\theta}$ where $\theta \in [0, 2\pi]$, then stability is guaranteed if

$$\left|\left(\frac{K}{1-PK}\right)(\omega)\right| < \frac{1}{r(\omega)} \qquad \forall\omega.$$

This is simply a frequency-domain constraint, and the approximations derived in Section 2.3.2 can be applied.

Modeling errors can also be reflected on the multiplicative or divisive uncertainty shown in Figures 3.6 and 3.7 respectively. The multiplicative uncertainty has the

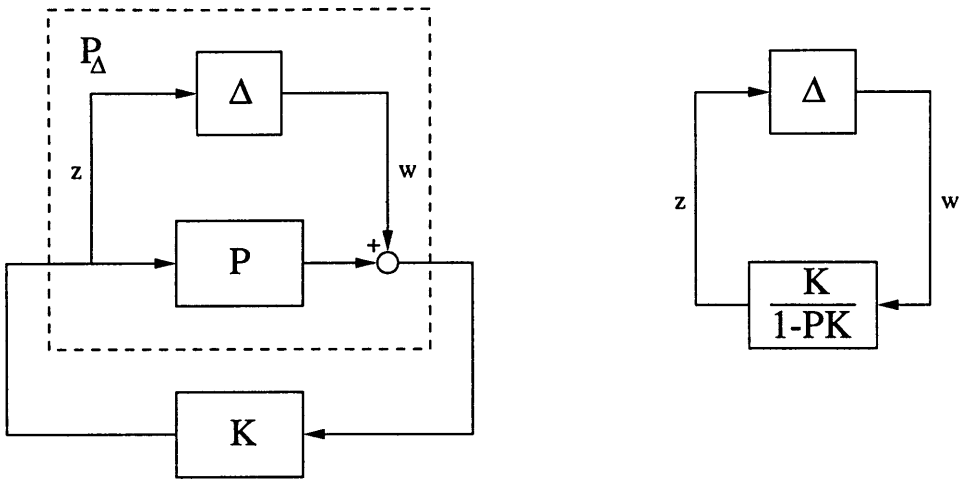

Figure 3.5: Additive uncertainty.

following form

$$P_\Delta = (1 + \Delta)P.$$

Under the same assumptions for Δ with a multiplicative uncertainty, stability is guaranteed if

$$\left|\left(\frac{PK}{1 - PK}\right)(\omega)\right| < \frac{1}{r(\omega)} \qquad \forall\omega.$$

Similarly, the divisive uncertainty has the form

$$P_\Delta = (1 - \Delta)^{-1}P.$$

Stability is guaranteed with a divisive uncertainty if

$$\left|\left(\frac{1}{1 - PK}\right)(\omega)\right| < \frac{1}{r(\omega)} \qquad \forall\omega.$$

3.3 Compensator Roll-off

It is often desirable to have the gain of the compensator roll-off at high frequencies because of inevitable high frequency unmodeled dynamics. Through the constrained optimization design approach, the designer is limited to constraining closed-loop transfer functions rather than constraining the compensator directly. One indirect approach

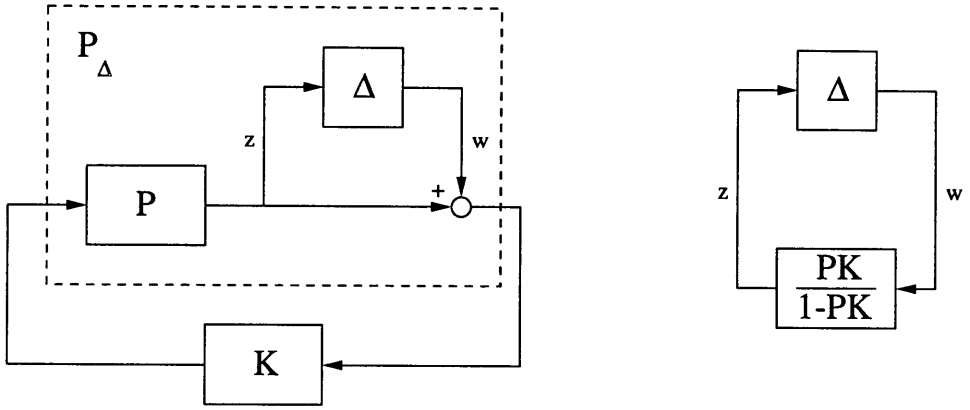

Figure 3.6: Multiplicative uncertainty (at plant output).

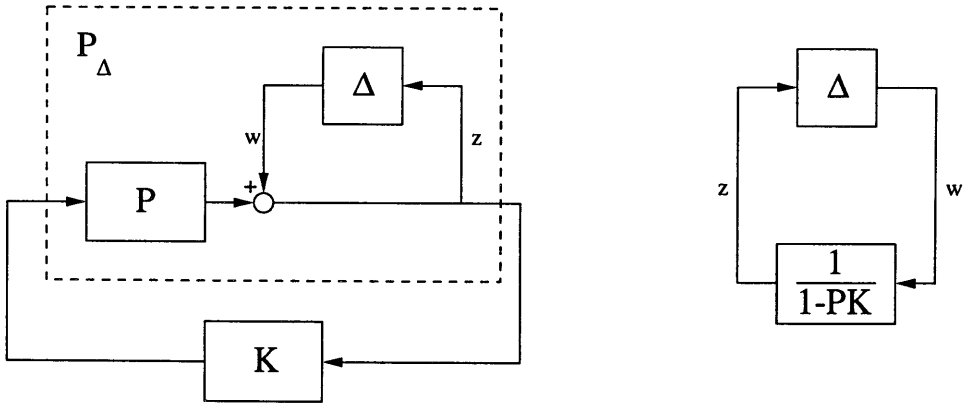

Figure 3.7: Divisive uncertainty (at plant output).

to imposing constraints on the compensator is by applying an additive uncertainty to the nominal plant of the form

$$P_\Delta = P + \Delta,$$

as shown in Figure 3.5. The closed-loop transfer function from w to z is then $K/(1 - PK)$. At high frequencies, Δ will be large so the loop gain will need to be small. Assuming $|PK| \ll 1$, the closed-loop transfer function from w to z is approximately

$$\left|\frac{K}{1 - PK}\right|(\omega) \approx |K(\omega)|.$$

Hence constraining $K/(1 - PK)$ at high frequency is an approximate constraint on the compensator. In [32], the roll-off constraint was proposed,

$$\left|\frac{K}{1 - PK}\right|(\omega) \approx |K(\omega)| < \left(\frac{\omega}{\omega_{co}}\right)^{-\frac{|\alpha|}{20}}$$

where ω_{co} is the crossover frequency and α is the roll-off slope in dB.

3.4 Loop Gain Roll-off

The same ideology can be applied to the loop gain. This may be useful to limit the closed-loop bandwidth of $PK/(1 - PK)$ which is common in tracking control problems. This transfer function is obtained by applying multiplicative uncertainty at the plant output as shown in Figure 3.6 so that the uncertainty on the plant has the form

$$P_\Delta = (1 + \Delta)P.$$

Again, at high frequencies Δ will be large so the loop gain magnitude must be small. Assuming $|PK| \ll 1$, the closed-loop transfer function from w to z is approximately

$$\left|\frac{PK}{1 - PK}\right|(\omega) \approx |PK(\omega)|.$$

In [32], the loop gain roll-off constraint was proposed,

$$\left|\frac{PK}{1 - PK}\right|(\omega) \approx |PK(\omega)| < \left(\frac{\omega}{\omega_{co}}\right)^{-\frac{|\alpha|}{20}}$$

where ω_{co} is the crossover frequency and α is the roll-off slope in dB.

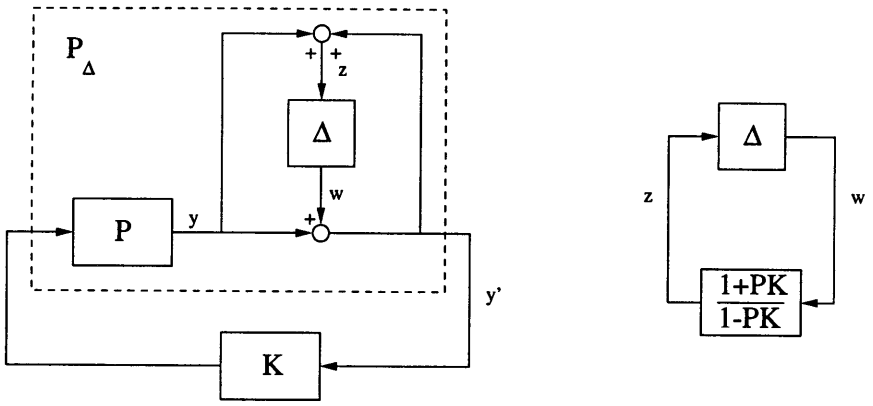

Figure 3.8: Mixed uncertainty (at plant output).

3.5 Gain and Phase Margin Constraints

Gain and phase margin constraints can be incorporated into the linear controller design problem by constraining the gain of a fictitious closed-loop input/output channel created by applying an uncertainty between the plant and the controller. One effective way to do this is by applying a mixed multiplicative and divisive uncertainty [11] at the plant output as shown in Figure 3.8 so that the uncertainty on the plant has the form

$$P_\Delta = P\left(\frac{1+\Delta}{1-\Delta}\right),$$

where $(1+\Delta)/(1-\Delta)$ can be interpreted as a perturbation on the loop gain PK injected between y and y'. By the small gain theorem, stability is guaranteed if $|L| < 1/|\Delta|$ where L is the transfer function seen by Δ or $(1+PK)/(1-PK)$. More specifically if Δ is of the form $re^{i\theta}$ where $\theta \in [0, 2\pi]$, then stability is guaranteed if

$$\left|\left(\frac{1+PK}{1-PK}\right)(\omega)\right| < \frac{1}{r(\omega)} \qquad \forall\omega.$$

Therefore, stability is guaranteed for any perturbation in the loop gain which falls inside the complex-plane circle $(1+re^{j\theta})/(1-re^{j\theta})$ where $\theta \in [0, 2\pi]$.

The gain margin is the range of tolerable gains between y and y' in which stability is maintained. Figure 3.9 shows the transfer function between y and y' is a pure gain when the phase of the uncertainty is 0 or 180 degrees ($\theta = 0, \pi$). If r_{min} is lower

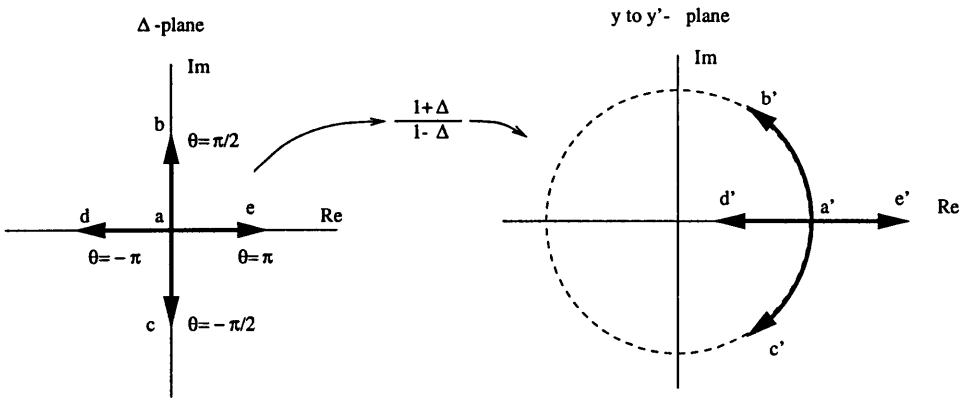

Figure 3.9: Map of $(1+\Delta)/(1-\Delta)$.

bound on $r(\omega)$,

$$r(\omega) \geq r_{min} \qquad \forall \omega,$$

then the gain margin is computed directly by letting $r = r_{min}$ and $\theta = 0, \pi$,

$$GM = \left[\frac{1 - r_{min}}{1 + r_{min}}, \frac{1 + r_{min}}{1 - r_{min}}\right].$$

Similarly, the phase margin is the range of tolerable phases between y and y' in which stability is maintained. Figure 3.9 shows the transfer function between y and y' is a pure phase (with unit magnitude) when the phase of the uncertainty is $\theta = \pm\pi/2$. Hence, the phase margin is computed by letting $r = r_{min}$ with $\theta = \pm\pi/2$,

$$PM = \left[\angle\frac{1 - jr_{min}}{1 + jr_{min}}, \angle\frac{1 + jr_{min}}{1 - jr_{min}}\right].$$

Through a simple trigonometric identity [2], the phase margin calculation simplifies to,

$$PM = [-\theta_{PM}, \theta_{PM}] \text{ where } \theta_{PM} = 2\tan^{-1}(r_{min}).$$

In fact, each r_{min} corresponds to an entire region of allowable simultaneous gain and phase perturbations as shown in Figure 3.10 where $(1 + r_{min}e^{j\theta})/(1 - r_{min}e^{j\theta})$ is plotted for several values of r_{min} with θ varying between 0 and π. The interior of each ellipse shows allowable gain and phase perturbations for y which will still guarantee stability. The numerical values adjacent to each ellipse are $1/r_{min}$ in decibels which

[2] $\tan 2\alpha = \frac{2\tan\alpha}{1-\tan^2\alpha}$ where $\tan\alpha = r$ and $\alpha = \theta/2$

are consistent with the bound on $(1+PK)/(1-PK)$ required to guarantee stability for gain and phase perturbations inside the ellipse. Gain and phase margins for each value of $1/r_{min}$ are read at the intersection of the ellipses with the 0 degrees and 0 dB axes respectively.

The nice symmetry about 0 dB is an appealing characteristic of the mixed multiplicative divisive uncertainty. Gain and phase margin constraints derived using the pure multiplicative or divisive uncertainties result in asymmetric gain and phase curves shown in Figures 3.11 and 3.12 respectively. However, the divisive uncertainty based constraints have a nice interpretation on the Nyquist plot, and are used in [4] to formulate M-circle constraints. A M-circle defines a neighborhood of radius M in the Nyquist plot about the critical point $1+j0$ (or $-1+j0$ assuming negative feedback) in which the loop gain is prohibited to enter [43]. Constraining the closed-loop transfer function seen by the divisive uncertainty, or $1/(1-PK)$, to be less than $1/M$ is equivalent to constraining the loop gain to stay outside of the M-circle neighborhood. This result is easy to see from the application of the small gain theorem:

$$\left|\left(\frac{1}{1-PK}\right)(\omega)\right| < \frac{1}{M} \qquad \forall\omega$$

or equivalently,

$$|(1-PK)(\omega)| > M \qquad \forall\omega.$$

In the complex plane, this is

$$(\Re[PK(\omega)]-1)^2 + (\Im[PK(\omega)])^2 > M^2,$$

which is the equation of a circle centered at $1+j0$ expressed as an inequality. Hence, $PK(\omega)$ must stay outside the circle centered at $1+j0$ with radius M as shown in Figure 3.13.

To enforce gain and phase margin constraints it is only necessary to constrain L at frequencies where the phase and gain crossover is expected to occur rather than the entire frequency spectrum. Figure 3.14 shows and example where L is constrained in anticipated gain and phase crossover frequency bands. In the band of anticipated gain crossover, L is constrained to be less than 11.43 dB corresponding to ± 3 dB

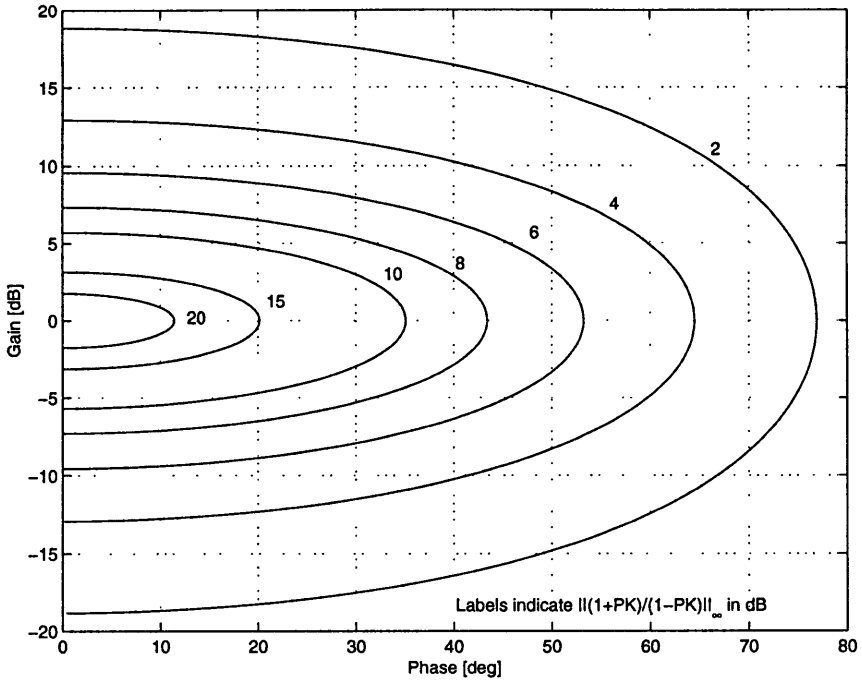

Figure 3.10: Guaranteed margins from constraints on mixed uncertainty.

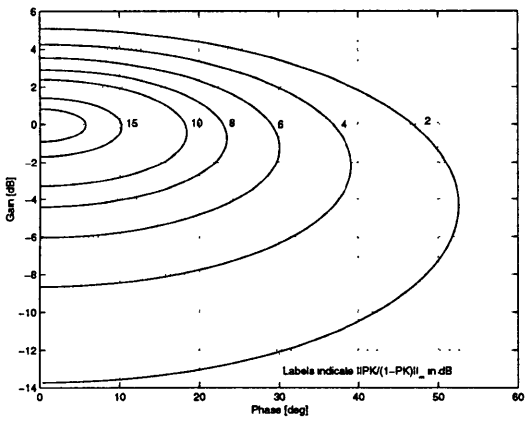

Figure 3.11: Guaranteed margins from constraints on multiplicative uncertainty.

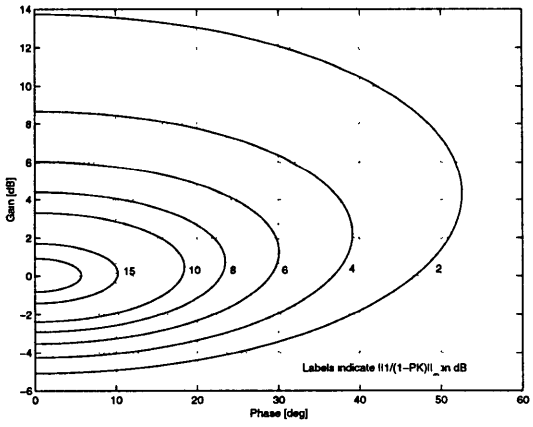

Figure 3.12: Guaranteed margins from constraints on divisive uncertainty.

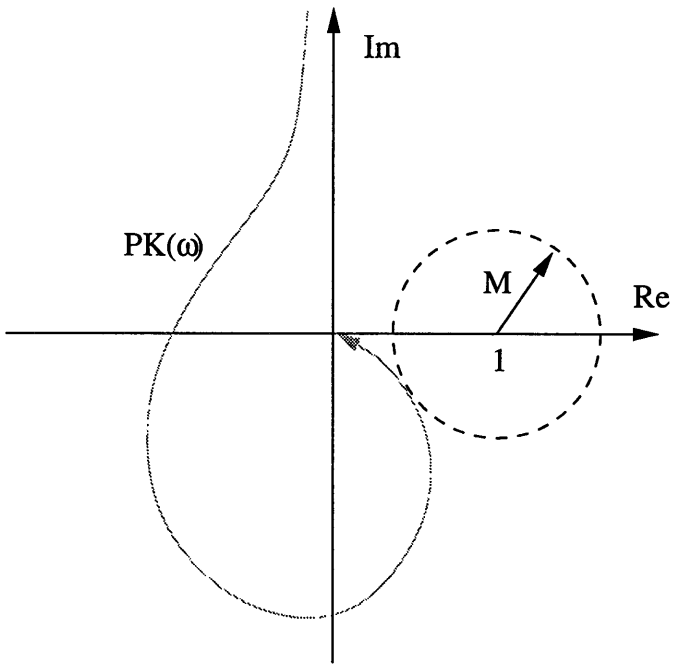

Figure 3.13: M-circle on Nyquist plot assuming positive feedback.

gain margin. Similarly, in the band of anticipated phase crossover, L is constrained to be less than 15.34 dB corresponding to 30° phase margin. The gain and phase margins as a result of these constraints are discussed in more detail in Section 6.6, and illustrated in Figure 6.12.

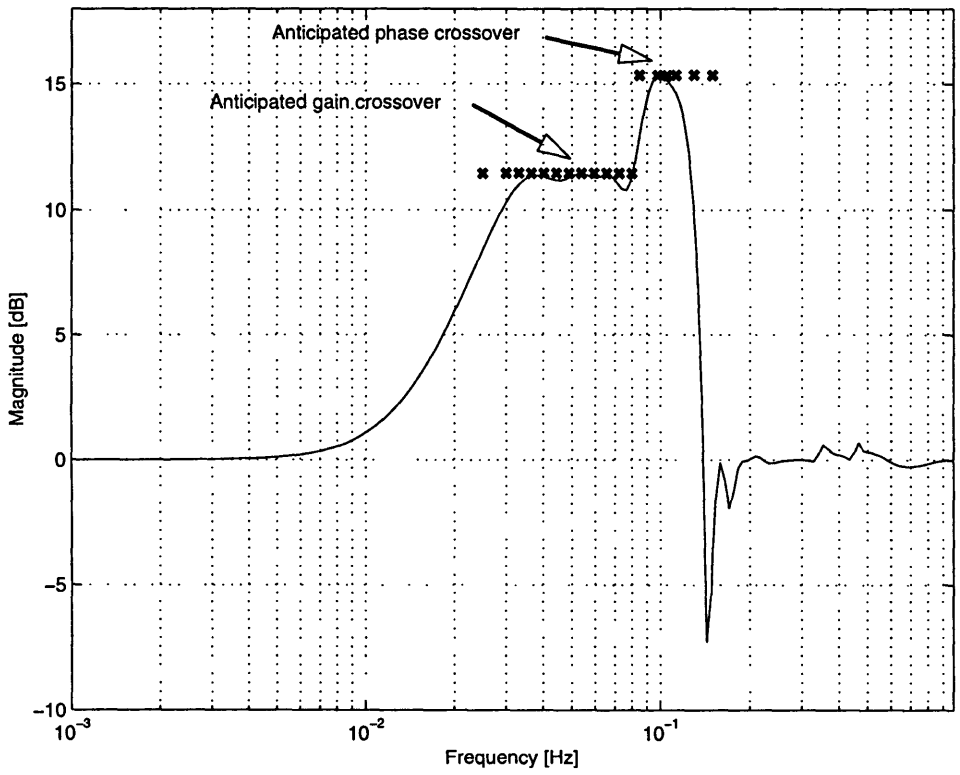

Figure 3.14: Example constraint on $(1 + PK)/(1 - PK)$ at crossover frequencies.

Chapter 4

Generalized Orthonormal Basis Functions

Solving the constrained $\mathcal{H}_2$ problem relies on approximating the infinite-dimensional system Q with an affine combination of a finite number of basis functions. An alternative, non-convex approach would be to represent Q as a finite length partial fraction expansion, where the parameters are the residue and poles of the expansion. A good model for optimization should:

- preserve the convexity of the problem.
- have good numerical properties such as convergence and conditioning.

In this work the expansion of Q is restricted to be linear combinations of the basis functions. Therefore Q will be affine over the free coefficients and convexity of the problem is preserved. Furthermore, only orthogonal basis functions are considered which have superior numerical properties to non-orthogonal basis functions.

The class of orthogonal basis functions have been studied for at least a century. Their potential in linear system synthesis has been realized by Wiener and Lee [38] in the 1930's. Historically, some commonly used and studied orthogonal basis functions include the FIR, Laguerre, and Kautz functions. These basis functions restrict all of the basis function poles to be at the same location on the open unit disk in the z-plane. For example, all of the FIR poles are at the origin, while the Laguerre

Table 4.1: Basis function pole location in z-plane.

FIR	$\xi_n = 0$	$n = 1, 2, \cdots$
Laguerre	$\xi_n = a$	$n = 1, 2, \cdots$
Kautz	$\xi_{2n-1} = \xi_1, \xi_{2n} = \xi_2$	$n = 1, 2, \cdots$
GOBF	$\xi_n =$ arbitrary	$n = 1, 2, \cdots$

functions move the poles from the origin to a point a on the real axis, and the Kautz functions move the poles to a real or complex conjugate pole pair location ξ_1 and ξ_2 that satisfy a quadratic equation. In the last 10 years, vigorous activity in the study of these functions helped to rediscover a method of building orthogonal functions with fixed pole locations anywhere on the open unit disk [34, 54]. These functions are referred to as Generalized Orthonormal Basis Functions (GOBF) and they generalize the FIR, Laguerre, and Kautz functions. The pole locations for each basis function are summarized in Table 4.1.

This chapter reviews the recent developments of the GOBF that have been playing an increasingly important role in system identification [7, 31, 33, 50, 53, 55, 65, 68]. and in linear controller design [4, 40, 46, 56], and provides explicit real state-space representations for these functions through two approaches. The first approach developed by the author is a direct construction from the transfer function representation of the GOBF provided in [54]. The second approach developed in [34] cascades balanced realizations of simple Laguerre and Kautz building blocks. In both developments, it is shown that representations with mixed real and complex conjugate poles can be built with series interconnections of two simple first and second order state-space systems. The series connection naturally produces a realization with a lower diagonal A. Simple system identification examples are provided.

4.1 Transfer Function Construction

The orthogonal basis function structure can be used to approximate an infinite dimensional system by a finite dimensional series expansion,

$$y(z) \approx \left(\sum_{n=0}^{N-1} \phi_n F_n(z) \right) u(z)$$

where $\{\phi_n\}_{n=0,...,N-1}$ are the parameters and $\{F_n(z)\}_{n=0,...,N-1}$, are the basis functions. The linear-in-the-parameters feature makes them a natural choice for optimization problems such as minimizing the error between a transfer function and frequency data, or designing an optimal filter subject to convex constraints. In [54], a simple transfer function construction for the complete GOBF are developed. The development of the GOBF are reviewed below.

A set of basis functions $\{F_n(z)\}$ is complete if it spans the space of all stable realizable transfer functions, and is orthonormal if $\sum_{k=0}^{\infty} f_i[k] f_j[k] = \delta_{ij}$, where $f_n[k]$ is the impulse response of $F_n(z)$ and δ_{ij} is the Kronecker delta function. The equivalent orthogonality condition in the frequency domain is $< F_i(z), F_j(z) >= \delta_{ij}$, where $< F_i(z), F_j(z) >= \frac{1}{2\pi} \int_{-\pi}^{\pi} F_i(e^{i\omega}) F_j(e^{i\omega})^* \, d\omega$. In [54], the complete GOBF model is derived as

$$F_n(z) = \left(\frac{\sqrt{1 - |\xi_n|^2}}{z - \xi_n} \right) \prod_{k=0}^{n-1} \left(\frac{1 - \xi_k^* z}{z - \xi_k} \right)$$

where ξ^* denotes the complex conjugate of ξ. This construction allows the arbitrary placement of poles $\xi_0, \xi_1, ..., \xi_{p-1}$ within the unit circle, rather than restricting pole placement to a single location as is the case with the FIR, Laguerre, and Kautz models. The filter under the product from $k = 0$ to $n - 1$ has the property $|H(\omega)| = 1$ or $H(z)H(1/z) = 1$ and is said to be all-pass. Hence the basis function $F_n(z)$ is the cascade of an all-pass filter with a low-pass filter.

When complex poles are added to the basis, the impulse response $f_n[k]$ can become complex which is meaningless for real systems. For example, if a complex pole is added to the basis without its conjugate partner, the impulse response of that basis function will be complex. In [54], conditions that guarantee real impulse responses are considered when complex conjugate pairs are added to the basis. Consider the

basis functions F_n and F_{n+1} with complex impulse responses associated with poles ξ_n and ξ_{n+1} where $\xi_n = \xi_{n+1}^\star$. A linear transformation can be selected to create new basis functions F_n' and F_n'' with real impulse responses as follows

$$F_n'(z) = \frac{\sqrt{1-|\xi_n|^2}(\beta z + \mu)}{z^2 - (\xi_n + \xi_n^\star)z + |\xi_n|^2} \prod_{k=0}^{n-1} \left(\frac{1 - \xi_k^\star z}{z - \xi_k} \right)$$

$$F_n''(z) = \frac{\sqrt{1-|\xi_n|^2}(\beta' z + \mu')}{z^2 - (\xi_n + \xi_n^\star)z + |\xi_n|^2} \prod_{k=0}^{n-1} \left(\frac{1 - \xi_k^\star z}{z - \xi_k} \right)$$

where β, μ, β' and μ' are real coefficients determined by solving the following equations

$$x^T M x = |1 - \xi_n^2|^2 \tag{4.1}$$

where

$$x \equiv (\beta, \mu)^T, M \equiv \begin{pmatrix} 1 + |\xi_n|^2 & 2Re\{\xi_n\} \\ 2Re\{\xi_n\} & 1 + |\xi_n|^2 \end{pmatrix},$$

and

$$\begin{pmatrix} \beta' \\ \mu' \end{pmatrix} = \frac{1}{\sqrt{1-\alpha^2}} \begin{pmatrix} \alpha & 1 \\ -1 & -\alpha \end{pmatrix} \begin{pmatrix} \beta \\ \mu \end{pmatrix} \tag{4.2}$$

where

$$\alpha \equiv \frac{\xi_n + \xi_n^\star}{1 + |\xi_n|^2}.$$

The eigenvalues of M in Equation (4.1) are $\lambda_1, \lambda_2 = |1 \pm \xi_n|^2 > 0$. Hence, M is a real, symmetric, positive definite matrix and thus diagonalizable [64]. The solutions lie on an ellipse

$$\lambda_1 (v_1^T x)^2 + \lambda_2 (v_2^T x)^2 = |1 - \xi_n^2|^2 \tag{4.3}$$

where v_1 and v_2 are the eigenvectors of M,

$$v_1 = \begin{pmatrix} \frac{1}{\sqrt{2}} \\ \frac{1}{\sqrt{2}} \end{pmatrix}, v_2 = \begin{pmatrix} \frac{1}{\sqrt{2}} \\ -\frac{1}{\sqrt{2}} \end{pmatrix}.$$

For example, a solution to Equation (4.3), corresponding to one of the principal axes of the ellipse, is when

$$\beta = \mu = \frac{\sqrt{2}}{2} \frac{|1 - \xi_n^2|}{|1 + \xi_n|}.$$

Table 4.2: Example pole location in z-plane.

$n = 0$	$0.88637 - 0.22336i$
$n = 1$	$0.88637 + 0.22336i$
$n = 2$	0.80754
$n = 3$	0.76818

4.1.1 Example Impulse and Frequency Response

To help visualize the GOBF in the frequency and time domains, consider the basis functions corresponding to four randomly selected poles:

- real poles at 0.34 and 0.42 Hz.
- complex conjugate pole pair at 0.418 Hz and with damping $\zeta = 0.3420$.

Assuming a 0.1 second time step, these poles correspond to the discrete pole locations listed in Table 4.2. The GOBF corresponding to these poles are

$$\begin{aligned}
F_0(z) &= \frac{0.07186(z+1)}{z^2 - 1.773z + 0.8355}, \\
F_1(z) &= \frac{0.5447(z-1)}{z^2 - 1.773z + 0.8355}, \\
F_2(z) &= \frac{0.5899}{(z-0.8075)} \left(\frac{0.8355z^2 - 1.773z + 1}{z^2 - 1.773z + 0.8355} \right), \\
F_3(z) &= \frac{0.6402}{(z-0.7682)} \left(\frac{1 - 0.8075z}{z - 0.8075} \right) \left(\frac{0.8355z^2 - 1.773z + 1}{z^2 - 1.773z + 0.8355} \right),
\end{aligned}$$

where $F_0(z) \equiv F_0'(z)$ and $F_1(z) \equiv F_0''(z)$. The impulse and frequency responses of the GOBF with these pole locations are shown in Figures 4.1, 4.2 respectively.

4.2 State-Space Realization: Direct Approach

A state-space realization of the general orthonormal basis can be derived directly from the transfer function construction by assuming a particular block diagram structure. One such structure is a series connection of SIMO (single-input/multiple-output)

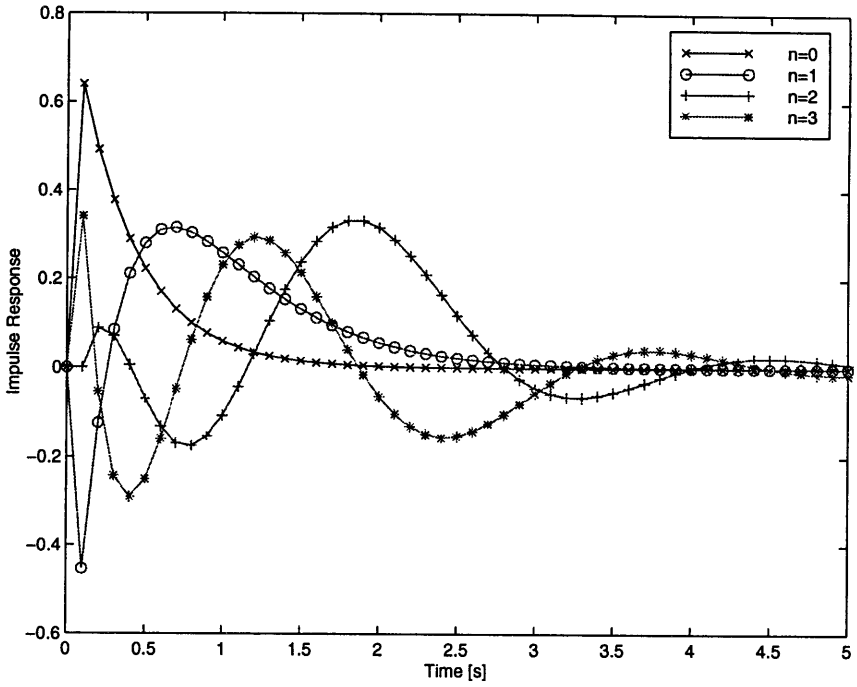

Figure 4.1: Example impulse response of the GOBF.

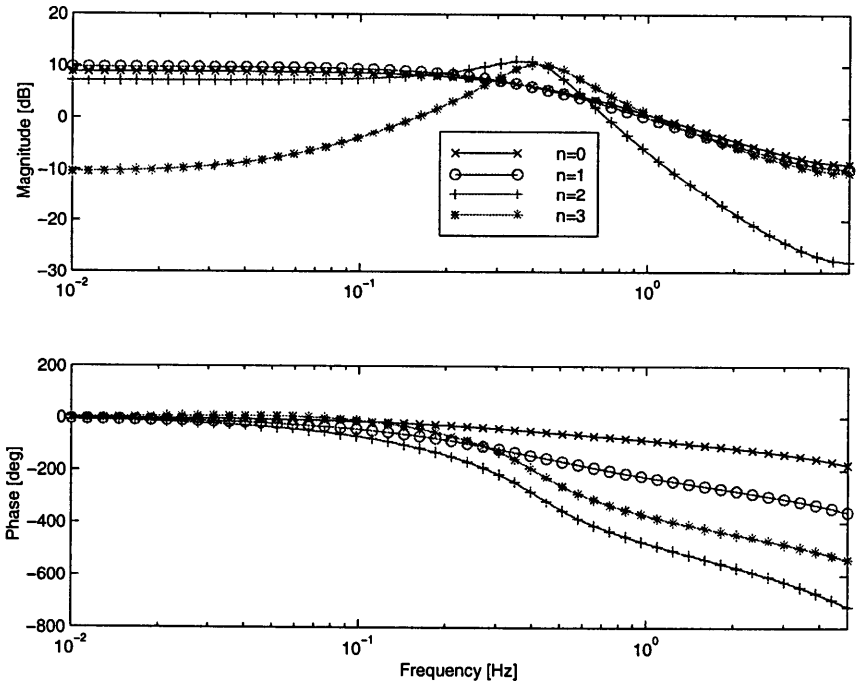

Figure 4.2: Example frequency response of the GOBF.

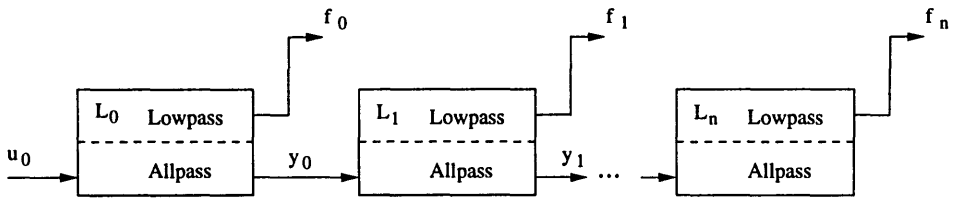

Figure 4.3: Series connection structure.

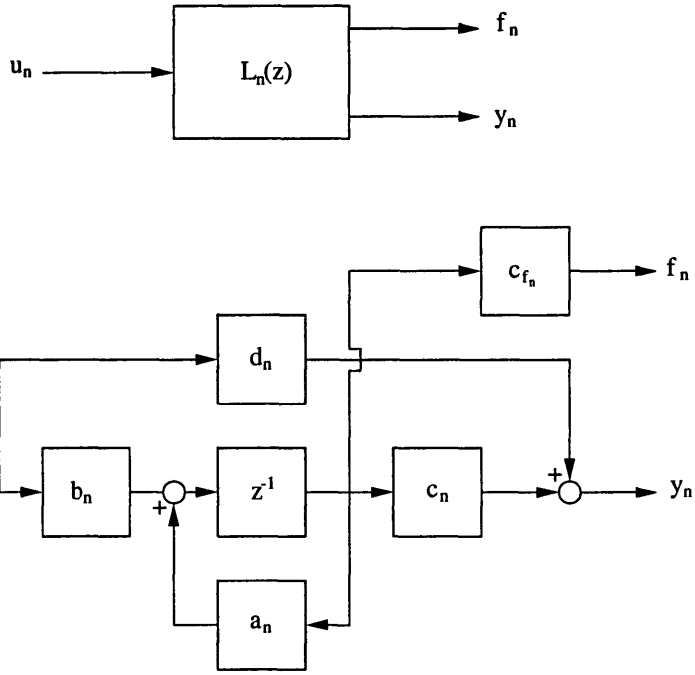

Figure 4.4: First order pole block diagram.

low-pass/all-pass blocks as shown in Figure 4.3, where the top channel(s) are simply low-pass filters with first or second order roll-off, and the bottom channel is an all-pass filter. With this structure, finding a state-space realization for a system with N basis functions is reduced to finding the state-space realization for block diagrams 4.4 and 4.5, and using simple state-space interconnection rules.

4.2.1 First Order Pole Representation

The structure in Figure 4.3 implies that the addition of a real pole is equivalent to multiplying by the 2×1 transfer function matrix $L_n(z)$ depicted by Figure 4.4, or

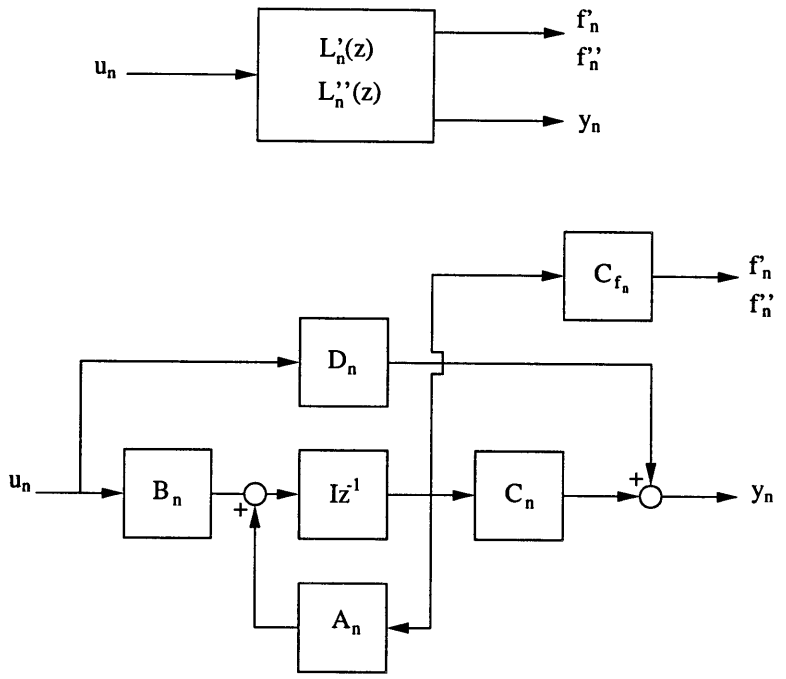

Figure 4.5: Second order pole block diagram.

more precisely

$$L_n(z) = [\ \frac{\sqrt{1-|\xi_n|^2}}{z-\xi_n} \quad \frac{1-\xi_n^* z}{z-\xi_n}\ ]^T$$

A state-space model for this transfer function matrix is illustrated in Figure 4.4, with

$$\begin{aligned} a_n &= \xi_n \\ b_n &= 1 \\ c_n &= \eta_n \\ c_{f_n} &= \sqrt{\eta_n} \\ d_n &= -\xi_n \end{aligned}$$

where $\eta_n \equiv 1 - |\xi_n|^2$.

4.2.2 Second Order Pole Representation

The addition of a second order pole is equivalent to multiplying by the 3×1 transfer function matrix depicted in Figure 4.5, or

$$L_n(z) = [\ \frac{\sqrt{1-|\xi_n|^2}(\beta z-\mu)}{z^2-(\xi_n+\xi_n^*)z+|\xi_n|^2} \quad \frac{\sqrt{1-|\xi_n|^2}(\beta' z-\mu')}{z^2-(\xi_n+\xi_n^*)z+|\xi_n|^2} \quad \frac{1-(\xi_n+\xi_n^*)z+|\xi_n|^2 z^2}{z^2-(\xi_n+\xi_n^*)z+|\xi_n|^2}\ ]^T$$

A state-space model for this transfer function matrix is illustrated in Figure 4.5, with

$$\begin{aligned} A_n &= \begin{bmatrix} 0 & 1 \\ -|\xi_n|^2 & 2Re\{\xi_n\} \end{bmatrix} \\ B_n &= \begin{bmatrix} 0 \\ 1 \end{bmatrix} \\ C_n &= \begin{bmatrix} (1-|\xi_n|^4) & -2Re\{\xi_n\}\eta_n \end{bmatrix} \\ C_{f_n} &= \sqrt{\eta_n} \begin{bmatrix} \mu & \beta \\ \mu' & \beta' \end{bmatrix} \\ D_n &= |\xi_n|^2 \end{aligned}$$

where $\eta_n \equiv 1 - |\xi_n|^2$. Notice that all of the coefficients in the state-space are real.

4.2.3 Series Interconnection

A state-space model of the basis functions with mixed real and complex poles can be derived by interconnecting the simple first and second order low-pass/all-pass blocks above using the following rule. Given $L(z)_n$ and $L(z)_{n+1}$ with state-space realizations

$$\left[\begin{array}{c|c} A_n & B_n \\ \hline C_{f_n} & 0 \\ C_n & D_n \end{array}\right]$$

and,

$$\left[\begin{array}{c|c} A_{n+1} & B_{n+1} \\ \hline C_{f_{n+1}} & 0 \\ C_{n+1} & D_{n+1} \end{array}\right]$$

respectively. Then, $L(z)_n L(z)_{n+1}$ has realization $(\tilde{A}, \tilde{B}, \tilde{C}, \tilde{D})$ where

$$\begin{aligned} \tilde{A} &= \begin{bmatrix} A_n & 0 \\ B_{n+1}C_n & A_{n+1} \end{bmatrix} \\ \tilde{B} &= \begin{bmatrix} B_n \\ B_{n+1}D_n \end{bmatrix} \\ \tilde{C} &= \begin{bmatrix} C_{f_n} & 0 \\ 0 & C_{b_{n+1}} \\ D_{n+1}C_n & C_{n+1} \end{bmatrix} \end{aligned}$$

$$\tilde{D} = \begin{bmatrix} 0 \\ 0 \\ D_{n+1}D_n \end{bmatrix}$$

The new system has three outputs f_n, f_{n+1}, y.

A state-space model for an arbitrary number of mixed real and complex poles is built using the above rule recursively. For example, consider building a state-space model with 4 first or second order blocks. The state-space realization $(\tilde{A}, \tilde{B}, \tilde{C}, \tilde{D})$ would be

$$\tilde{A} = \begin{bmatrix} A_0 & 0 & 0 & 0 \\ B_1C_0 & A_1 & 0 & 0 \\ B_2D_1C_0 & B_2C_1 & A_2 & 0 \\ B_3D_2D_1C_0 & B_3D_2C_1 & B_3C_2 & A_3 \end{bmatrix}$$

$$\tilde{B} = \begin{bmatrix} B_0 \\ B_1D_0 \\ B_2D_1D_0 \\ B_3D_2D_1D_0 \end{bmatrix}$$

$$\tilde{C} = \begin{bmatrix} C_{b_0} & 0 & 0 & 0 \\ 0 & C_{b_1} & 0 & 0 \\ 0 & 0 & C_{b_2} & 0 \\ 0 & 0 & 0 & C_{b_3} \\ D_3D_2D_1C_0 & D_3D_2C_1 & D_3C_2 & C_3 \end{bmatrix}$$

$$\tilde{D} = \begin{bmatrix} 0 \\ 0 \\ 0 \\ D_3D_2D_1D_0 \end{bmatrix}.$$

The last row in $\tilde{C}$ and $\tilde{D}$ would be discarded when the recursion is terminated. Close inspection of the above realization shows that there is no conflict in dimension by mixing first and second order blocks.

4.2.4 Special Case I.: Real Pole State-Space Representation

The $N \times 1$ state-space system $(A, B, C, 0)$ representation of a orthonormal basis with strictly real poles is found by

$$A_{ij} = \begin{cases} 0 & \text{for } i < j \\ \xi_{j-1} & \text{for } i = j \\ \eta_{j-1} & \text{for } i = j+1 \\ \eta_{j-1} \prod_{k=j}^{i-2}(-\xi_k) & \text{for } i > j+1 \end{cases}$$

$$B_i = \begin{cases} 1 & \text{for } i = 1 \\ \prod_{k=0}^{i-2}(-\xi_k) & \text{for } i > 1 \end{cases}$$

$$C_{ij} = \begin{cases} \sqrt{\eta_{j-1}} & \text{for } i = j \\ 0 & \text{for } i \neq j. \end{cases}$$

4.2.5 Special Case II.: Complex Pole State-Space Representation

The $N \times 1$ state-space system $(A, B, C, 0)$ representation of a orthonormal basis with strictly complex conjugate poles is

$$A_{\hat{i},\hat{j}} = \begin{cases} 0_{2\times 2} & \text{for } i < j \\ \begin{bmatrix} 0 & 1 \\ -|\xi_{j-1}|^2 & 2Re\{\xi_{j-1}\} \end{bmatrix} & \text{for } i = j \\ \begin{bmatrix} 0 & 0 \\ (1-|\xi_{j-1}|^4) & -2Re\{\xi_{j-1}\}\eta_{j-1} \end{bmatrix} & \text{for } i = j+2 \\ \begin{bmatrix} 0 & 0 \\ (1-|\xi_{j-1}|^4) & -2Re\{\xi_{j-1}\}\eta_{j-1} \end{bmatrix} \prod_{k=j+1}^{i-2}(-\xi_k^*) & \text{for } i > j+2 \end{cases}$$

$$B_{\hat{i}} = \begin{cases} \begin{bmatrix} 0 \\ 1 \end{bmatrix} & \text{for } i = 1 \\ \begin{bmatrix} 0 \\ 1 \end{bmatrix} \prod_{k=0}^{i-2}(-\xi_k^*) & \text{for } i > 1 \end{cases}$$

$$C_{\hat{i},\hat{j}} = \begin{cases} \sqrt{\eta_{j-1}} \begin{bmatrix} \mu_{j-1} & \beta_{j-1} \\ \mu'_{j-1} & \beta'_{j-1} \end{bmatrix} & \text{for } i = j \\ 0_{2\times 2} & \text{for } i \neq j \end{cases}$$

where $i = 1, 3, 5, ..., N-1$, $j = 1, 3, 5, ..., N-1$, $\hat{i} = [i, i+1]^T$ and $\hat{j} = [j, j+1]$.

4.3 State-Space Realization: Balanced Approach

Perhaps a more elegant way to derive a state-space model for the GOBF is found in the developmental theory of the generalized orthonormal basis derived by Heuberger et. al. [34]. This approach uses special balanced realizations to construct the GOBF. A realization (A, B, C, D) of a stable system is said to be (internally) balanced if the solutions to the Lyapunov equations $APA^\star + BB^\star = P$ and $A^\star QA + C^\star C = Q$ satisfy $P = Q = \Sigma$, where $\Sigma = diag(\sigma_1, \sigma_2, \ldots, \sigma_n)$, $\sigma_1 \geq \ldots \geq \sigma_n$ is a diagonal matrix of the positive Hankel singular values. The main result of this work is embodied in the following theorem.

Theorem. *Let $G(z)$ be a scalar inner transfer function with McMillan degree $n > 0$, having a minimal balanced realization (A, B, C, D). Denote*

$$V_k(z) = z(zI - A)^{-1}BG^k(z).$$

Then the sequence of scalar rational functions $\{e_i^T V_k(z)\}_{i=1,\ldots,n,;k=0,\ldots,\infty}$ forms an orthonormal basis for the Hilbert space $\mathcal{H}_2$.

In the above theorem, e_i is the standard basis vector of zeros with 1 in the i-th location, inner can be read as all-pass, and the McMillan degree [43] is the number of poles in the transfer function. This theorem states that given an n-th order all-pass filter and its minimal balanced realization (A, B, C, D), a complete orthonormal basis for the class of square-integrable functions (functions with finite $\mathcal{H}_2$ norm) is given by $\{e_i^T V_k(z)\}_{i=1,\ldots,n,;k=0,\ldots,\infty}$. With this basis, the poles of $G(z)$ are infinitely repeated. In this work, the idea is to pick n large enough so that the basis made up of distinct pole locations (i.e., $k = 0$) is a good basis for the square-integrable functions. The GOBF with distinct poles is

$$V_0(z) = z(zI - A)^{-1}B,$$

where the i-th basis function is $\{e_i^T V_0(z)\}_{i=1,\ldots,n}$. Notice that this implies that the realization of $G(z)$ has the form $(A, B, I, 0)$ and $V_0(z) = zG(z)$.

The purpose of the forward shift z on $V_0(z)$ is seen through a corollary in [34].

Corollary. *Let G be an inner function with McMillan degree n as in the Theorem, with a corresponding sequence of basis functions $V_k(z)$. Then for every proper stable transfer function $H \in \mathcal{H}_2$ there exists unique $\theta \in \mathrm{R}$, and $\Phi = \{\Phi_k\}_{k=0,1,\ldots} \in \ell_2^{1\times n}[0,\infty)$, such that*

$$H(z) = \theta + z^{-1} \sum_{k=0}^{\infty} \Phi_k V_k(z),$$

where θ and Φ_k are the orthogonal expansion coefficients of $H(z)$.

The relationship between $F(z)$ and $V_0(z)$ is now seen,

$$F(z) = z^{-1} V_0(z) = G(z),$$

where $F(z) \equiv [\, F_0(z) \quad F_1(z) \quad \cdots \quad F_{N-1}(z) \,]^T$. The Corollary also says that a constant should be added to the basis with coefficient θ to model systems with feedthrough[1] (non-zero D).

To construct a state-space for the GOBF using Theorem 4.3, one must derive the minimal balanced realization for the n-th order all-pass filter $G(z)$ with arbitrary stable poles. This is made easy through the theory of orthogonal, all-pass filters [63]. An orthogonal, all-pass filter is defined to be a state-space realization of on all-pass filter with orthonormal states. A system has orthonormal states if and only if the state covariance matrix $P = E\{x(t)x(t)^T\}$ is identity[2] for zero mean unit variance white noise input. The state covariance is computed from the discrete Lyapunov equation,

$$P = APA^T + BB^T.$$

Hence it follows that for orthogonal systems,

$$AA^T + BB^T = I.$$

[1] Recall that the basis functions derived in Section 4.2 had a zero D term.

[2] P can always be made identity with the proper state transformation.

Because the system is also all-pass, two additional conditions are imposed on the state-space (see Appendix 10A of [63]),

$$\begin{aligned} CC^T + DD^T &= I, \\ AC^T + BD^T &= 0. \end{aligned}$$

These three conditions imply that an orthogonal, all-pass filter has the property,

$$\begin{bmatrix} A & B \\ C & D \end{bmatrix} \begin{bmatrix} A & B \\ C & D \end{bmatrix}^T = I.$$

Constructing a n-th order all-pass network $G(z)$ with distinct poles is achieved through the following Proposition:

Proposition. *Cascading orthogonal, all-pass filters results in an orthogonal, all-pass filter.*

In the general case, the $G(z)$ can be constructed by cascading first and second order Laguerre and Kautz blocks respectively. The Laguerre and Kautz blocks are the simplest first and second order orthogonal, all-pass filters. Therefore through this Proposition, cascading l Laguerre and k Kautz blocks with arbitrary stable poles results in an $n = l + 2k$ order orthogonal, all-pass filter. Minimal balanced state-space realizations for the Laguerre and Kautz blocks are now described.

4.3.1 Laguerre Function Balanced Realization

A single, real pole, all-pass filter is given by the Laguerre function,

$$G(z) = \frac{1 - az}{z - a},$$

where a is real valued with $|a| < 1$. A minimal balanced state-space realization of G is [34],

$$\left[\begin{array}{c|c} a & \sqrt{\eta} \\ \hline \sqrt{\eta} & -a \end{array}\right],$$

where $\eta \equiv 1 - a^2$. Since the Laguerre function has a single pole, the orthogonality condition is trivially satisfied. The standard Laguerre model is a special case to the GOBF when using the single pole ($n = 1$) all-pass filter $G(z)$ in Theorem 4.3,

$$V_k(z) = z\frac{\sqrt{1-a^2}}{z-a}\left(\frac{1-az}{z-a}\right)^k, \quad |a| < 1.$$

The Laguerre function has a real pole at ξ_n when $a = \xi_n$.

4.3.2 Kautz Function Balanced Realization

A single, complex conjugate pole, all-pass filter is given by the two-parameter Kautz function,

$$G(z) = \frac{-cz^2 + b(c-1)z + 1}{z^2 + b(c-1)z - c},$$

where b and c are real valued with $|b| < 1$ and $|c| < 1$. A minimal balanced realization of G is [34],

$$\left[\begin{array}{cc|c} b & \sqrt{(1-b^2)} & 0 \\ c\sqrt{(1-b^2)} & -bc & \sqrt{(1-c^2)} \\ \hline \sqrt{(1-c^2)(1-b^2)} & -b\sqrt{1-c^2} & -c \end{array}\right].$$

This realization satisfies the orthogonality conditions. The two-parameter Kautz model is a special case of the GOBF when using the complex conjugate pole ($n = 2$) all-pass filter $G(z)$ in Theorem 4.3,

$$V_k(z) = z\left\{\begin{array}{l} \frac{\sqrt{(1-c^2)(1-b^2)}}{z^2+b(c-1)z-c}\left(\frac{-cz^2+b(c-1)z+1}{z^2+b(c-1)z-c}\right)^k \\ \frac{\sqrt{(1-c^2)}(z-b)}{z^2+b(c-1)z-c}\left(\frac{-cz^2+b(c-1)z+1}{z^2+b(c-1)z-c}\right)^k \end{array}\right. \quad |b| < 1,\ |c| < 1.$$

The two-parameter Kautz function has complex conjugate poles at ξ_n and $\xi_n^\star$ when picking $c = -|\xi_n|^2$ and $b = -2Re\{\xi_n\}/(c-1)$.

4.3.3 State-Space Construction

A minimal, balanced, orthogonal state-space realization for the most general case with multiple pole locations is constructed by cascading the Laguerre and Kautz function blocks at specified pole locations in any order,

$$G(z) = G_1(z)G_2(z)G_3(z)\cdots G_n(z),$$

where $G_1(z)$, $G_2(z)$,... and $G_n(z)$ can be single pole Laguerre blocks or complex conjugate pole Kautz blocks. The cascade of the realizations (A_1, B_1, C_1, D_1) and (A_2, B_2, C_2, D_2) is defined by

$$\left[\begin{array}{cc|c} A_1 & 0 & B_1 \\ B_2C_1 & A_2 & B_2D_1 \\ \hline D_2C_1 & C_2 & D_2D_1 \end{array}\right].$$

When the recursion is terminated, the C and D matrices are replaced by I and 0 respectively. The orthogonal basis functions are the states of the resulting realization (A, B, C, D):

$$\begin{aligned} A &= \begin{bmatrix} A_0 & 0 & 0 & \cdots \\ B_1C_0 & A_1 & 0 & \\ B_2D_1C_0 & B_2C_1 & A_2 & \\ \vdots & & & \ddots \end{bmatrix} \\ B &= \begin{bmatrix} B_0 \\ B_1D_0 \\ B_2D_1D_0 \\ \vdots \end{bmatrix} \\ C &= I \\ D &= 0. \end{aligned}$$

The realization for $G(z)$ is in the form $(A, B, I, 0)$ so that $V_0(z) = zG(z)$ and,

$$F(z) = G(z).$$

4.4 Pole Selection for Design

Selecting an efficient set of poles for the GOBF plays the most critical role in finding acceptable solutions to the constrained $\mathcal{H}_2$ problem. The GOBF introduce many more degrees of freedom over the FIR, Laguerre, or Kautz functions by allowing for arbitrary pole locations. These degrees of freedom can be exploited by the designer to minimize the number of basis functions needed to obtain a feasible design. However,

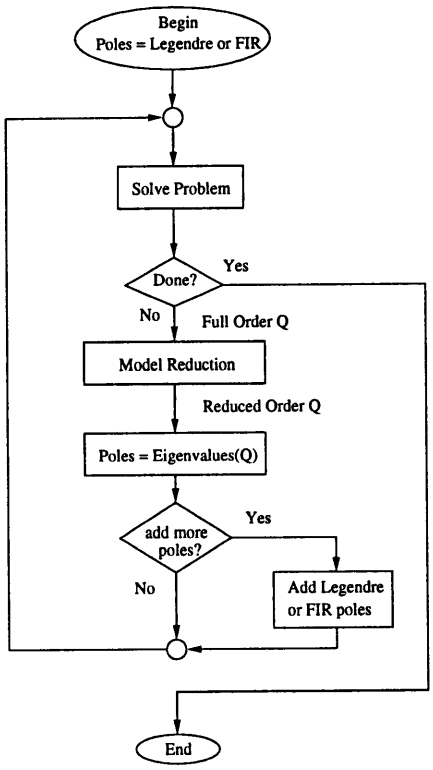

Figure 4.6: Recursive process for finding efficient GOBF for design.

it is unclear how to systematically select the most efficient basis for a given design problem. This section proposes a simple *ad hoc* method to find an efficient set of poles for the GOBF during the design process. This method is used to select the GOBF poles in the examples in this thesis.

Figure 4.6 illustrates the algorithm to find efficient GOBF for a given design problem. The algorithm starts with any basis which results in a feasible solution to the optimization problem. For example a high order FIR or Legendre [28] basis could be used to find an initial feasible solution. Then model reduction techniques are used to find a reduced order Q with new pole locations. The poles of the reduced order Q represent the pole locations of the GOBF for the next iteration. The designer has the option to include extra pole locations representing FIR or Legendre basis functions into the new pole set to increase the chance of finding a feasible solution on the next iteration. The algorithm is terminated when the designer feels that the minimum order basis is found that solves the optimization problem.

4.5 System Identification Examples

The utility of the unifying orthonormal basis is best illustrated with simple system identification examples. In essence, the design problem is a system identification problem of the optimal $Q(z)$.

4.5.1 Model-Matching with the GOBF

Consider minimizing the $\mathcal{H}_2$ norm of the error between a known transfer function $H(z)$ and linear combination of basis functions,

$$\min_{\phi} \|(H(z) - \phi^T F(z))\|_2$$

where $F(z) \equiv [\, F_0(z) \quad F_1(z) \quad \cdots \quad F_{N-1}(z) \,]^T$. A state-space solution to this problem is derived in [45]. In summary, using state-space interconnection rules the transfer function $H(z) - \phi^T F(z)$ can be represented as

$$H - \phi^T F \sim \left[\begin{array}{cc|c} A_H & 0 & B_H \\ 0 & A_F & B_F \\ \hline C_H & -\phi^T C_F & 0 \end{array}\right] = \left[\begin{array}{c|c} A & B \\ \hline C & 0 \end{array}\right],$$

where $H(z) = (A_H, B_H, C_H, 0)$ and $F(z) = (A_F, B_F, C_F, 0)$. In this example D is assumed to be zero with no loss of generality (D can easily be approximated by adding a constant to the basis). By definition $\|H - \phi^T F\|_2$ is,

$$\begin{aligned} \|H - \phi^T F\|_2^2 &= \mathrm{Tr}(CPC^T) \\ &= [C_H \;\; -\phi^T C_F] \left[\begin{array}{c} P_{11} P_{12} \\ P_{21} P_{22} \end{array}\right] \left[\begin{array}{c} C_H^T \\ -C_F^T \phi \end{array}\right], \end{aligned}$$

where P is the solution to the discrete Lyapunov equation,

$$APA^T + BB^T = P.$$

The optimal ϕ is found by solving the equation,

$$\frac{d}{d\phi} \|H - \phi^T F\|_2 = 0.$$

Hence,

$$\phi_{\text{opt}} = (C_F P_{22} C_F^T)^{-1} C_F P_{21} C_H^T.$$

For example, consider approximating the discrete transfer function

$$H(z) = \frac{-38.2048(z^3 - 2.833z^2 + 2.6802z - 0.84663)}{z^4 - 3.3121z^3 + 4.3304z^2 - 2.6291z + 0.63362}$$

using a 20th order FIR, Laguerre, and the GOBF bases.

The 20th order FIR approximation of $H(z)$ results in an $\mathcal{H}_2$ error of 83.17. Figure 4.7 shows the frequency response of the FIR approximation compared to $H(\omega)$. The FIR approximation shows approximately 35 dB error at low frequencies. Furthermore, the FIR basis does not approximate the 60 Hz resonance very well. The FIR basis has all of its poles fixed at the origin and the only degree of freedom is the basis order. Because the pole location and the order is fixed, this represents the best approximation possible.

A 20th order Laguerre basis with optimal time scale [23] results in an $\mathcal{H}_2$ error of 34.62. The optimal time scale for a particular system is derived by minimizing the truncation error associated with the finite Laguerre series expansion. Unfortunately the optimal time scale can only be computed if $H(z)$ is known a priori. For this problem the optimal time scale was computed to be $a = 0.6824$. Figure 4.7 shows the frequency response of the Laguerre approximation with optimal time scale compared to $H(\omega)$. Again large errors of approximately 29 dB occur at low frequencies. However, the Laguerre basis approximates the 60 Hz resonance much better than the FIR basis. The Laguerre basis has all of its poles fixed at the time scale a and therefore is completely specified by the choice of a and the order. Since a was picked to minimize the truncation error, this approximation represents the best 20th order Laguerre fit. However in real system identification problems, the optimal time scale would not be known and the Laguerre approximation would get worse.

The best approximation with 20 GOBF basis functions is harder to find since each pole location must be specified individually. The best GOBF basis would correspond to choosing the poles of $H(z)$ exactly which would result in zero $\mathcal{H}_2$ error. This is unreasonable for system identification because the poles of $H(z)$ are not know a

priori. One proposal for system identification is to search for the basis poles that minimizes the $\mathcal{H}_2$ error of the approximation. Unfortunately the map between the basis poles and the $\mathcal{H}_2$ error is nonlinear making the search for the optimal pole locations complicated. For this example, a simple search was executed based on a finite set of poles in an evenly spaced lattice of 121 pole locations. These pole locations are defined on a grid of natural frequencies vs. damping ratios which contain real and complex conjugate poles with natural frequencies between 10 and 100 Hz, and damping ratios[3] between 0.01 and 1. The GOBF was constructed by adding one real pole or complex conjugate pole pair at a time based on their individual $\mathcal{H}_2$ error. The best 20th order GOBF found with this coarse frequency/damping lattice results in an $\mathcal{H}_2$ error of 0.28. Figure 4.7 shows the frequency response of the GOBF approximation compared to $H(\omega)$. The GOBF approximation matches $H(\omega)$ well at all frequencies including the 60 Hz resonance. This example does not reflect the best approximation possible with the GOBF because of the arbitrary pole selection criterion used. With a finer frequency/damping grid, the GOBF approximation is expected to get better.

An illustration of the $\mathcal{H}_2$ error vs. basis order is shown in Figure 4.8. For comparison, two special cases of the GOBF are plotted in addition to the above cases, where the poles are restricted to be either all real or all complex conjugate. The real pole GOBF case, denoted Random Real GOBF, has randomly selected real poles between 10 and 100 Hz. The complex pole GOBF case, denoted Random GOBF, has randomly selected complex poles with the same frequency range but with random damping ratios between 0 and 1. The Figure shows that the recursive construction of the GOBF is the most effective means of minimizing the $\mathcal{H}_2$ error in system identification applications. For design applications it is more realistic to randomly pick the pole locations of the basis. The Figure shows that in this case, the GOBF with randomly selected complex conjugate pole location is the best choice for design.

[3]The real poles correspond to the grid line with damping ratio 1.

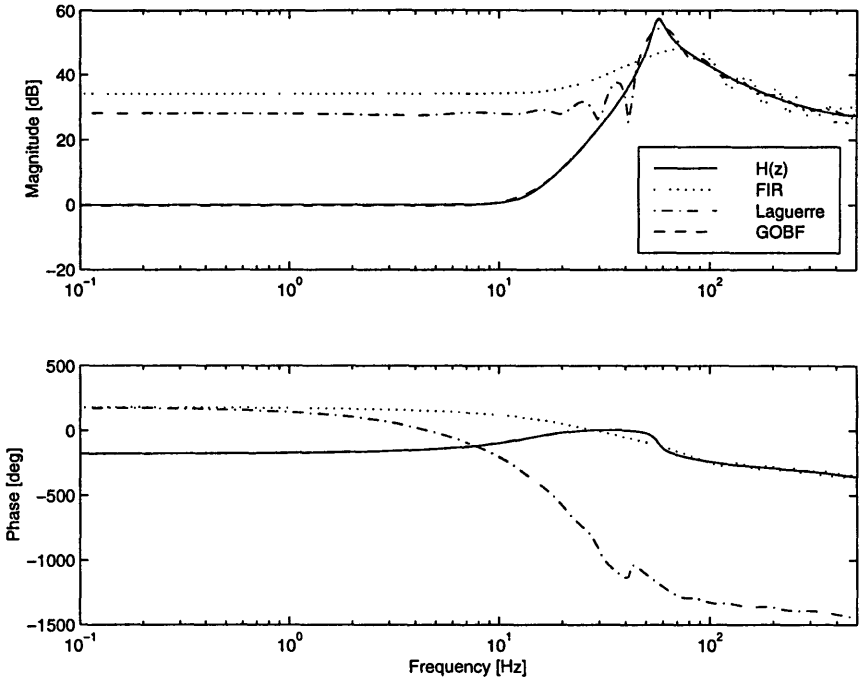

Figure 4.7: Comparison of FIR, Laguerre, and GOBF approximations of $H(z)$.

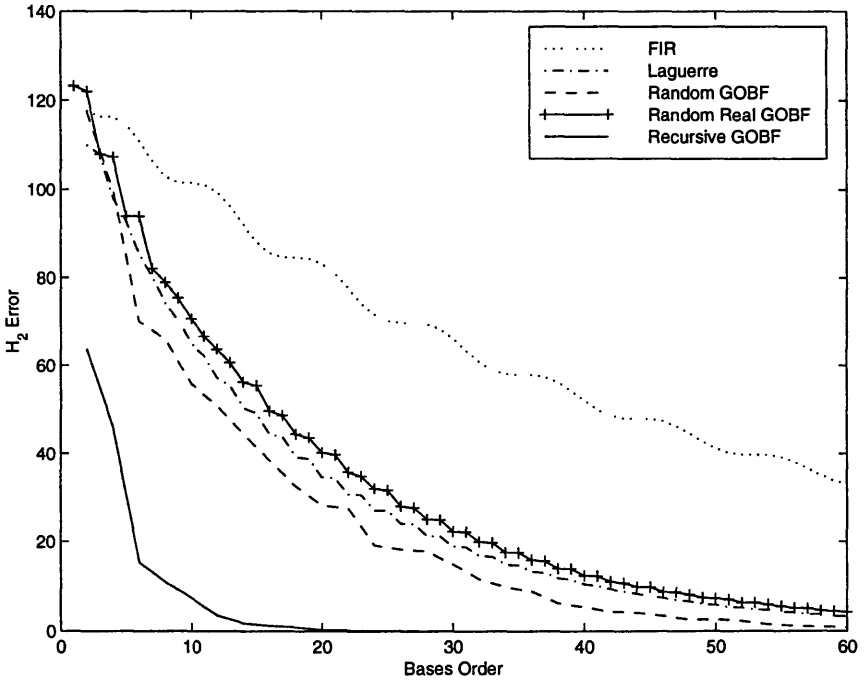

Figure 4.8: Illustration of the $\mathcal{H}_2$ error vs. basis order with FIR, Laguerre, Random Real and Complex GOBF, and Recursive GOBF approximations of $H(z)$.

4.5.2 Frequency-Domain System Identification

System identification from frequency data is easily formulated as a least squares problem. Consider approximating the frequency response $G(\omega)$ using the GOBF, or

$$\min_{\phi} \|W(\omega)(G(\omega) - F(\omega)\phi)\|_2^2 \text{ for all } \omega \in \{e^{i\tilde{\omega}T} | \tilde{\omega} = [0, \pi/T]\}$$

where $W(\omega)$ is a frequency weight and $F(\omega)$ is the vector of basis functions defined in Section 4.5.1. This problem is approximated by minimizing

$$E = \frac{T}{\pi} \sum_{i=1}^{N_\omega} (G(\omega_i) - F(\omega_i)\phi)^* W^T(\omega_i) W(\omega_i)(G(\omega_i) - F(\omega_i)\phi)\Delta\tilde{\omega}_i,$$

or equivalently,

$$E = (G(\omega) - F(\omega)\phi)^* W^T \Delta\Omega W(G(\omega) - F(\omega)\phi),$$

where $W = \text{diag}[W(\omega)]$, $G \in C^{N_\omega \times 1}$, $F \in C^{N_\omega \times N}$, $\phi \in R^{N \times 1}$, $\tilde{\omega}_i$ are a discrete set of sampled frequency points, and $\Delta\Omega$ is defined by,

$$\Delta\Omega = \frac{T}{\pi} \text{diag}[\, \Delta\tilde{\omega}_1 \quad \Delta\tilde{\omega}_2 \quad \cdots \quad \Delta\tilde{\omega}_{N_w} \,],$$

where $\Delta\tilde{\omega}_i = \tilde{\omega}_{i+1} - \tilde{\omega}_i$ for $i = 1, \ldots, N_w - 1$ and $\Delta\tilde{\omega}_{N_w} = \Delta\tilde{\omega}_{N_w - 1}$. To guarantee a real solution, the real and imaginary parts of the G and F matrices are separated, and the least-squares problem is solved by,

$$\phi_{\text{opt}} = (\tilde{F}^T \tilde{W}^T \Delta\tilde{\Omega} \tilde{W} \tilde{F})^{-1} \tilde{F}^T \tilde{W}^T \Delta\tilde{\Omega} \tilde{W} \tilde{G}$$

where $\tilde{F} = [\, F_{Re}(\omega) \quad F_{Im}(\omega) \,]^T$, $\tilde{G} = [\, G_{Re}(\omega) \quad G_{Im}(\omega) \,]^T$, $\Delta\tilde{\Omega} = \text{diag}[\, \Delta\Omega \quad \Delta\Omega \,]$ and $\tilde{W} = \text{diag}[\, W \quad W \,]$. If the basis functions are orthonormal and $\tilde{W} = I$, then the optimal solution is,

$$\phi_{\text{opt}} = \tilde{F}^T \Delta\tilde{\Omega} \tilde{G}.$$

Active Vibration Isolation System System Identification Example

To demonstrate this system identification technique on real frequency data, the Active Vibration Isolation System (AVIS) is used as an example. This system is presented

as a design example in Chapter 7. A detailed description of the AVIS system and data are provided in [29]. The objective of this exercise is to demonstrate how frequency weights with the GOBF can be a used to effectively capture local dynamics in frequency bands of interest, while intentionally under-modeling other frequency bands. Figure 4.9 shows the target Frequency Response Function (FRF) data spanning a frequency range between 0.1 Hz and 5 kHz and exhibiting hundreds of lightly damped modes. The objective is to model the local dynamics in the 400-1500 Hz range while approximating the gain and phase trends outside this range. This type of model would be useful for designing a low order model-based controller with an anticipated crossover frequency between 400 and 1500 Hz.

The fixed pole locations used in the GOBF consisted of placing a second order mode at 35.803 Hz and 0.1791 damping to approximate the lightly damped dynamics in the 10-100 Hz range and then randomly selecting 20 second order modes between 400-700 Hz and 13 second order modes between 700-2500 Hz. Figure 4.9 shows the unweighted 68 order approximation using the GOBF. The approximation failed to approximate the low frequency zero between 0.7 and 0.8 Hz causing a large low frequency gain error and substantial broad band phase error. At low frequency the target transfer function has approximately 50 dB less gain than at high frequencies which essentially reduces the incentive for the least squares solution to eliminate low frequency approximation error. One way to remedy this is to incorporate frequency weights into the least squares problem. In this example the frequency weight was constructed by first inverting the magnitude data to normalize the data to 0 dB through the entire frequency range, then multiplying specified frequency bands by scalar weights listed in Table 4.5.2. Figure 4.10 compares the weighted and unweighted systems. Using the same pole locations, Figure 4.11 shows the 68 order weighted approximation with the GOBF. Now good qualitative matching is observed in the low frequency band while tighter matching is observed in the 400 to 1500 Hz band.

Table 4.3: AVIS frequency weights after normalization.

Frequency Band [Hz]	Weight	[dB]
0.1-10	100	40
100-400	300	49.54
400-1500	1000	60
1500-2000	100	40
2000-5000	10	20

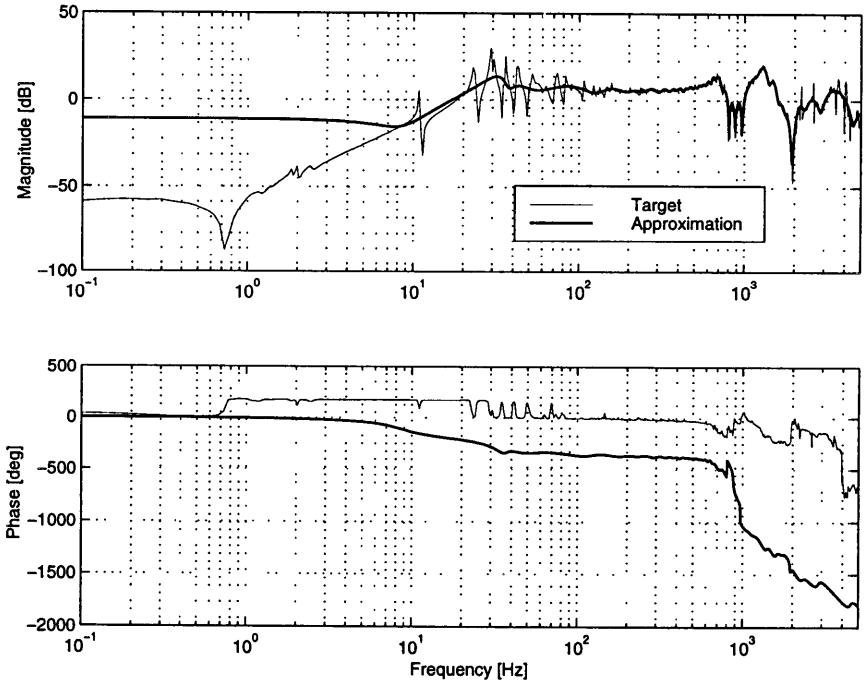

Figure 4.9: AVIS system identification example with GOBF.

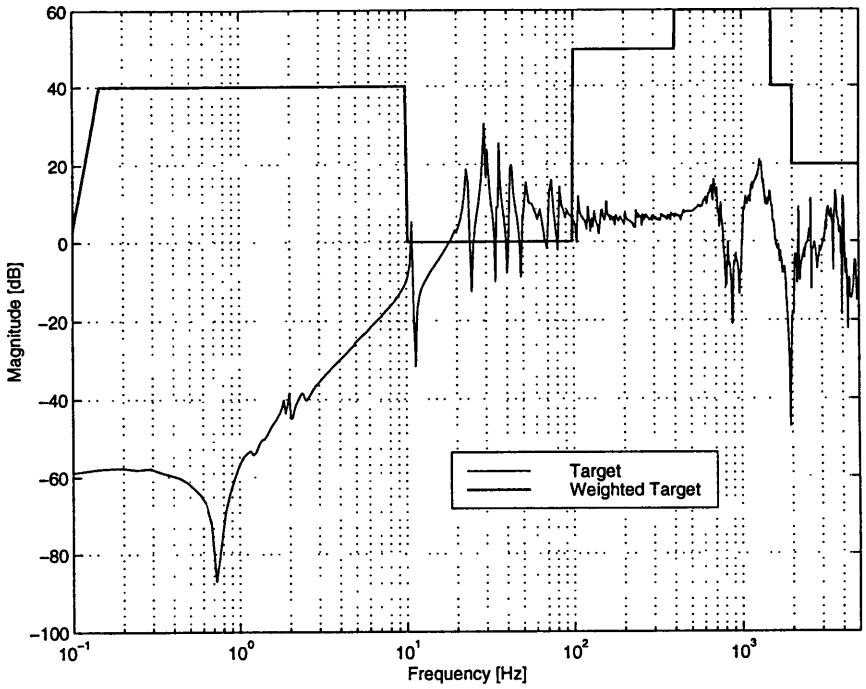

Figure 4.10: AVIS FRF magnitude and weighted magnitude.

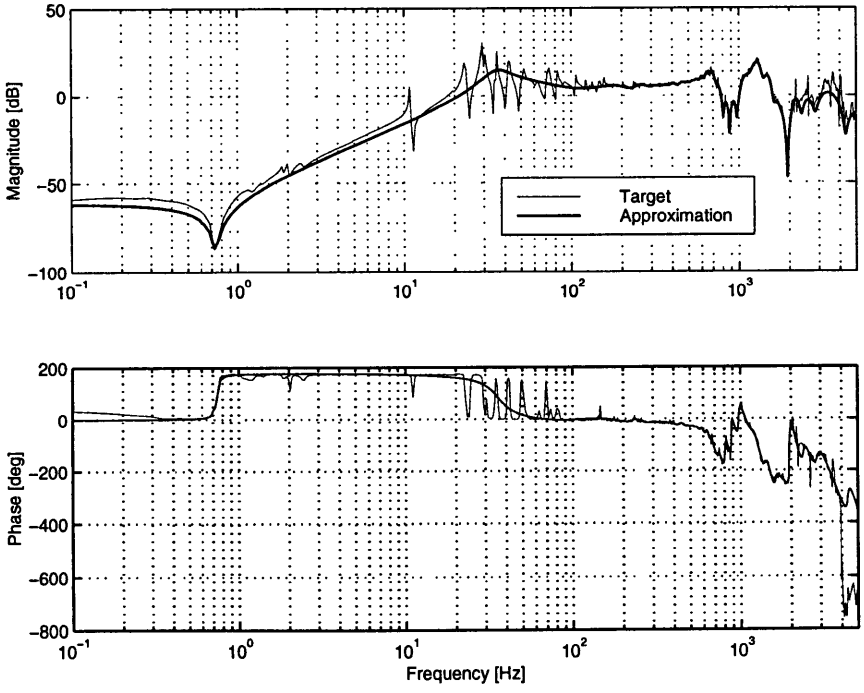

Figure 4.11: AVIS system identification example with weighted GOBF.

Chapter 5

Graphical User Interface Tool

A MATLAB based Computer-Aided Design (CAD) tool known as the Structural Control Toolbox (SCTB) [32] was developed under subcontract at The Charles Stark Draper Laboratory to include the constrained $\mathcal{H}_2$ methodology. The SCTB tools are driven in a Graphical User Interface (GUI) environment that eliminates the need for the user to interact with the MATLAB command line. The present capabilities of the SCTB include:

- Plant construction from linear models or Frequency Response Function (FRF) data.
- Controller design via classical, model based $\mathcal{H}_2$, $\mathcal{H}_\infty$, μ, or constrained optimization design methods.
- Plant and controller model reduction.
- Real-time controller interface.

This chapter introduces the GUI panels associated with designing constrained $\mathcal{H}_2$ controllers only. More detail on the other SCTB features can be found in the **Structural Control Toolbox; User's Guide** [32].

5.1 Main Panel

Upon launching the SCTB from the MATLAB command line, the main panel appears as shown in Figure 5.1. The main panel has a menu bar with four pull-down menus: File, Window, Options, and Help; text fields for the system name and description; plant and controller list boxes which contain variations of the design model and controller design iterations; and various buttons and pop-up menus that allow the user to access the SCTB tools. These tools allow the user to import plants and controllers into the SCTB data structures, design controllers, close loops, analyze open-loop and closed-loop systems, and perform model reduction. The remainder of this chapter will focus on the SCTB tools associated with controller design, in particular the constrained $\mathcal{H}_2$ methodology.

5.2 Constrained Optimization Controller Design GUI

The constrained $\mathcal{H}_2$ software is accessed by selecting the "Constrained Optimization" option under the "Design Methods" pop-up menu on the main panel. This launches the constrained optimization controller design GUI as shown in Figure 5.2. The GUI is designed to operate in four modes:

1. Objective function specification mode.
2. Basis function specification mode.
3. frequency-domain constraint specification mode.
4. time-domain constraint specification mode.

The modes are toggled through a set of radio buttons on the left hand side of the panel. The right hand side of the constrained optimization controller design GUI is updated for each mode with custom interfaces to accept the user input. By default, this panel is initially in the objective function specification mode. After the objective,

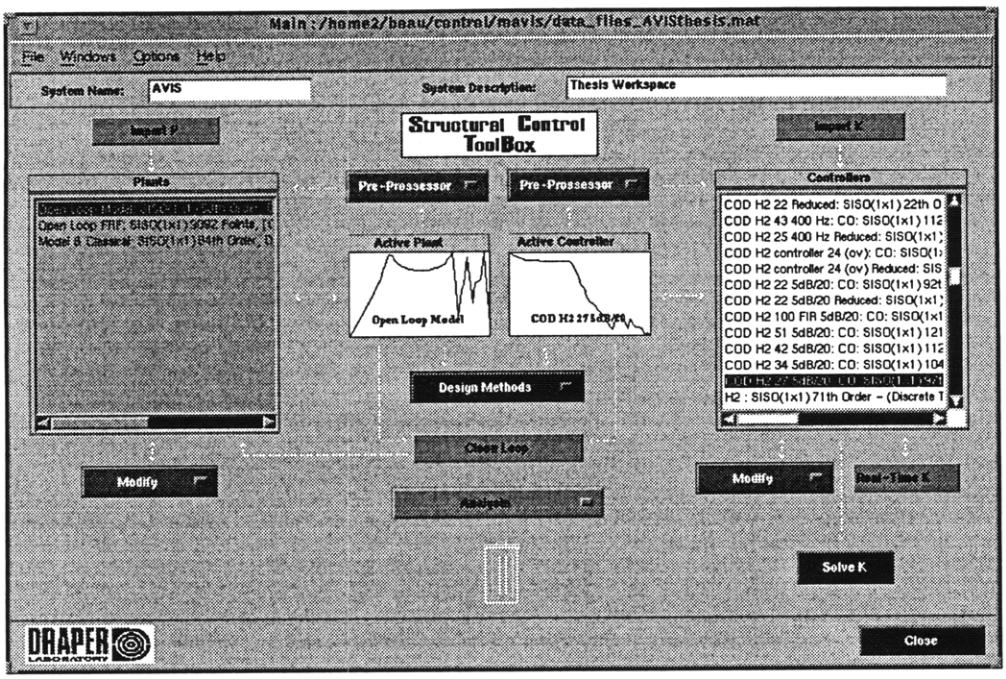

Figure 5.1: Main panel.

basis and constraints have been specified, the problem can be solved by simply clicking the "Solve" button in the lower left corner of the panel.

5.2.1 Objective Function Specification Mode

The objective function specification mode shown in Figure 5.2 is the default setting of the constrained optimization controller design GUI. The $\mathcal{H}_2$ minimization option in optimization method pop-up menu must be selected with the appropriate transfer matrix to engage the constrained $\mathcal{H}_2$ design method. Frequency weights can be appended to the design model by clicking the "Frequency Weights" button and following the instructions. Finally, the feedback sign should be selected appropriately for positive and negative feedback controller design problems.

5.2.2 Basis Function Specification Mode

After the objective function has been specified, a basis for Q must be selected. Clicking the "Edit Basis" radio button produces the basis function control panel as shown

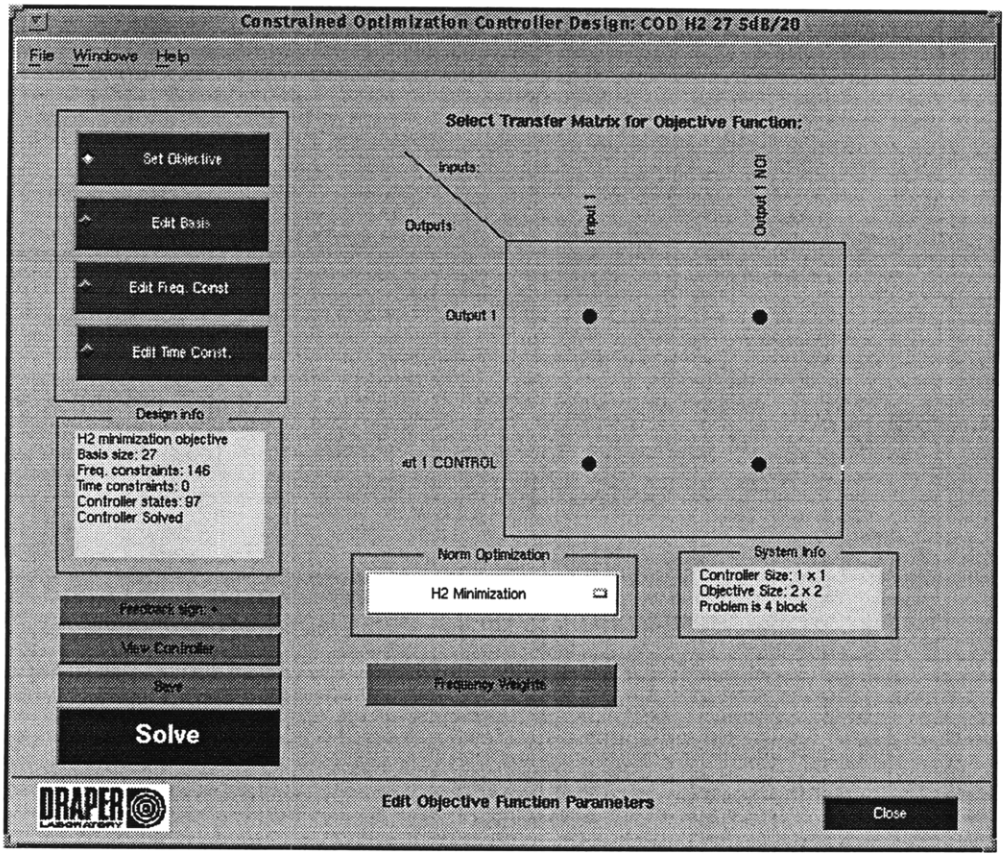

Figure 5.2: Objective function control panel – $\mathcal{H}_2$ minimization.

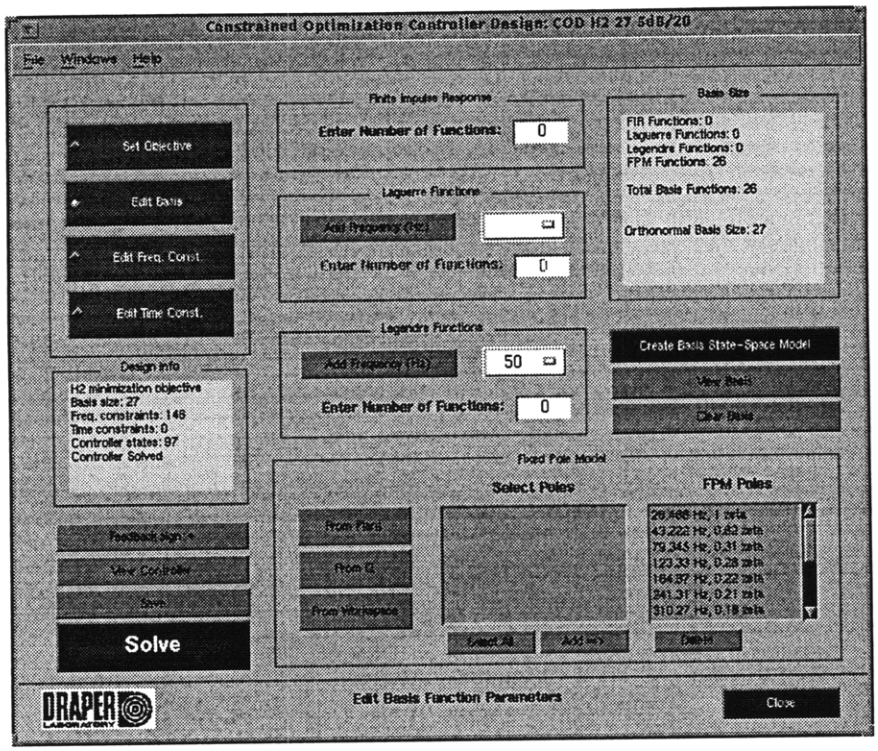

Figure 5.3: Basis function control panel.

in Figure 5.3. This panel has an assortment of basis function generation options for the FIR, Laguerre, Legendre, and the fixed pole models described in [45]. Although the interface remains unchanged, the fixed pole models have been replaced with the GOBF models of Chapter 4 for this work. The user can specify a basis as a mixture of FIR, Laguerre, Legendre, and GOBF models. The state-space realization of the orthonormal basis is generated by clicking the "Create Basis State-Space Model" button on the right hand side of the panel.

5.2.3 Frequency-Domain Constraint Specification Mode

The frequency and time-domain constraints are specified by clicking the appropriate radio buttons on the on the left hand side of the the constrained optimization controller design GUI. Clicking the "Edit Freq. Const." button produces the frequency domain constraint function selection panel as shown in Figure 5.4. This panel displays a matrix of transfer functions which can be constrained. A transfer function is

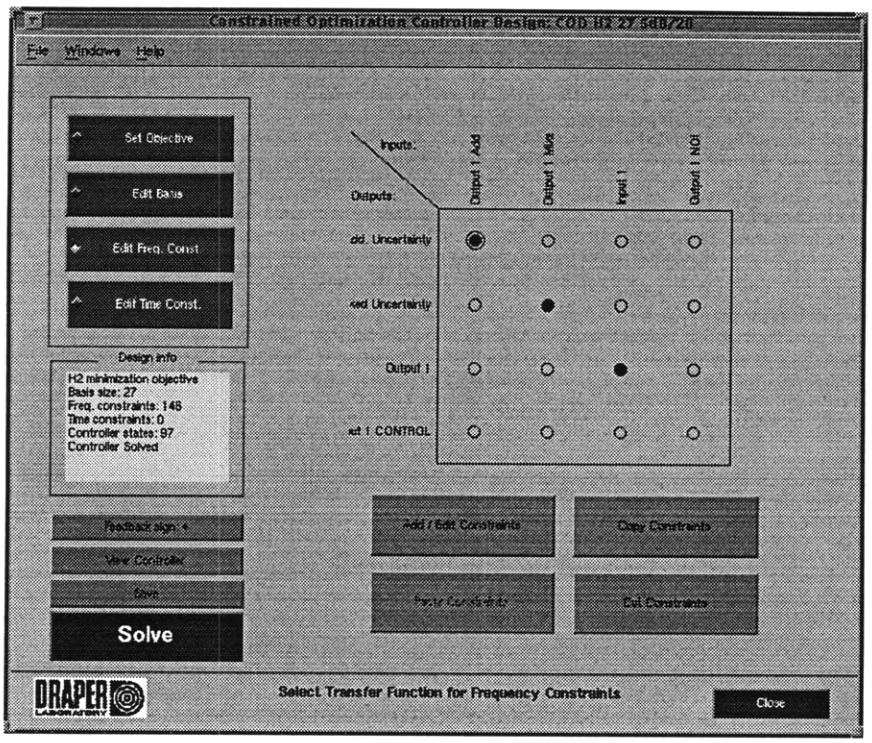

Figure 5.4: Frequency-domain constraint transfer function selection panel.

selected by clicking on the circle corresponding to that particular transfer function in the matrix. Constraints are added or edited to the selected transfer function by clicking the "Add/Edit Constraints" button. This produces the frequency-domain constraint tool shown in Figure 5.5. Constraints can be added at single points by pressing the "Add Points" radio button and clicking on the appropriate spot on the Bode magnitude plot. Likewise, a line of discrete frequency constraint points can be added by first pressing the "Add Lines" radio button, entering a line density of points per decade, and clicking on the Bode magnitude plot to specify the initial and final points of the line segment. Each point constraint is approximated with N linear constraints as discussed in Section 2.3.2. The number of linear constraints per frequency-domain constraint is specified in the "Angles per Constraint" field. The open-loop and previous closed-loop transfer functions can be plotted as a reference as shown in Figure 5.5. Constraints can be deleted using the "Delete" button and specific areas of the Bode magnitude plot can be enlarged or reduced using the "Zoom" feature.

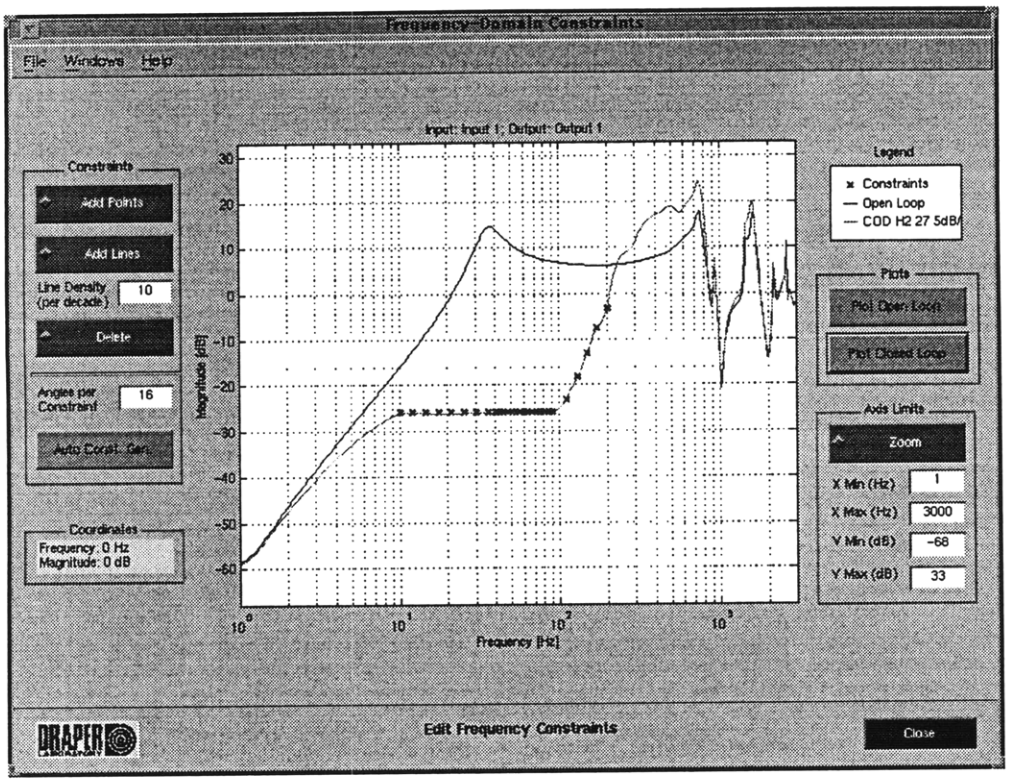

Figure 5.5: Frequency-domain constraint tool.

Automatic Constraint Generator

Some of the most common constraints can be generated automatically through the automatic constraint generator shown in Figure 5.6. The automatic constraint generator is accessed by pressing the "Auto Const. Gen." button on the frequency-domain constraint tool. The user must select the form of closed-loop transfer function currently being constrained on the left hand side of the GUI. The choices $K/(1+PK)$, $PK/(1+PK)$, $1/(1+PK)$, and $(1-PK)/(1+PK)$ correspond to the transfer functions seen by the additive, multiplicative, divisive, or mixed multiplicative/divisive uncertainties respectively. After the appropriate closed-loop transfer function has been selected, the user must select either the compensator roll-off, loop gain roll-off, or gain and phase margin constraints option on the right hand side of the GUI. For example, selecting the "Additive – $K(1+PK)$" and "Compensator Roll Off" radio buttons produces the roll-off constraint tool shown in Figure 5.7. The user must specify the roll-off slope (in dB/decade), approximate crossover, minimum and max-

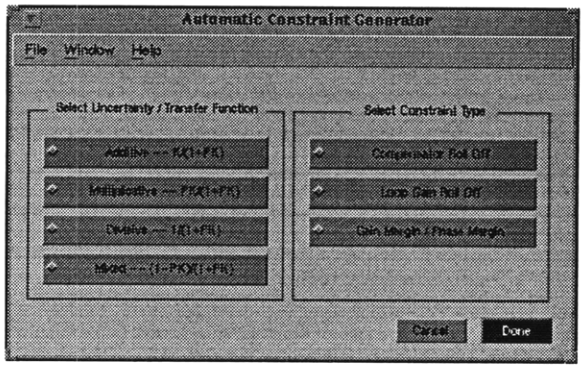

Figure 5.6: Automatic constraint generator.

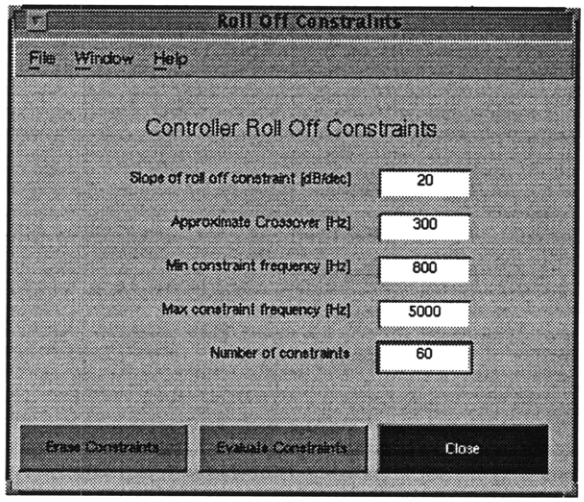

Figure 5.7: Roll-off constraint tool.

imum constraint frequency, and the total number of constraints. The constraints are automatically placed on the Bode magnitude plot when the "Evaluate Constraints" button is pressed.

Gain and phase margin constraints can be automatically generated for the multiplicative, divisive, or mixed uncertainty models by selecting the appropriate transfer function and pressing the "Gain Margin / Phase Margin" radio button. This produces the gain and phase margin constraint tool shown in Figure 5.8. The user supplies the desired gain and phase margins, approximate gain and phase margin frequencies, and the total number of constraints. The region of allowable simultaneous gain and phase perturbations at each crossover frequency are plotted on the left hand side of the tool as discussed in Section 3.5. The constraints are automatically placed on the

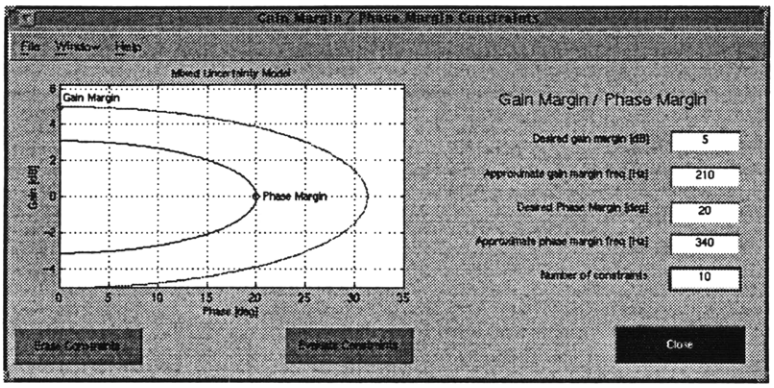

Figure 5.8: Gain and phase margin constraint tool.

Bode magnitude plot when the "Evaluate Constraints" button is pressed.

5.2.4 Time-Domain Constraint Specification Mode

The time-domain constraints mode is activated by clicking the "Edit Time Const." button on the constrained optimization controller design GUI. The time-domain constraint tool operates in two modes: the disturbance specification mode and the constraint specification mode. The disturbance specification mode shown in Figure 5.9 allows the user to define a specific disturbance profile using the mouse to shape the profile or choose from a list of typical disturbances such as an impulse, step, or ramp. After the disturbance profile has been specified, the transient response to the disturbance can be constrained in the constraint specification mode as shown in Figure 5.10. The open-loop response and previous closed-loop responses can be plotted for reference before the constraints are added. The user can toggle between placing upper and lower bound constraints by selecting the appropriate mode of the pop-up menu in the lower left hand corner of the panel. Constraints can be added at single points with the mouse or along a line segment by specifying the line density and end points of the segment. Constraints can be deleted using the "Delete" button and specific areas of the figure can be enlarged or reduced using the "Zoom" feature.

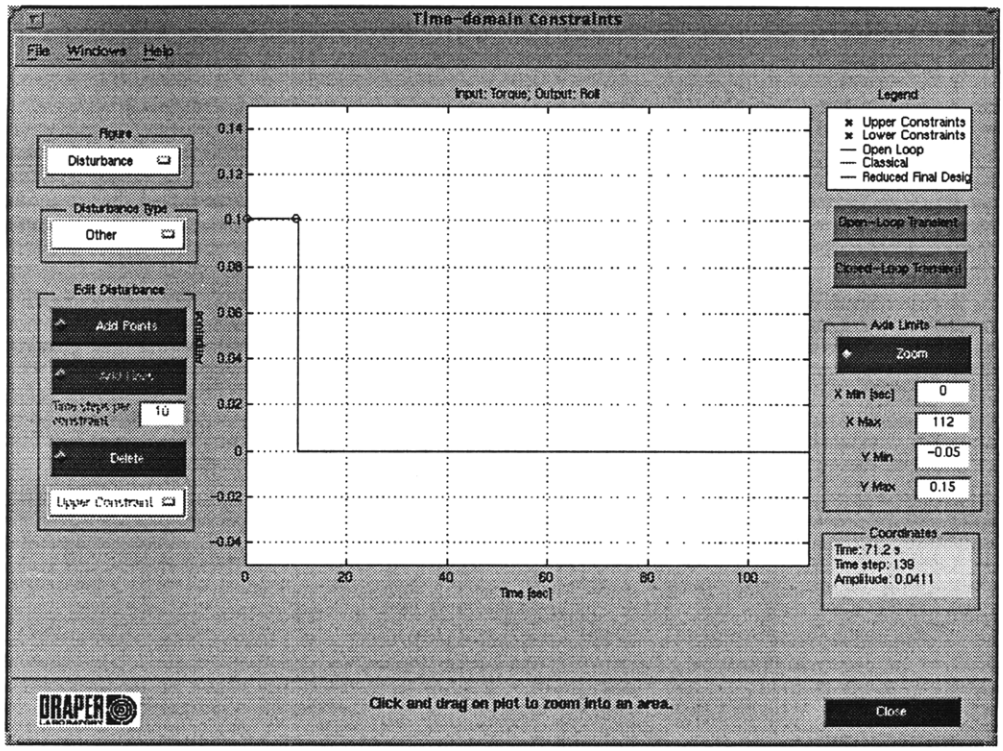

Figure 5.9: Time-domain constraint tool – Disturbance specification.

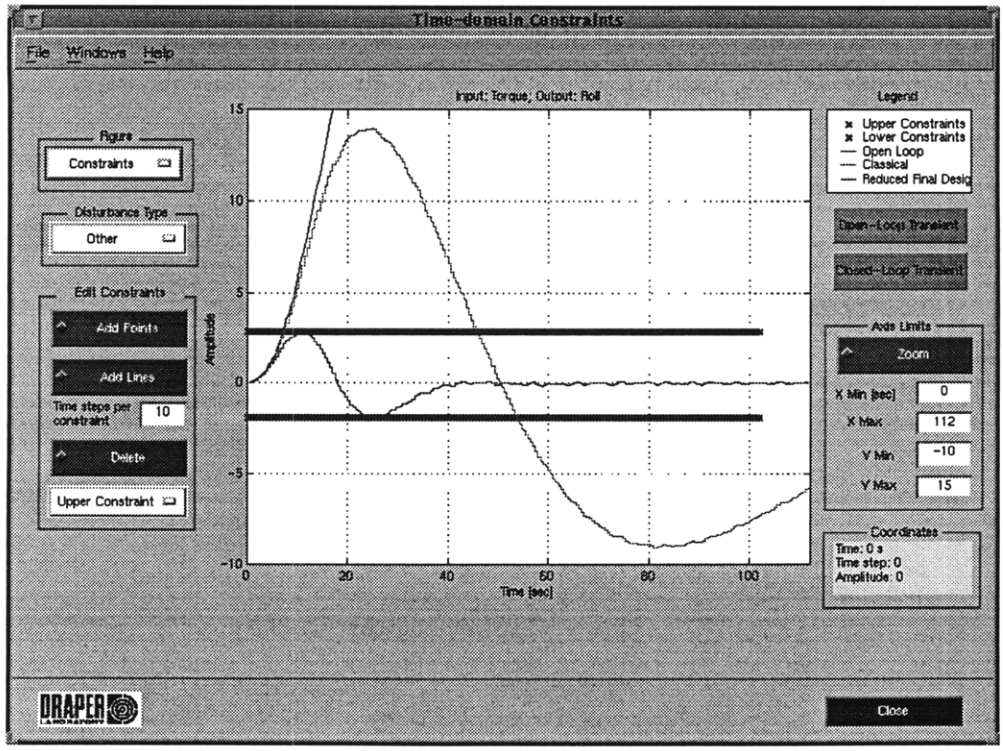

Figure 5.10: Time-domain constraint tool – Constraint specification.

Chapter 6

EOS-AM1 Precision Pointing Attitude Control Example

The Earth Observing System (EOS)-AM1 spacecraft, shown in Figure 6.1, is a three axis stabilized satellite with a large lightweight gallium arsenide solar array extending along the pitch axis. The attitude control system has specific peak-to-peak angular excursion pointing requirements during the normal (science data taking) mode [1]. However, the presence of lightly-damped solar array structural modes (and frequency uncertainty) has limited the bandwidth of the classical control system [39].

To investigate the potential for improved pointing performance in the presence of low frequency solar array modes, NASA Goddard Space Flight Center funded a study to examine the application of robust control [1]. Since the time of that study the EOS-AM1 spacecraft model has been used at the Draper Laboratory as a benchmark problem to evaluate and develop new design techniques.

The following design focuses on a $\mathcal{H}_2$ design with performance and stability robustness constraints for the roll axis. Previous multi-axis designs [1] show that the controllers can safely be designed on a per axis basis, due to the low cross-axis coupling.

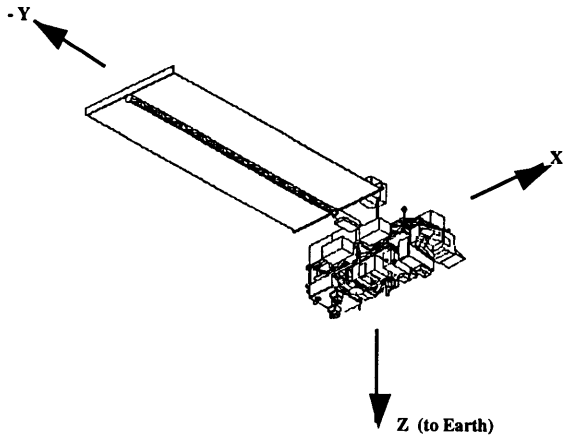

Figure 6.1: EOS-AM1 Spacecraft.

6.1 Classical Design

The classical design described in [39] is used as a baseline to formulate the design objectives presented in this chapter. The original design goals for the classical system were "to provide the necessary low frequency disturbance torque rejection while maintaining 10 dB of gain margin and 40 degrees of phase margin." These margins are more conservative than the design objectives presented in Section 6.2 and limit the peak-to-peak performance.

The philosophy of the classical design was to achieve the desired gain and phase margins by choosing the system bandwidth to be at least 10 times lower than the dominate resonant frequency. The design used a proportional-integral architecture to sequentially close the minor rate and major position loops respectively. Third order low-pass (Butterworth) filters were placed in the rate and position feedback loops to provide attenuation at frequencies above the system bandwidth. An notch filter was included to provide additional attenuation at the dominant flexible body modal frequencies.

6.2 Design Objectives

In the NASA study, a simplified model of the EOS-AM1 dynamics was used along with the four control design objectives listed below. These design objectives seek to improve the peak-to-peak transient response of the classical design while maintaining a minimal level of stability robustness. Several controllers were designed at Draper Laboratory and MIT which attempted to meet all four of these specifications [1, 17]. For comparison, the results from some of the Draper designs are shown in Tables 6.2 and 6.3. The control design objectives are:

1. Reject sinusoidal disturbances at the 0.00015 Hz orbital rate below the magnitude of the baseline controller performance at 9 dB [asec/in-lb].
2. Improve the peak-to-peak transient response to a 10 second, 0.1 in-lb torque pulse by a factor of 5 over baseline (from 24 to 4.82 arcsec).
3. Provide 3 dB gain margin and 30° phase margin.
4. Guarantee robust stability with 15% flexible modal frequency uncertainty.

6.3 Design Model

The continuous-time design model included a combination of the roll axis rigid body modes and three dominant flexible modes of the solar array, and has the form:

$$P(s) = \left(\frac{1}{Js^2} + \sum_{k=1}^{3} \frac{\theta_k^2}{s^2 + \zeta\omega_k s + \omega_k^2} \right) \text{[arc-sec/in-lbs]}$$

with

$$\begin{aligned} J^{-1} &= 1.2917, \zeta = 0.0015, \\ \theta^2 &= [0.8226 \quad 1.2719 \quad 0.4380], \\ \omega &= [0.2219 \quad 0.3469 \quad 0.4527] \times 2\pi. \end{aligned}$$

For design, the plant was converted to a discrete time representation using a zero order hold with a sampling time of 0.512 sec. A single cycle time delay z^{-1} was then

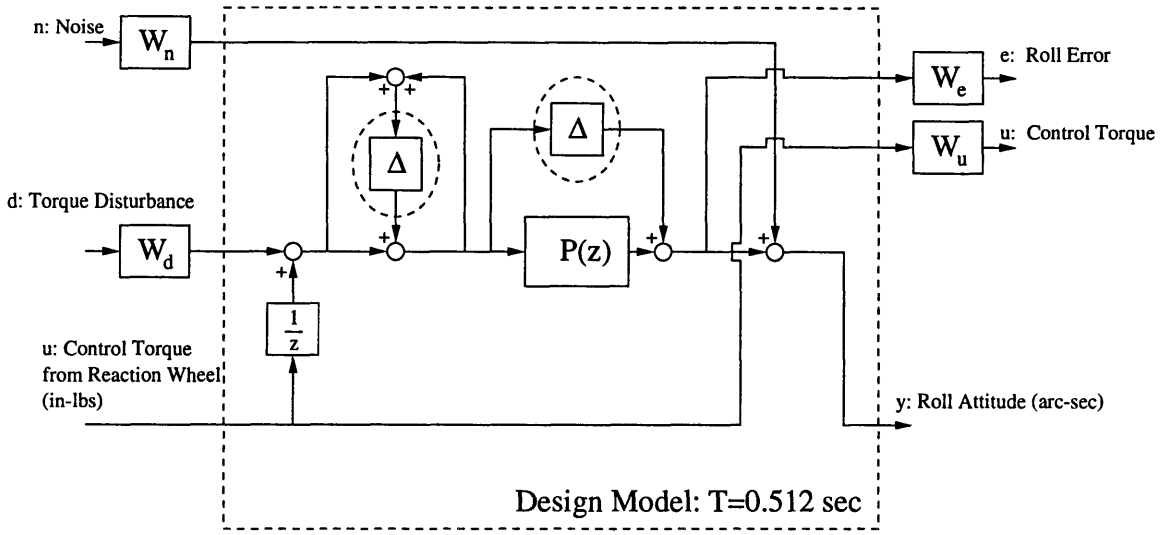

Figure 6.2: EOS-AM1 Design Model.

appended to the input to model a processing delay present in the control computer, resulting in a 9th order discrete model shown in Figure 6.2. The input of this model is a control torque from reaction wheel actuators in in-lbs, and the output is the roll attitude of the spacecraft, measured in arc-sec.

To pose the problem in standard LQG form, the plant roll output and the control signal were selected as the regulated output. A disturbance was added to the control signal at the plant input, and an exogenous noise input was added to the attitude measurement.

Butterworth filter weighting functions were appended to the regulated outputs to penalize the error at low frequencies and control effort at high frequencies. Scalar weights on the roll error, control, disturbance, and noise were adjusted until the unconstrained $\mathcal{H}_2$ design came close to meeting the design objectives. The optimization weights are listed below.

- Roll error: 2nd order, 0.18 Hz, low-pass filter (W_e).
- Control: 3rd order, 0.30 Hz, 60 dB high-pass filter (W_u).
- Disturbance: -6.02 dB (W_d).
- Noise:-20 dB (W_n).

Two types of modeling uncertainty were included as a mechanism to meet the robustness objectives. An additive uncertainty $P + \Delta_a$ was included to add high frequency robust stability constraints, and a mixed multiplicative and divisive uncertainty at the plant input $(1 + \Delta_m)(1 - \Delta_m)^{-1}P$ was included to constrain the gain and phase margins. The outputs and inputs from these Δ blocks appear as extra inputs and outputs in the design model.

6.4 Constrained $\mathcal{H}_2$ Design

The design objectives were directly addressed by simultaneously placing constraints on the appropriate transfer functions and transient responses. The first performance requirement was to achieve the same level of disturbance rejection at the orbital rate (0.00015 Hz) as the classical controller. This was met by placing a single constraint in the frequency domain on the transfer function from the torque disturbance to the roll error or $P/(1 - PK)$, with the magnitude constrained to be less than 9 dB at 0.00015 Hz. This constraint, and the resulting closed loop is shown on Figure 6.3. Also shown on this figure are the open loop, classical closed loop, and the unconstrained $\mathcal{H}_2$-optimal solution.

The second performance requirement was to improve the peak-to-peak transient response of the classical closed loop by a factor of five to a 10 second 0.1 in-lb torque disturbance pulse. This was achieved by placing time-domain constraints on the transient response, shown in Figure 6.4. This figure also shows the unconstrained $\mathcal{H}_2$ solution and the classical transient response for comparison.

The gain and phase margin constraints discussed in Section 3.5 are used to meet the third design objective by placing a mixed multiplicative and divisive uncertainty block at the plant input. The uncertainty has the form

$$P = P_{nom}\left(\frac{1 + \Delta_m}{1 - \Delta_m}\right).$$

By the small gain theorem, stability is guaranteed if $|\Delta_m(\omega)| \leq r(\omega)$ and

$$\left|\left(\frac{1 + PK}{1 - PK}\right)(\omega)\right| < \frac{1}{r(\omega)} \qquad \forall\omega.$$

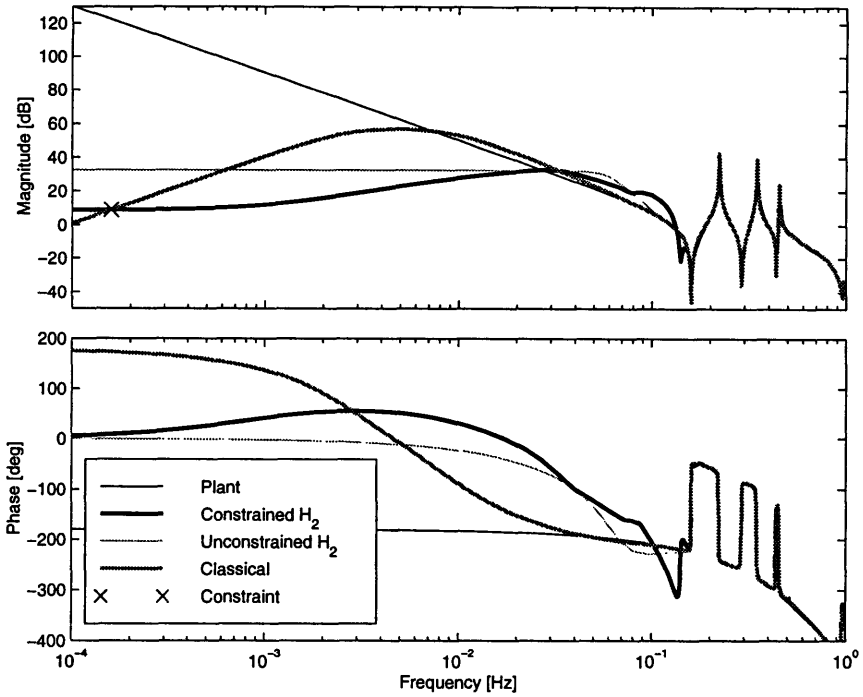

Figure 6.3: Orbital rate disturbance rejection constraint.

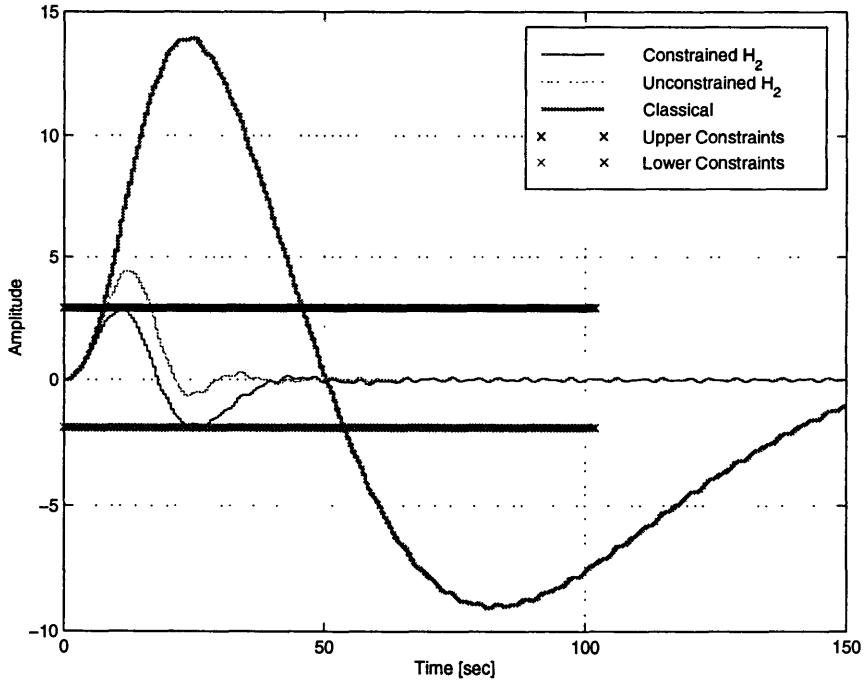

Figure 6.4: Closed-loop transient response constraints.

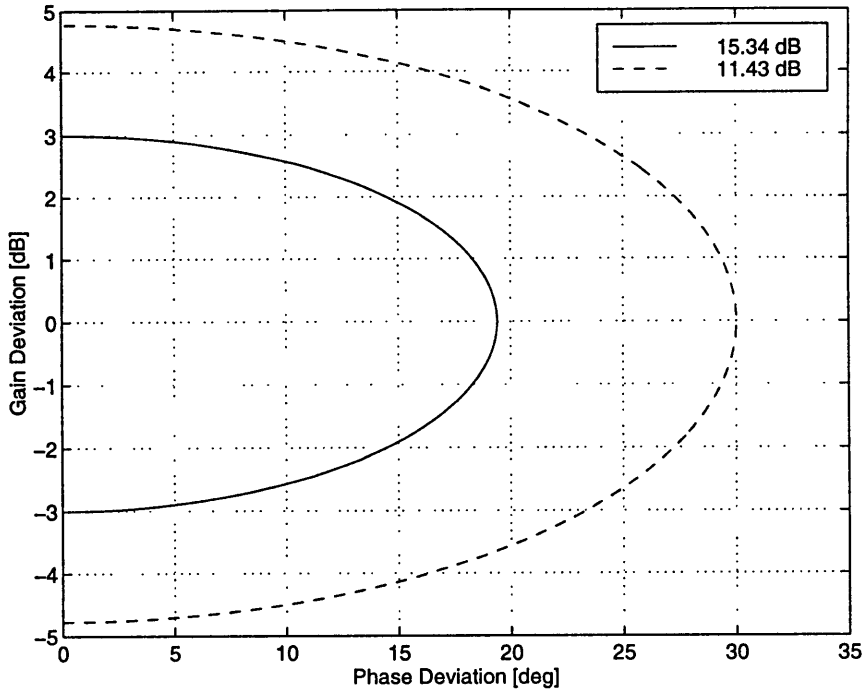

Figure 6.5: Guaranteed gain and phase margins for bound on $|(1+PK)/(1-PK)(\omega)|$.

Therefore, stability is guaranteed for any perturbation in the loop gain which falls inside the complex-plane circle $(1 + re^{j\theta})/(1 - re^{j\theta})$ where $\theta \in [0, 2\pi]$. Figure 6.5 shows two of these circles, and their corresponding bounds on the magnitude of $(1 + PK)/(1 - PK)$. This figure tells us that in order to guarantee ± 3 dB gain margin and 30° phase margin, $|(1+PK)/(1-PK)(\omega)|$ must be constrained below 15.34 dB at phase crossover and 11.43 dB at magnitude crossover. Figure 6.6 shows the constraints on $(1 + PK)/(1 - PK)$ which were distributed around the region of anticipated phase and gain cross-over. The actual gain and phase cross-over with the final design was found to be 0.05 Hz and 0.1 Hz respectively.

The fourth and final specification was to guarantee robust stability for 15% modal frequency uncertainty. An additive uncertainty model is used to model the frequency uncertainty:

$$P = P_{\text{nom}} + \Delta_a.$$

To bound the magnitude of the Δ_a block, define the set of all possible modal frequen-

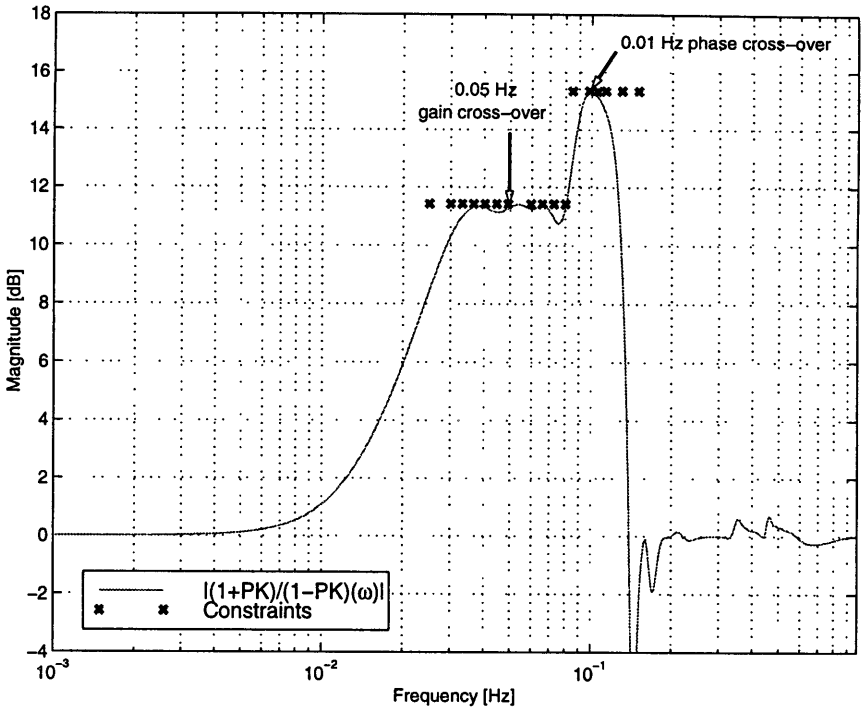

Figure 6.6: Gain and phase margin constraints.

cies to be

$$\Omega = \{\bar{f} : \bar{f} \in [0.85\bar{f}_{\text{nom}}, 1.15\bar{f}_{\text{nom}}]\}$$

where $\bar{f} \equiv [f_1, f_2, f_3]$ is a vector of the three modal frequencies, and $\bar{f}_{\text{nom}}$ is the nominal value of these three frequencies. The frequency response of P is then a function of $\bar{f}$, and the perturbation is constructed as

$$\delta(\omega, \bar{f}) = P(\omega, \bar{f}) - P(\omega, \bar{f}_{\text{nom}})$$

The magnitude of Δ_a is bounded by

$$|\Delta_a(\omega)| \leq |\Delta_{\text{sup}}(\omega)| = \sup_{\bar{f}\in\Omega} |\delta(\omega, \bar{f})|.$$

By the small gain theorem, stability is guaranteed if

$$\left|\left(\frac{K}{1-PK}\right)(\omega)\right| < \left|\frac{1}{\Delta_{\text{sup}}(\omega)}\right| \qquad \forall\omega.$$

Figure 6.7 shows the application of these robustness constraints. The grey area is $|\Delta_{\text{sup}}^{-1}|$, calculated numerically by varying the three structural modes in the plant by

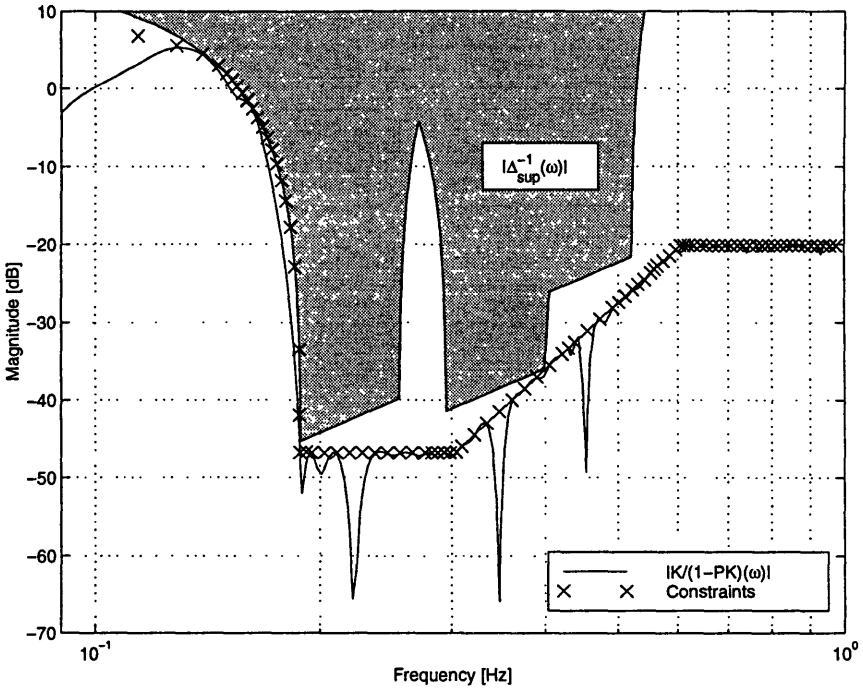

Figure 6.7: Robust stability constraints.

±15%. The constraints were chosen to lie below this area. A smooth shape was chosen for the constraints, giving the closed loop additional conservatism, and simplifying the controller.

6.5 Basis Selection

Three bases for Q were selected for this problem including the FIR, Legendre, and GOBF basis. The figures and results presented in Section 6.4 are based on the Legendre basis solution. The Legendre orthonormal basis was constructed with real poles at frequencies [0.05 0.15 ... $(0.1N$ - 0.05)] Hz shown in Figure 6.8 on the complex plane. This pole location choice bears resemblance to the continuous time Legendre basis functions as described [28]. A total of 80 functions were used for optimization (plus a constant, for a total of 81 basis functions). The quadratic program had 81 variables and 2193 linear constraints. A Sun Sparc 20 found the solution in two minutes using the MINOS optimization software [49]. The full order controller consisted

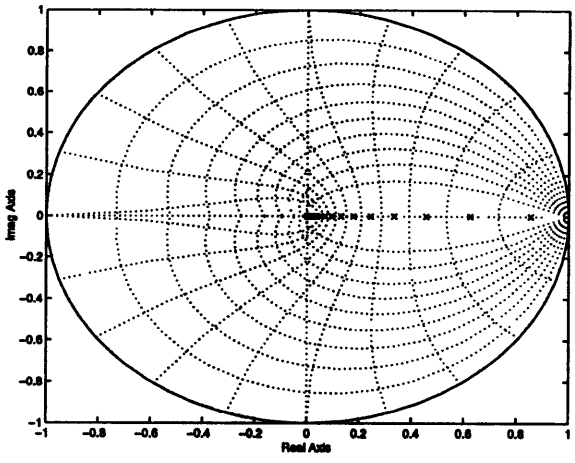

Figure 6.8: Legendre pole locations.

of 104 stable states. A balanced model reduction [48] of the controller decreased the order to 20 states with little degradation in performance or robustness.

For comparison, this problem was resolved using the FIR and GOBF basis. The basis order, controller order, and reduced controller order with corresponding specification error are tabulated for each basis in Table 6.1 and compared to the Legendre basis described above. The specification error is the maximum percent in which the original specifications were violated after model reduction. The basis order column lists the minimum number of FIR and GOBF basis functions[1] needed to find a feasible solution which meets all of the design specifications. A balanced model reduction was used to find reduced order controllers with minimal degradation in performance. The minimum number of FIR basis functions needed to obtain a feasible solution was found to be 85 compared to 30 GOBF. Figure 6.9 and 6.10 show that the majority of the GOBF poles are lightly damped and distributed over a wide frequency band while all of the FIR poles are at the origin. The GOBF pole locations were found through a recursive process discussed in Section 4.4 that starts with the Legendre or FIR pole locations, solves the optimization problem, and sets the new pole locations to the poles of a reduced order Q plus some additional Legendre or FIR poles.

[1]Plus a constant

Table 6.1: Basis Comparison.

Basis	Basis Order	Controller Order		Specification error with
		Full	Reduced	reduced controller [%]
FIR	85	108	22	1.14
Legendre	81	104	20	0.73
GOBF	30	53	18	0.42

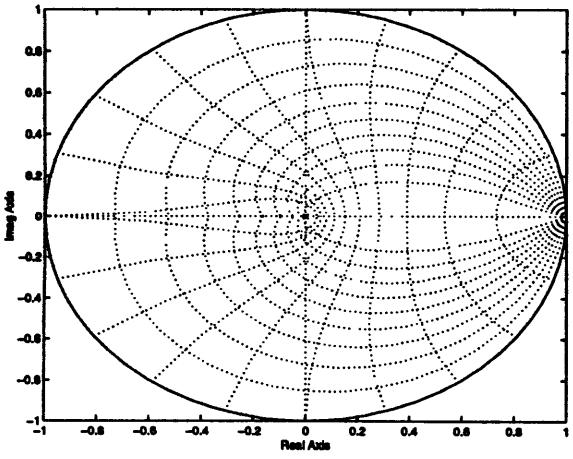

Figure 6.9: FIR pole locations.

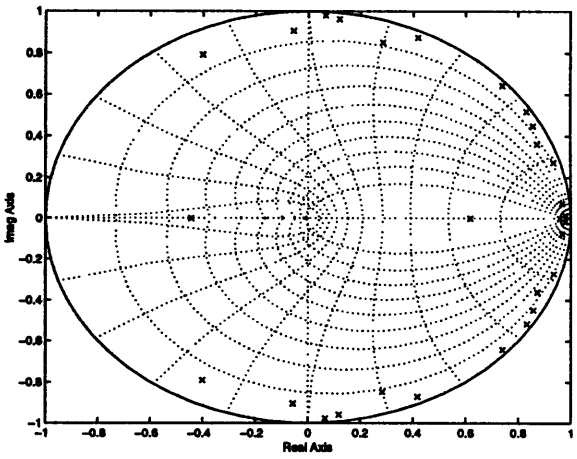

Figure 6.10: GOBF pole locations.

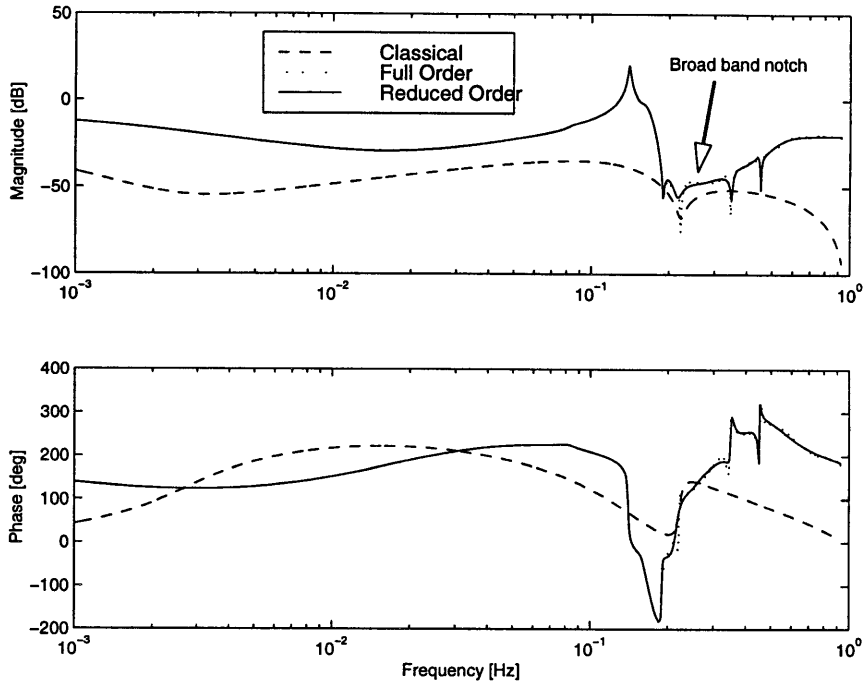

Figure 6.11: EOS-AM1 full and reduced order Legendre compensators compared to the classical design.

6.6 Compensator and Results

The full and reduced order Legendre compensators are shown in Figure 6.11 compared to the classical design. Qualitatively, the constrained $\mathcal{H}_2$ design is a higher gain controller than the classical with a broad notch between 0.2 and 0.6 Hz which gain stabilizes the flexible body modes. This is illustrated on the Nichols chart in Figure 6.12 and 6.13 where the circling motion of the loop transfer function corresponding to the flexible body modes stays below 0 dB.

Tables 6.2 and 6.3 compare the constrained $\mathcal{H}_2$ design to classical, the unconstrained $\mathcal{H}_2$, and three previous Draper designs. The requirements are listed at the top of the table and violations are emphasized with italics. The Constrained $\mathcal{H}_2$ design, in bold, is the only design that simultaneously meets all of the design specifications.

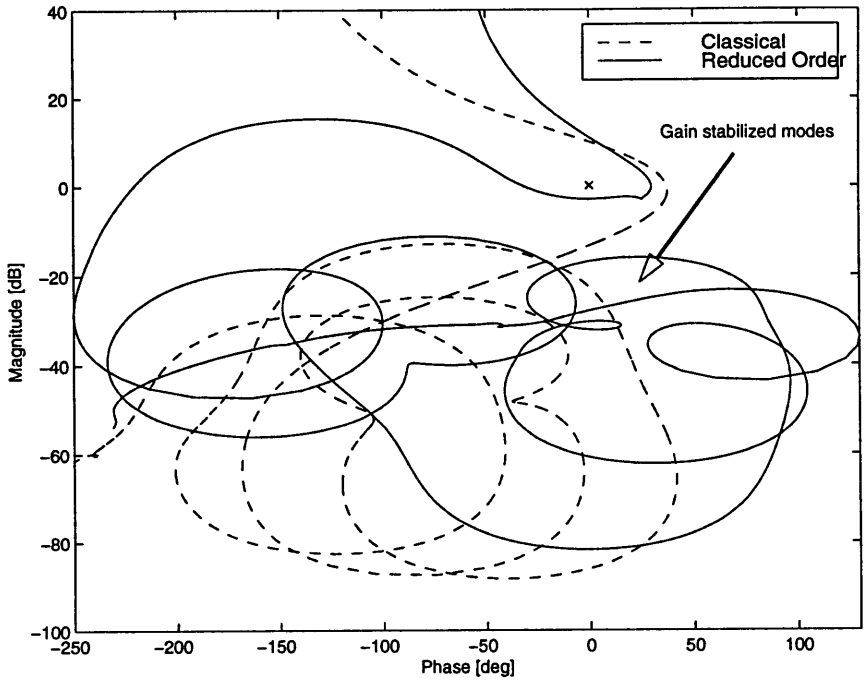

Figure 6.12: Nichols chart of reduced Legendre and classical controllers.

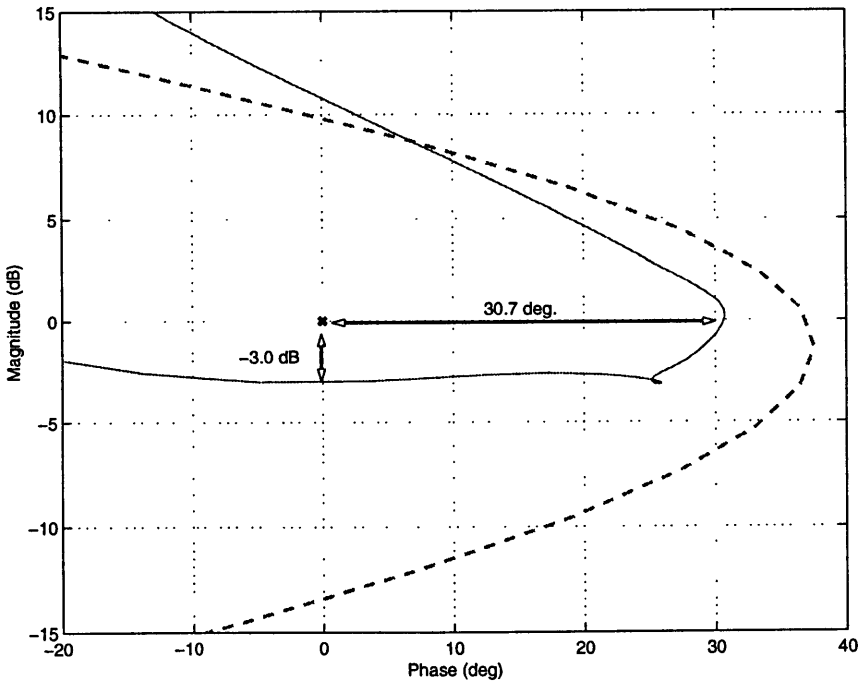

Figure 6.13: Gain and phase margins of reduced Legendre controller.

Table 6.2: Performance Comparison.

Control Method	Disturbance Rejection at Orbital Rate [arcsec/in-lbs]	Peak-to-Peak transient to 10 second 0.1 in-lb torque pulse [arcsec]
Requirement	2.8	4.8
Classical	2.8	*24.1*
$\mathcal{H}_2$	*43.8*	*5.1*
Constrained $\mathcal{H}_2$	**2.8**	**4.8**
Previous Draper Designs		
LQG	0.5	*16.9*
$\mathcal{H}_\infty$	1.6	3.2
μ	2.4	4.6

6.7 Conclusion

The constrained $\mathcal{H}_2$ design approach directly accommodates the precision pointing control objectives listed in Section 6.2. This design is the first successful design of many attempts, including classical and modern approaches, to simultaneously meet all of the design objectives. No attempt was made to exceed the performance and stability robustness objectives described in Section 6.2. Although the constrained $\mathcal{H}_2$ controllers were of order 53 and above, simple model reduction reduced the controller order to as low as 18 states with little degradation in performance and stability robustness.

Table 6.3: Robustness Comparison.

Control Method	Robustness to Modal Frequency Error			Stability Margins	
	Mode 1 [%]	Mode 2 [%]	Mode 3 [%]	Gain margin [dB]	Phase margin [deg]
Requirement	15.00	15.00	15.00	3.00	30.0
Classical	32.50	55.63	68.13	8.52	36.9
$\mathcal{H}_2$	15.60	16.30	62.00	3.60	*22.5*
Constrained $\mathcal{H}_2$	**15.00**	**33.00**	**58.00**	**3.00**	**30.7**
Previous Draper Designs					
LQG	*9.40*	40.60	56.30	3.10	35.6
$\mathcal{H}_\infty$	*8.80*	*14.40*	36.30	*1.20*	*7.3*
μ	17.5	39.40	60.60	4.20	*23.3*

Chapter 7

AVIS Disturbance Rejection Control Example

As part of a spaceborne optical system technology demonstration program, Draper Laboratory, under contract from Eastman Kodak Co., has developed and tested a six-axis, Active Vibration Isolation System (AVIS) on the Structural Test Model (STM) test bed [29] shown in Figure 7.1. The optical system technology selected for this study was a 102" diameter telescope structure which is roughly the size of the Hubble Space Telescope. The AVIS is designed to isolate the telescope from disturbances transmitted through six active struts or main mounts that distort the wavefront and perturb the position of the telescope image on the detector. Detailed descriptions of the STM and the nominal AVIS are found in [29]. A second AVIS design found in [46] was based on a constrained optimization approach proposed in [45] and was successfully implemented and tested on the hardware system. This chapter offers a third design based on the reformulated constrained $\mathcal{H}_2$ approach.

7.1 Design Objectives

The objective of the AVIS is to provide >20 dB attenuation between 10 and 200 Hz while shifting the telescope-on-struts modes from 35-65 Hz to 5-10 Hz and providing reasonable gain and phase margin and compensator roll-off. Single-input/single-

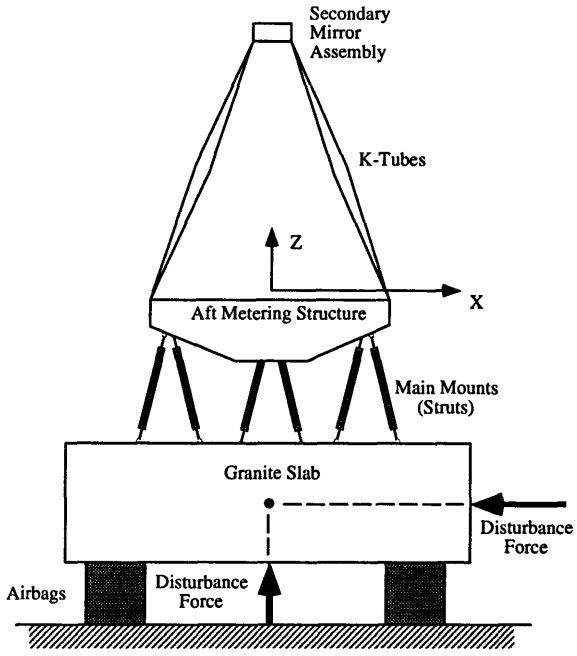

Figure 7.1: Structural Test Model.

output (SISO) classical and reduced constrained optimization [45] AVIS controllers, which neglect coupling between the struts, have been designed, implemented and tested on the STM [29, 46]. The nominal classical controller successfully attenuated the closed loop in the 10-100 Hz range while keeping the primary structural mode above 5 Hz and providing 2 dB and 10 degrees of gain and phase margin respectively. This prompted the following design objectives for the constrained optimization controller [46]:

1. Improve upon the closed-loop classical performance in the 10–200 Hz range.

2. Meet or exceed the gain and phase margins of the classical controller.

3. Keep the primary structural mode above 5 Hz in the closed loop.

4. Maintain stability with all six strut loops closed.

The constrained optimization design successfully met objectives 1, 2 and 4 while objective 3 was achieved by appending filters that reduced the low frequency gain of the controller. The constrained optimization controller actually provided >30 dB

attenuation between 10 and 200 Hz and approximately 3 dB and 12 degrees of gain and phase margin respectively as computed from the FRF data. New objectives for a SISO constrained $\mathcal{H}_2$ controller are derived based on these results:

1. Reject sinusoidal disturbances with >30 dB attenuation in the 10–200 Hz range.
2. Provide 3 dB gain margin and 12° of phase margin.
3. Stability robustness to high frequency unmodeled dynamics through 20 dB per decade compensator roll off.

7.2 Design Model

Discrete time linear models with 0.0001 second time step were developed for each strut using a pseudo-linear identification (PLID) method [35] from FRF experimental data. Figure 7.2 shows the FRF data for Strut #1 compared to the 58th order linear model. The lightly damped modes below 200 Hz were intentionally left unmodeled because they are collocated and easily controlled. The modeling error in the frequency band of expected crossover is shown in Figure 7.3. Approximately 2 dB and 7° of gain and phase error between the measured FRF data and the state-space model is observed in the region of expected phase and gain crossovers respectively. These errors must be factored into the gain and phase margin constraints in the constrained $\mathcal{H}_2$ formulation. For example, to achieve 3 dB and 12° gain and phase margin with the FRF data, the controller must achieve at least 5 dB and 19° gain and phase margin with the linear model.

A 3rd order Pade approximate half cycle delay was appended to the control input to model processing delay present in the control computer. The control input was also passed through a zero order hold (ZOH) which accounts for another half cycle delay.

The constrained $\mathcal{H}_2$ method requires the design model to be in standard LQG form. Hence, the displacement output and control signal were selected as regulated outputs and a disturbance and noise was added to the control signal and displacement

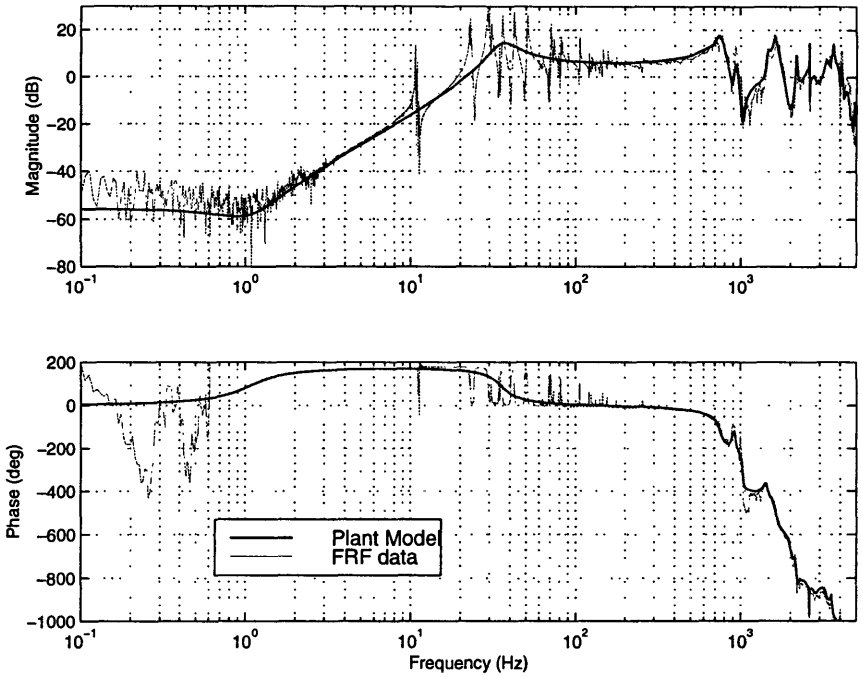

Figure 7.2: Strut #1 FRF data and plant model.

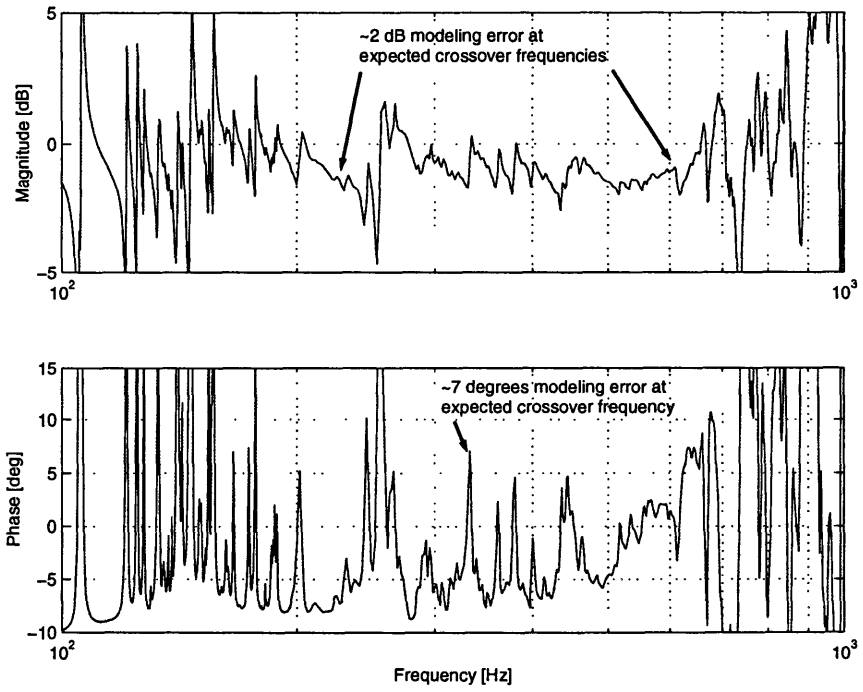

Figure 7.3: Strut #1 system identification error at expected crossover range.

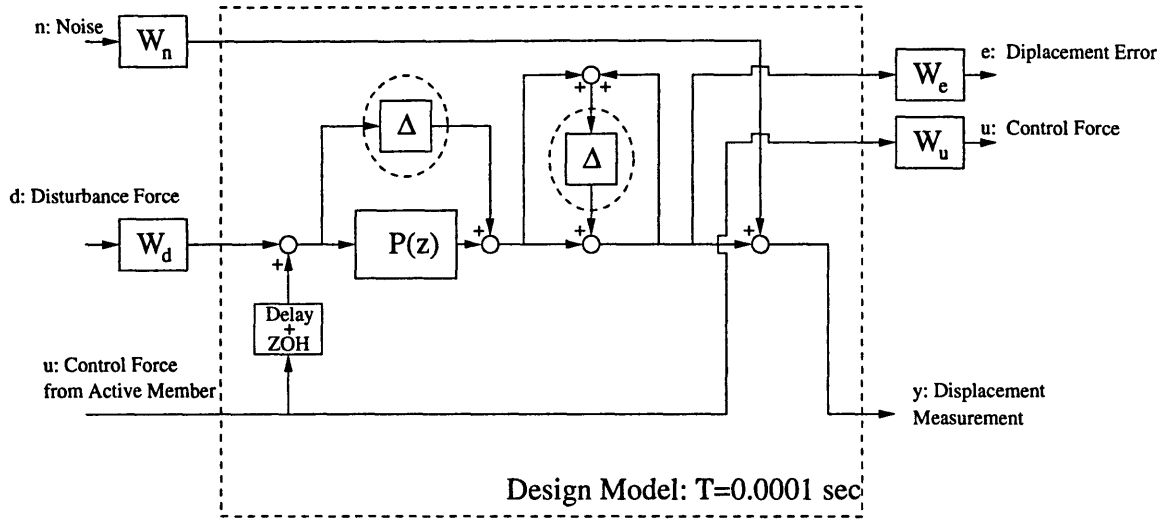

Figure 7.4: AVIS design model.

measurement respectively as shown in Figure 7.4. Frequency weights were appended to the model to penalize displacement error between 10–100 Hz and control effort at low and high frequencies. The weights are listed below and shown in Figure 7.5.

- Displacement Error: 3rd order, 100 Hz, Butterworth low-pass filter cascaded with 1st order, 1 Hz, Butterworth high-pass filter (W_e).
- Control: 2nd order filter with poles at 0.1 and 5000 Hz and zeros at 5 and 100 Hz (W_u).
- Disturbance Force: 3rd order, 100 Hz, Butterworth low-pass filter cascaded with 1st order, 1 Hz, Butterworth high-pass filter (W_d).
- Noise: -60 dB (W_n).

Modeling uncertainties were included as a mechanism to meet the roll-off and gain and phase margin objectives. An additive uncertainty $P + \Delta_a$ was included to add high frequency robust stability constraints, and a mixed multiplicative and divisive uncertainty at the plant output $(1 + \Delta_m)(1 - \Delta_m)^{-1}P$ was included to constrain the gain and phase margins. The outputs and inputs from these Δ blocks appear as extra inputs and outputs in the design model.

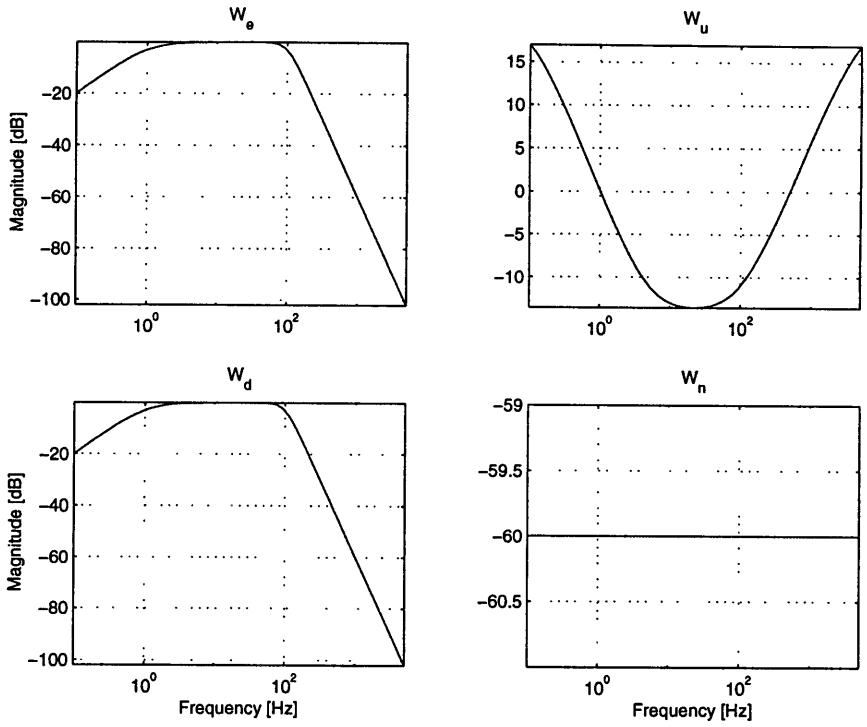

Figure 7.5: AVIS frequency weights.

7.3 Constrained $\mathcal{H}_2$ Design

The design objectives were simultaneously enforced by placing frequency constraints on the appropriate closed-loop transfer functions. Greater than 30 dB disturbance attenuation in the 10–200 Hz range was enforced by placing frequency-domain magnitude constraints at -26 dB on the closed-loop transfer function from disturbance to error, or $P/(1 - PK)$, in the 10–200 Hz band. The constraints and resulting closed loops based on the model and FRF data are shown in Figure 7.6 compared to the open-loop FRF data.

The gain and phase margin requirement was met by placing frequency-domain magnitude constraints on the transfer function seen by the mixed multiplicative and divisive uncertainty, or $(1 + PK)/(1 - PK)$, as discussed in Section 3.5. To achieve 3 dB and 12° of gain and phase margin with the FRF data, constraints were placed on $(1 + PK)/(1 - PK)$ corresponding to 5 dB and 20° to compensate for the modeling error at the crossover frequencies shown in Figure 7.3. The constraints were

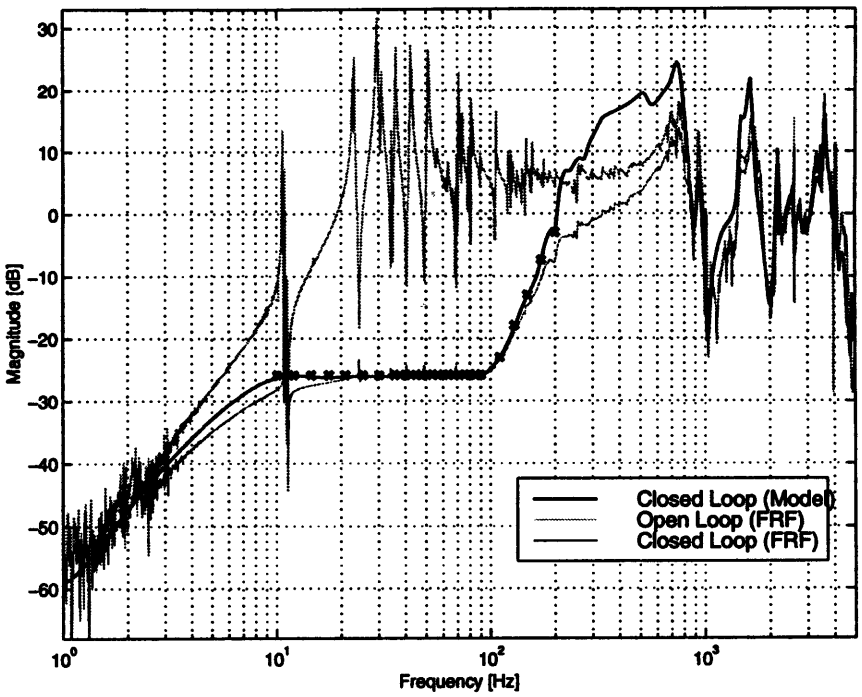

Figure 7.6: AVIS disturbance isolation constraints and closed-loop performance.

initially distributed about the expected crossover frequencies and after a couple design iterations they were moved to the actual crossover frequencies. The loop transfer function shown in Figure 7.8 shows that there were actually two phase crossover frequencies at approximately 210 and between 670-780 Hz while the gain crossover occurred between 310 and 380 Hz. To achieve 5 dB and 20° of gain and phase margin respectively, $(1+PK)/(1-PK)$ is constrained below 11.05 and 15.07 dB at phase and gain crossovers respectively. The gain and phase margin constraints and the resulting closed loop are shown in Figure 7.7.

The 20 dB/decade compensator roll-off constraint was enforced by constraining the transfer function seen by the additive uncertainty, or $K/(1-PK)$, as discussed in Section 3.3. At high frequency, assuming a small loop gain magnitude, the roll-off constraint is approximated by:

$$\left|\frac{K}{1-PK}\right|(\omega) \approx |K(\omega)| < \left(\frac{\omega}{\omega_{co}}\right)^{-\frac{|\alpha|}{20}}$$

where ω_{co} is the crossover frequency and α is the roll off slope in dB. The crossover frequency was picked to be 300 Hz with an α of 20. A total of 60 constraints between

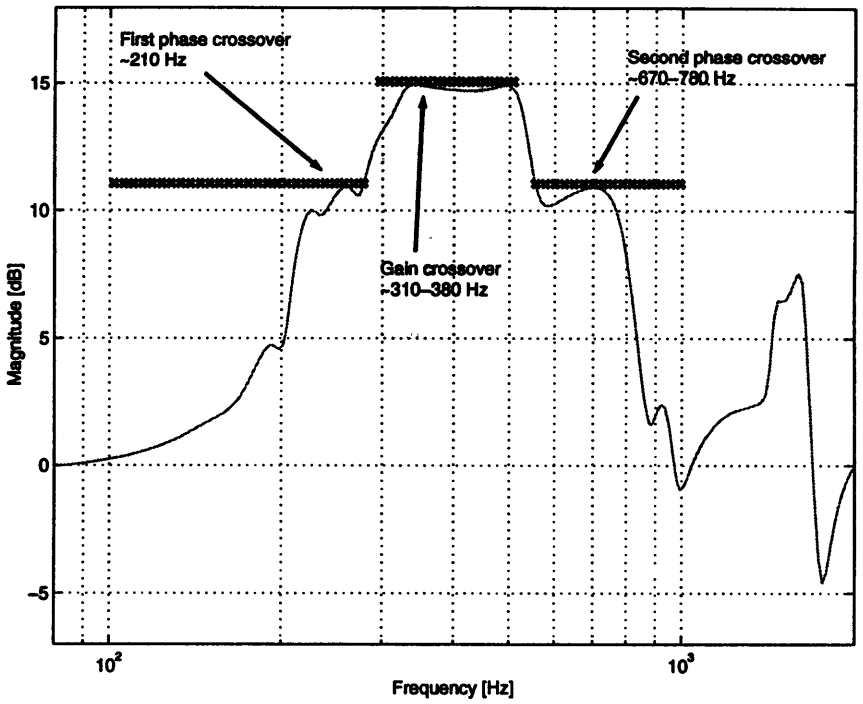

Figure 7.7: AVIS gain and phase margin constraints.

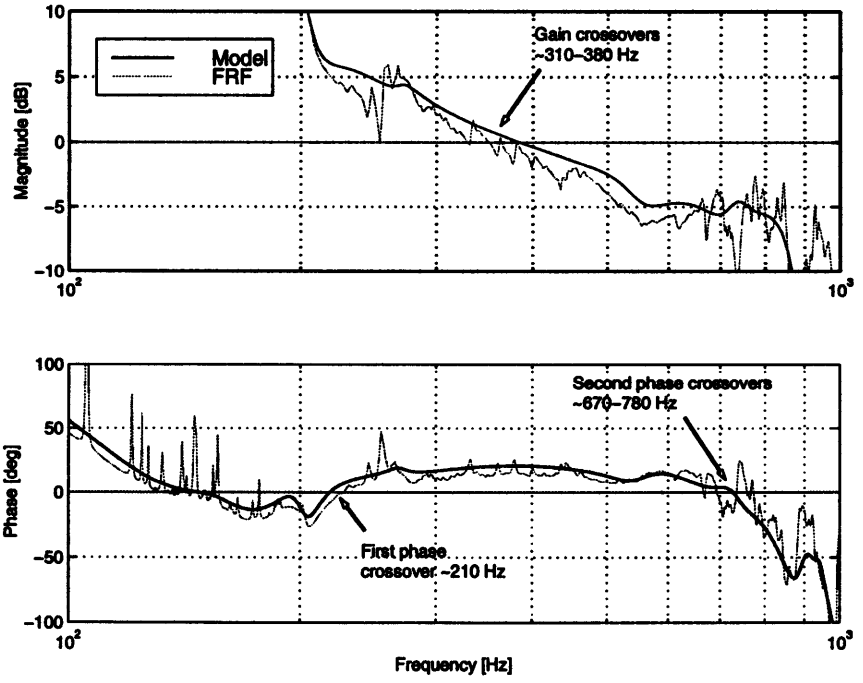

Figure 7.8: Gain and phase crossover frequencies with reduced constrained $\mathcal{H}_2$ design.

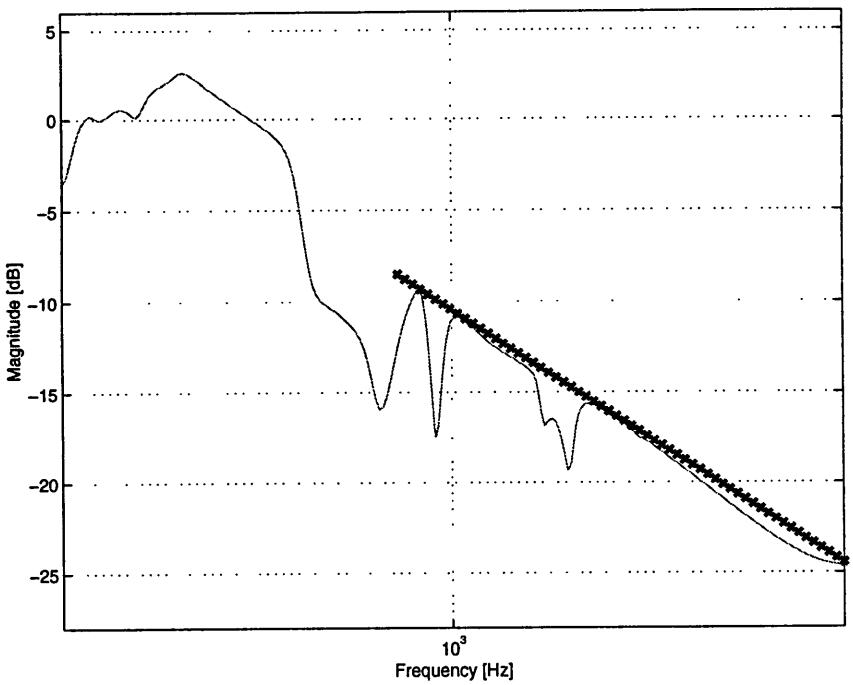

Figure 7.9: AVIS 20 dB/decade compensator roll-off constraints.

800-5000 Hz were placed on $K/(1-PK)$. The constraints and the resulting closed loop are shown in Figure 7.9.

7.4 Basis Selection

Three bases for Q were selected for this problem including the FIR and two GOBF bases. The algorithm described in Section 4.4 was used to minimize the order of the GOBF bases given an initial large order basis. For comparison, the algorithm was initialized with two different Legendre basis selections. First the algorithm was initiated with a 70th order Legendre basis with real poles at frequencies [25 75 ... 3475] Hz plus a constant. After several iterations, the basis was reduced to 21 GOBF plus a constant totaling 22 basis functions. At the algorithm termination, the majority of the GOBF poles are lightly damped as shown in Figure 7.10. The final quadratic program had 22 variables and 2337 linear constraints. A Sun Sparc 20 found the solution in five minutes using the MINOS optimization software [49]. The full order controller consisted of 92 stable states while a balanced model reduction [48] decreased

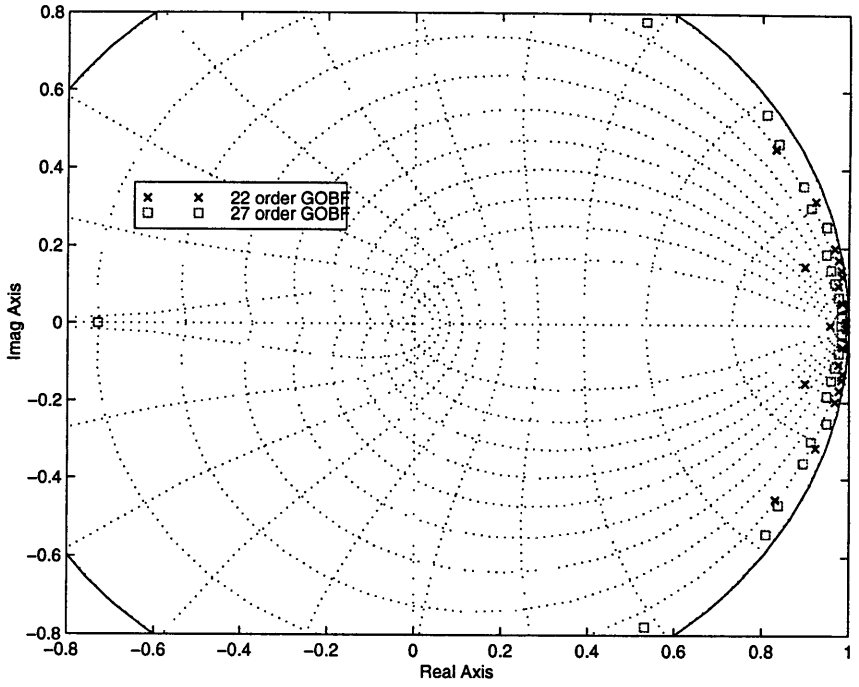

Figure 7.10: Pole locations for 22nd and 27th order GOBF.

the order to 27 states with no degradation in performance or stability margins. The figures and results presented in Section 7.3 are based on this solution.

The order of a constrained $\mathcal{H}_2$ controller designed using the algorithm described in Section 4.4 is sensitive to the initial basis selection and the model reduction choices of the designer. To demonstrate this, the problem was resolved starting with a 50 order Legendre basis with real poles at [25 75 ... 2475] Hz plus a constant. The iteration number, basis order, basis type, solution time, compensator order and closed-loop 2-norm are recorded in Table 7.1. After 4 iterations, a minimum of 26 GOBF plus a constant were needed to find a feasible solution. The 2-norm of the closed loop is relatively constant through the iterations indicating that the closed-loop designs are nearly identical at each step. The poles of the 27th order GOBF are compared to the 22nd order GOBF of the previous solution in Figure 7.10. Qualitatively the majority of the poles in both solutions are lightly damped although in general they do not match in z-plane location.

For comparison, the problem was resolved a third time with a 100th order FIR basis. MINOS found a feasible solution after 17:31 minutes, however closer inspection

Table 7.1: Iterative basis selection algorithm results.

Iteration #	Basis Order	Type	Solution Time	Compensator Order	$\|H\|_2$
1	51	Legendre	11:37	121	11.8080
2	42	GOBF	8:08	112	11.8066
3	34	GOBF	6:30	104	11.7965
4	27	GOBF	5:46	97	11.7403

of the closed loop reveals that the solution is actually invalid. High frequency spiking occurs between the constraints in the closed-loop transfer function $K/(1-PK)$ shown in Figure 7.11 making the solution unacceptable. This is a common problem when a poor basis is selected for Q. One remedy to prevent spiking is to increase the constraint density over the frequency band where the spiking occurs. Experience shows that when the constraint density is increased with no adjustment in basis order, the problem becomes infeasible, hence requiring even more basis functions. This initiates an iterative process of resolving the problem with an increasing number of basis functions and constraints until either a feasible solution is found or the problem is determined infeasible. This can be time consuming and leads to excessively large compensators. An alternative conjecture is that spiking may be a symptom of an improperly weighted $\mathcal{H}_2$ norm minimization. In this case the solution is to increase the corresponding frequency weight in the band where the spiking occurs. The hope is that the weighted $\mathcal{H}_2$ optimization leg of the quadratic program will remove the spikes after a feasible solution is found.

7.5 Compensator and Results

The full and reduced order constrained $\mathcal{H}_2$ compensators resulting from the 22nd order GOBF solution are shown in Figure 7.12 compared to the classical design. The constrained $\mathcal{H}_2$ controller shows higher gain in and below the 10-200 Hz disturbance isolation frequency band while exhibiting increasing phase lead above 200 Hz. The

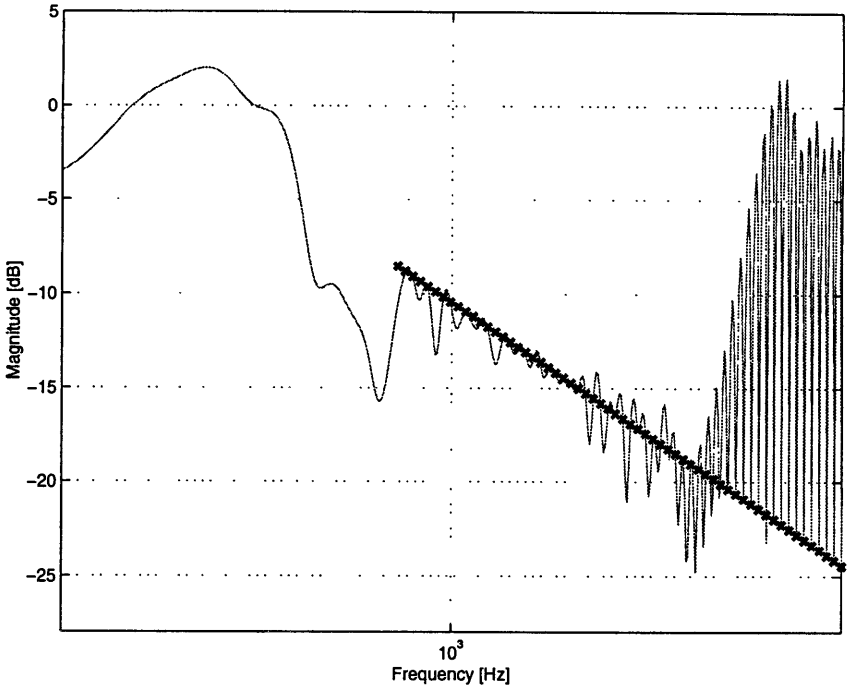

Figure 7.11: High frequency spiking in $K/(1-PK)$ with 100 order FIR basis.

additional gain of the constrained $\mathcal{H}_2$ controller provides better disturbance isolation performance than the classical design in the 10-200 Hz band as shown in Figure 7.13. At the gain crossover (310-380 Hz), the constrained $\mathcal{H}_2$ controller shows slightly more phase lead than the classical controller. The exact gain and phase margins are shown on the Nichols chart in Figure 7.14 for the reduced order constrained $\mathcal{H}_2$ compensator with the model and FRF data. The model based gain and phase margins are 5 dB and 20° respectively as expected from the gain and phase margin constraints. However, the actual FRF based gain and phase margins are 3 dB and 12° which corresponds perfectly to the original objective. Finally, above 800 Hz the constrained $\mathcal{H}_2$ compensator gain rolls-off at 20 dB/decade.

The classical, constrained optimization, and full and reduced constrained $\mathcal{H}_2$ controllers are compared in Table 7.2 in terms of their order and closed-loop 2-norm. The order of the constrained $\mathcal{H}_2$ controller is derived by summing the order of the design model, frequency weights and Q (the number of basis functions). The 2-norm is a good qualitative measure of the degree of disturbance isolation and roll-off that the

Table 7.2: AVIS controller comparison.

Controller	Controller Order	$\|H\|_2$
Classical [29]	3	16.9158
Constrained Optimization [45]	161	-
Constrained $\mathcal{H}_2$	92	11.3110
Reduced Constrained $\mathcal{H}_2$	27	11.6688

compensator provides. Little degradation is observed in the 2-norm performance between the reduced constrained $\mathcal{H}_2$ controller and full order design. A more dramatic 31% improvement in the 2-norm is observed between the classical and the reduced constrained $\mathcal{H}_2$ design at the price of 24 states. The table also illustrates that the constrained $\mathcal{H}_2$ method resulted in a much lower order controller than the constrained optimization method before reduction for this example.

7.6 Conclusion

Active vibration isolation or disturbance rejection is well suited for the constrained $\mathcal{H}_2$ design method. Typical disturbance attenuation, gain and phase margin, and compensator roll-off constraints are directly incorporated into the design process with the appropriate compensation for modeling error. The GOBF were a particularly important factor in finding a low order, well behaved feasible solution in this example. Up to 100 FIR basis functions were shown to produce unacceptable solutions compared to the 22th order GOBF solution which simultaneously met all of the objectives. The resulting constrained $\mathcal{H}_2$ controller was of order 92, but simple model reduction reduced this controller to 27 states with no degradation in the performance and stability margins.

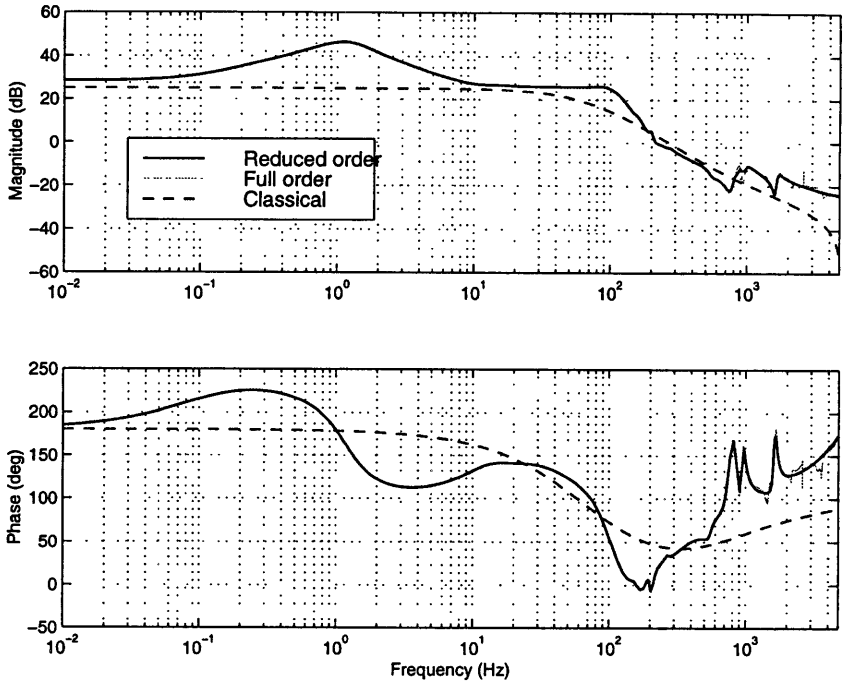

Figure 7.12: Comparison of full and reduced order constrained $\mathcal{H}_2$ controllers with classical.

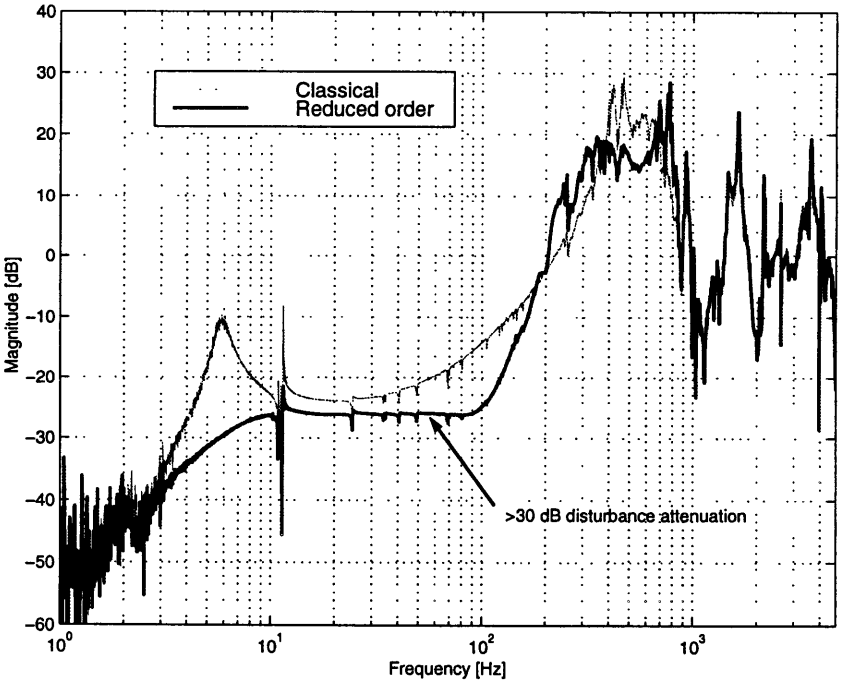

Figure 7.13: Disturbance isolation comparison of classical and reduced order constrained $\mathcal{H}_2$ design.

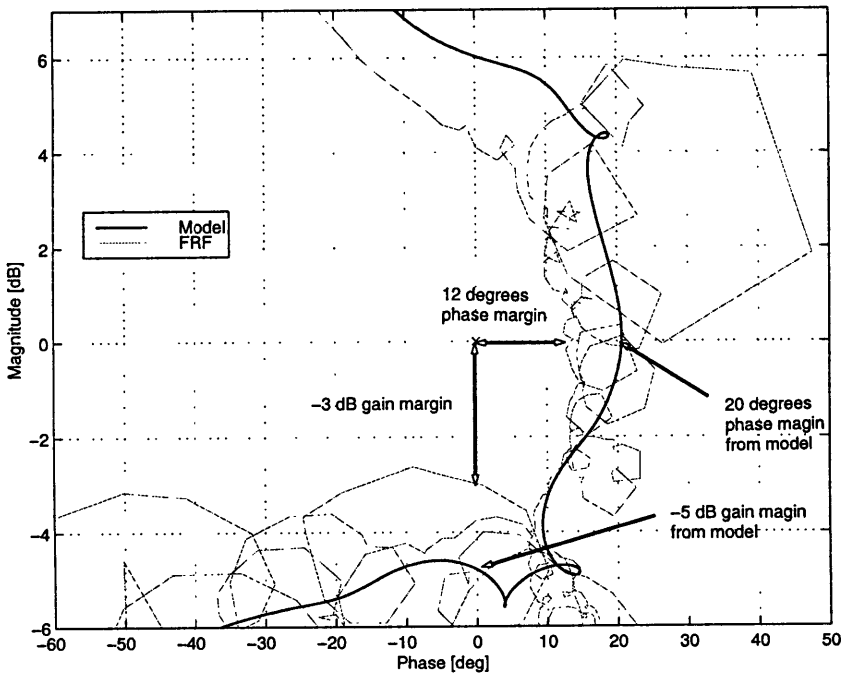

Figure 7.14: Gain and phase margins corresponding to 5 dB and 20° constraints with reduced constrained $\mathcal{H}_2$ design; actual FRF based margins are 3 dB and 12°.

Chapter 8

Conclusions

A linear controller design tool was developed which poses the most typical specifications and weighted $\mathcal{H}_2$ objective as a convex mathematical program. The tool exploits two simple types of constraints in the frequency and time domain to formulate a variety of closed-loop specifications including robustness to modeling uncertainty and gain and phase margins. The practical utility of this tool was demonstrated on real applications by designing constrained $\mathcal{H}_2$ controllers for a precision pointing attitude control system and an active vibration isolation system. The constrained $\mathcal{H}_2$ design of the precision pointing attitude control system proved to be the first controller to simultaneously meet the provided set of performance and stability robustness specifications. In the active vibration isolation system design example, the constrained $\mathcal{H}_2$ method was successful in meeting the design specifications while subsequent analysis based on experimental frequency data verified the results.

This tool uses a direct parameter optimization approach of the closed-loop Youla or Q-parameter. The Youla parameterization is an affine, free parameter representation in the variable Q of the set of closed loops achievable by all stabilizing compensators. Although Q can be represented by any stable system, which spans an infinite dimensional space, this space is approximated with a finite number of basis functions for optimization. The basis selection for Q introduces an important tradeoff between finding feasible solutions to the mathematical program and the compensator dimension. A large basis for Q increases the probability of finding a feasible solution

(if one exists) while driving the compensator order up.

One criticism of this method is that it results in high order compensators due to the large number of basis functions needed to find a feasible solution. This problem was addressed by considering the newly rediscovered Generalized Orthogonal Basis Functions for Q rather than the standard FIR, Laguerre or Kautz bases. These functions introduce extra flexibility in pole location and ordering that can be exploited to find lower order compensators. An iterative algorithm was proposed as an *ad hoc* way of finding a low order basis for Q. This algorithm starts with an high order basis for Q with arbitrary pole locations, then uses model reduction on the solution to find the basis poles for the next step. The algorithm proved to be effective in reducing the basis order in the two examples presented. It was also demonstrated that further model reduction of the resulting compensator often leads to lower order controllers with little or no impact on stability and performance. This framework provides an effective "engineer in the loop" method of synthesizing mixed objective linear compensators.

Constraints on closed-loop frequency and time responses were central in this work. Linear approximations of the frequency domain constraints were used in the examples. These approximations were found to perform better when using the MINOS optimization software than the exact quadratic forms. For example, in some cases the optimization algorithm could not find a feasible solution when the constraints were posed in quadratic form, while a solution was found quickly when the constraints were in linear form. The frequency domain constraints were shown to be useful in constructing robustness to modeling uncertainty and gain and phase margin constraints. The small gain theorem acted as the link between the close-loop gain and these specifications. As expected, this naturally produces gain stabilized solutions to robust control problems. Phase stabilization solutions of uncertain dynamics were not explored in this work.

The constrained $\mathcal{H}_2$ approach has proven to be a useful linear controller design technique for many real problems. With the constrained $\mathcal{H}_2$ tool developed in this work, an engineer can be given a plant and a set of design specifications and find a

controller suitable for implementation or determine with some confidence that one does not exist.

8.1 Future Work

The problem of finding the best basis for Q is still a problem at large. Much work is needed to understand the infinite-dimensional constraint set on Q before a basis is introduced. This understanding would help the engineer pick a minimum order basis for Q that produces a feasible solution to the mathematical program. One idea is to parameterize Q in terms of the real and imaginary parts of the complex frequency response to solve for the frequency response of Q. Using system identification techniques, a low order model of the solution may be obtained. Of course for this approach to work, the frequency and impulse responses must be realizable by a linear stable system which may be a limiting restriction of this method. Another idea is to construct a basis for Q one pole at a time by searching over the pole locations and picking the pole that comes closest to meeting the constraints. However at each iteration, the mathematical program must be rewritten and resolved from scratch which could be a computational burden.

There are plenty of possibilities to expand the menu of constraints to encompass more control problems. One area left unexplored was the use of LMI constraints and semidefinite programming. LMI constraints could open the door to maximum singular value or $\mathcal{H}_\infty$ constraints and frequency-domain constraints over a band rather than a single point. With the continuing innovation in computer technology and optimization algorithms, LMI constraints are quickly entering the control community mainstream and promise to rival linear and quadratic programming problems in efficiency.

The method presented in this work falls into the model-based control category, where the plant model is used to construct the Youla-parameterization and the constraints. An attractive extension of this work would be to eliminate the need of a plant model. A method that could construct the Youla-parameterization and constraints from experimental frequency or time data would no doubt be a more powerful tool.

Eventually a model of the stabilizing compensator will be needed for implementation implying that data-based design methodologies will likely be hybrid where both data and models will find their place.

Bibliography

[1] B. Appleby and R. Hughes, "A High Performance Robust Attitude Controller for Flexible Spacecraft," *AIAA Guidance, Navigation, and Control Conference,* Scottsdale, Arizona, pp. 181–187, August 1994.

[2] D. Bossert, U.-L. Ly, J. Vagners, "Evaluation of Reduced-Order Controllers on a Two-Link Flexible Manipulator," *Proceedings of the American Control Conference,* Seattle, Washington, June 1995.

[3] S.P. Boyd and C.H. Barratt, *Linear Controller Design: Limits of Performance.* Englewood Cliffs, NJ: Prentice–Hall, 1991.

[4] S.P. Boyd, V. Balakrishnan, C.H. Barratt, N.M. Khraishi, X. Li, D.G. Meyer, and S. A. Norman, "A new CAD method and associated architectures for linear controllers," *IEEE Transactions on Automatic Control,* vol. 33, pp. 268–283, March 1988.

[5] S.P. Boyd, L. El Ghaoui, E. Feron, V. Balakrishnan, *Linear Matrix Inequalities in System and Control Theory.* SIAM, 1994.

[6] A.J. Calise and K.A. Fegley, "Quadratic programming in the statistical design of sampled-data control systems," *IEEE Transactions on Automatic Control,* pp. 77-80, February 1968.

[7] R.A. de Callafon, P.M.J. Van den Hof, M. Steinbuch, "Control relevant identification of compact disc pick-up mechanism," *Proceedings of the 32nd Conference on Decision and Control,* San Antonio, Texas, December 1993.

[8] R.V. Churchill and J.W. Brown, *Complex Variables and Applications, Fifth Addition.* McGraw–Hill, Inc. 1990.

[9] M.A. Dahleh and I. Diaz-Bobillo, *Control of Uncertain Systems: A Linear Programming Approach.* Englewood Cliffs, NJ: Prentice–Hall, 1994.

[10] M.A. Dahleh and J.B. Pearson, Jr., "l^1-Optimal Feedback Controllers for MIMO Discrete-Time Systems," *IEEE Transactions on Automatic Control,* vol. 32, no. 4, pp. 314–322, April 1987.

[11] R.L. Daily, "Lecture Notes for the Workshop on $\mathcal{H}_\infty$ and μ Methods for Robust Control," presented at the *IEEE Conference on Decision and Control,* December 1991.

[12] E.J. Davision and I.J. Ferguson, "The Design of Controllers for the Multivariable Robust Servomechanism Problem Using Parameter Optimization Methods," *IEEE Transactions on Automatic Control,* vol.26, no. 1, February 1981.

[13] C.A. Desoer, R-W. Liu, J. Murray, R. Saeks, "Feedback System Design: The Fractional Representation Approach to Analysis and Synthesis," *IEEE Transactions on Automatic Control,* vol. 25, no. 3, pp. 399–412, June 1980.

[14] I. Diaz-Bobillo, *The General l^1 Multiblock Problem: Exact and Approximate Solutions.* Ph.D. Thesis, Massachusetts Institute of Technology, February 1992.

[15] J.C. Doyle, "Lecture Notes in Advances in Multivariable Control," ONR/Honeywell Workshop, Minneapolis, MN.

[16] N. Elia, *Computational Methods for Multi-Objective Control.* Ph.D. Thesis, Massachusetts Institute of Technology, September 1996.

[17] M. Escobar, *Systematic Procedure to Meet Specific Input/Output Constraints in the ℓ_1-optimal Control Problem Design.* Masters Thesis, MIT, February 1995.

[18] K.A. Fegley, "Designing sampled-data control systems by linear programming," *IEEE Transactions on Applications and Industry,* vol. 81, pp. 198–200, May 1964.

[19] K.A. Fegley, S. Blum, J.O. Bergholm, A.J. Calise, J.E. Marowitz, G. Porcelli, and L.P. Sinha, "Stochastic and deterministic design and control via linear and quadratic programming," *IEEE Transactions on Automatic Control,* vol. AC-16, pp. 759–765, December 1971.

[20] K.A. Fegley and M.I. Hsu, "Optimum discrete control by linear programming," *IEEE Transactions on Automatic Control,* vol. 9, pp. 114–115, January 1965.

[21] B.A. Francis, *A Course in $\mathcal{H}_\infty$ Control Theory.* Lecture Notes in Control and Information Sciences, vol. 88, Springer-Verlag, 1988.

[22] R.M. Freund and S. Mizuno, "Interior Point Methods: Current and Future Directions," MIT O.R. Working Paper 318-96, *Optima,* 51, 1996.

[23] Y. Fu, G.A. Dumont, "An Optimum Time Scale for Discrete Laguerre Network," *IEEE Transactions on Automatic Control,* vol. 38, No 6, pp. 934-938, June 1993.

[24] Gill, P.E., Murray, W. and Wright, M.H., *Practical Optimization.* Academic Press, London, 1981.

[25] C.L. Gustafson and C.A. Desoer, "Controller design for linear multivariable feedback systems with stable plants, using optimization with inequality constraints," *International Journal of Control,* vol. 37, no. 5, pp. 881-907, 1983.

[26] C.L. Gustafson and C.A. Desoer, "A CAD methodology for linear mulitvariable feedback systems based on algebraic theory," *International Journal of Control,* vol. 41, no. 3, pp. 653-675, 1985.

[27] G. Hadley, *Linear Programming.* Addison-Wesley Publishing Company, Inc., 1962.

[28] S.R. Hall, *A Failure Detection Algorithm for Linear Dynamic Systems.* Sc. D. Thesis, MIT, June 1985.

[29] T.C. Henderson, "Design and testing of a broadband active vibration isolation system using stiff actuators," *19th AAS Guidance and Control Conference,* February 1996.

[30] Z. Hu and P.D. Loewen, "Numerical solution of multiple objective control system design problem for SISO systems," *Proceedings of the American Control Conference,* Seattle, Washington, June 1995.

[31] P.S.C. Heuberger, P.M.J. Van Den Hof, O.H. Bosgra, "A generalized orthonormal basis of linear dynamic systems," *Proceedings of the 32nd Conference on Decision and Control,* San Antonio, Texas, December 1993.

[32] T.C. Henderson, M.D. Piedmonte, L.K. McGovern, J.W. Jang, and B.V. Lintereur, *Structural Control Toolbox.* User's Guide, November 1997.

[33] P.S.C. Heuberger and O.H. Bosgra, "Approximate system identification using system based orthonormal functions," *Proceedings of the 29th Conference on Decision and Control,* Honolulu, Hawaii, December 1990.

[34] P. Heuberger, P. Van den Hof, and O. Bosgra, "A Generalized Orthonormal Basis for Linear Dynamical Systems," *IEEE Transactions on Automatic Control,* vol. 40, no. 3, pp. 451–465. March, 1995.

[35] M.A. Hopkins and H.F. VanLandingham, "Optimal nonlinear estimation of linear stochastic systems," *Journal of Dynamics Systems, Measurement, and Control,* vol. 115, pp. 529-536, Sept. 1994.

[36] D.R. Jaques and D.B. Ridgely, "A Fixed-Order, Mixed-Norm Control Synthesis Method for Discrete Linear Systems," *Proceedings of the American Control Conference,* Seattle, Washington. June 1995.

[37] D.R. Jaques and D.B. Ridgely, "Convexity vs. Compensator Order for the Discrete-Time, Mixed-Norm Control Problem," *Proceedings of the 34th Conference on Decision and Control,* New Orleans, LA. December 1995.

[38] Y. W. Lee, *Statistical Theory of Communication.* John Wiley & Sons, Inc. 1960.

[39] D. Linder, J. Bolek, and J. Lombardo, "Guidance, Navigation, and Control Subsystem for the EOS-AM spacecraft," *Proc. of the AIAA Guidance, Navigation, and Control Conference,* Hilton Head, S.C., August 1992.

[40] B.V. Lintereur and L.K. McGovern, "Constrained $\mathcal{H}_2$ Design via Convex Optimization Applied to Precision Pointing Attitude Control," *Proceedings of the IEEE Conference on Decision and Control,* December 1997, San Diego.

[41] U.-L. Ly. "Robust Control Design Using Nonlinear Constrained Optimization," *Proceedings of the 1990 American Control Conference,* vol. 1, pp. 968–9, San Diego, California, 1990.

[42] U.-L. Ly, A.E. Bryson, and R.H. Cannon, "Design of Low-Order Compensators using Parameter Optimization," *Automatica,* vol. 21, no. 3, pp. 315-318, 1985.

[43] J.M. Maciejowski, *Multivariable Feedback Design.* New York: Addison Wesley, 1989.

[44] J.E. Marowitz and K.A. Fegley, "System design using quadratic programming," *IEEE Transactions on Automatic Control,* vol. 16, no. 3, pp. 241–246.

[45] L.K. McGovern, *A Constrained Optimization Approach to Control with Application to Flexible Structures.* Masters Thesis, MIT, June 1996.

[46] L.K. McGovern, T.C. Henderson, "Design of an Active Vibration Isolation Control System Using Constrained Optimization," *Proceedings of the American Control Conference,* Albuquerque, N.M., pp. 3115–3120, 1997.

[47] R.A. Mills and A.E. Bryson, "Parameter-Robust Control Design Using a Minimax Method," *Journal of Guidance, Control, and Dynamics,* vol. 15, no. 5, September-October 1992.

[48] B.C. Moore, "Principal component analysis in linear system: controllability, observability, and model reduction," *IEEE Transactions on Automatic Control,* AC-26, pp. 17–31, 1981.

[49] B.A. Murtagh, M.A. Saunders, *MINOS 5.4 User's Guide.* Systems Optimization Laboratory, Stanford University, February 1995.

[50] V. Nalbantoglu, J. Bokor and G. Balas, "System identification with generalized orthonormal basis functions: an application to flexible structures," *2nd IFAC Symposium on Robust Control Design,* June 1997, Budapest, Hungary. *Submitted to Automatica,* February 1998.

[51] Y. Nesterov and A. Nemirovskii, *Interior-Point Polynomial Algorithms in Convex Programming.* Philadelphia: SIAM, 1994.

[52] C.N. Nett, C.A. Jacobson, M.J. Balas, "A connection between state-space and doubly coprime fractional representations," *IEEE Transactions on Automatic Control,* vol. 29, no. 9, pp. 831–832, September 1984.

[53] B. Ninness and J.C. Gomez, "Asymptotic analysis of MIMO system estimates by the use of orthonormal bases," Technical Report, Department of Electrical and Computer Engineering, University of Newcastle, Australia.

[54] B. Ninness and F. Gustafsson. "A Unifying Construction of Orthonormal Bases for System Identification," *IEEE Transactions on Automatic Control,* vol. 42, no. 4, pp. 515–521, April 1997.

[55] B. Ninness, H. Hjalmarsson, F. Gustafsson, "Bias and variance analysis of estimation using fixed denominator model structures," Technical Report EE9617, Department of Electrical and Computer Engineering, University of Newcastle, Australia.

[56] C.M. Oakley and C.H. Barratt. "End point controller design for an experimental two-link flexible manipulator using convex optimization," *Proceedings of the American Control Conference,* 1990.

[57] L. Pernebo, "An algebraic theory for the design of controllers for linear multivariable systems- Part I: structure matrices and feedforward design," *IEEE Transactions on Automatic Control,* vol. 26, no. 1, pp. 171–182, February 1981.

[58] L. Pernebo, "An algebraic theory for the design of controllers for linear multivariable systems- Part II: Feedback realizations and feedback design," *IEEE Transactions on Automatic Control,* vol. 26, no. 1, pp. 183–194, February 1981.

[59] E. Polak, "Optimization-based Computer-aided design of control systems: a survey," *Proceedings of the IECON'87: 1987 International Conference on Industrial Electronics, Control, and Instrumentation,* vol. 2, pp 796–7, 1987.

[60] E. Polak, S. E. Salcudean. "On the Design of Linear Multivariable Feedback Systems Via Constrained Nondifferentiable Optimization in H^∞ Spaces," *IEEE Transactions on Automatic Control,* vol. 34, no. 3, pp. 268–276, March 1989.

[61] E. Polak, P. Siegel, T. Wuu and W.T. Nye, "DELIGHT.MIMO: An interactive, optimization-based mulitvariable control system design package," *Computer-Aided Control Systems Engineering,* Elsevier Science Publishers B.V., North-Holland, 1985; reprinted from *IEEE Control Systems Magazine,* vol. 2, no. 4, pp. 9–14, December 1982.

[62] E. Polak, D. M. Stimler. "Optimization-Based Design of Control Systems with Uncertain Plant," *Applications of Nonlinear Programming to Optimization and Control. Proceedings of the 4th IFAC Workshop,* pp. 25-33, San Francisco, California, 1983.

[63] R.A. Roberts, C.T. Mullis. *Digital Signal Processing.* Addison-Wesley Publishing Company, Reading, Massachusetts, 1987.

[64] G. Strang, *Linear Algebra and its Applications.* Harcourt Brace Jovanovich, FL, 1988.

[65] P.M.M. Van Den Hof, P.S.C. Heuberger, J. Bokor, "System identification with generalized orthonormal basis functions," *Automatica,* vol. 31, no. 12, pp. 1821–1834, 1995.

[66] M. Vidyasagar, *Control System Synthesis: A Factorization Approach.* MIT Press, Cambridge, Massachusetts, 1985.

[67] M.A. deVirgilio and D.K. Kamimoto. "Practical Applications of Modern Controls for Booster Autopilot Design," *AIAA/IEEE Digital Avionics Systems Conference,* Fort Worth, Texas, 1993.

[68] D.K. de Vries and P. Van den Hof, "Frequency domain identification with generalized orthonormal basis functions," *IEEE Transactions on Automatic Control,* vol. 43, no. 5, pp. 656–669, May 1998.

[69] C. Voth and U.-L. Ly. "Total Energy control system autopilot design with constrained parameter optimization," *Proceedings of the 1990 American Control Conference,* vol. 2, pp. 1332-7, San Diego, California, 1990.

[70] G.N. Ward and U.-L. Ly. "Stability Augmentation Design of a Large Flexible Transport Using Nonlinear Parameter Optimization," *Journal of Guidance, Control, and Dynamics,* vol. 19, no. 2, March-April 1996.

[71] D.C. Youla, J.J. Bongiorno, and H.A. Jabr, "Modern Wiener-Hopf design of optimal controllers—Part I: The single-input-output case," *IEEE Transactions on Automatic Control,* vol. AC-21, no. 1, pp. 3–13, June 1976.

[72] D.C. Youla, H.A. Jabr, and J.J. Bongiorno, "Modern Wiener-Hopf design of optimal controllers—Part II: The multivariable case," *IEEE Transactions on Automatic Control,* vol. AC-21, no. 3, pp. 319–338, June 1976.

[73] K. Zhou, J.C. Doyle, and K. Glover, *Robust and Optimal Control.* Prentice Hall, Upper Saddle River, New Jersey, 1996.